Quantitative Measurements of Cerebral Hemodynamics using Magnetic Resonance Imaging

Dr. Amit Mehndiratta

Supervised by Dr. Michael A. Chappell and Dr. Stephen J. Payne

Keble College

Trinity Term 2013

Department of Engineering Science
University of Oxford

This thesis is submitted to the University of Oxford, in partial fulfillment of the requirements for the degree of Doctor of Philosophy. This thesis is entirely my own work and, except where otherwise indicated, describes my own research.

Quantitative Measurements of Cerebral Hemodynamics using Magnetic Resonance Imaging

Dr. Amit Mehndiratta

Keble College

Trinity Term 2013

Submitted in partial fulfillment of the requirements for the degree of Doctor of Philosophy

Abstract

Cerebral ischemia is a vascular disorder that is characterized by the reduction of blood supply to the brain, resulting in impaired metabolism and finally death of brain cells. Cerebral ischemia is a major clinical problem associated with global morbidity and mortality rates of about 30%. Clinical management of cerebral ischemia relies heavily on perfusion analysis using dynamic susceptibility contrast MRI (DSC-MRI). DSC-MRI analysis is performed using mathematical models that simulate the underlying vascular physiology of brain. Cerebral perfusion is calculated using perfusion imaging and is used as a marker of tissue health status; low perfusion being an indicator of impaired tissue metabolism.

In addition to measurement of cerebral perfusion, it is possible to quantify the blood flow variation within the capillary network referred to as cerebral microvascular hemodynamics. It has been hypothesized that microvascular hemodynamics are closely associated with tissue oxygenation and that hemodynamics might undergo a considerable amount of variation to maintain normal tissue metabolism under conditions of ischemic stress. However with DSC-MRI perfusion imaging, quantification of cerebral hemodynamics still remains a big challenge.

Singular Value Decomposition (SVD) is currently a standard methodology for estimation of cerebral perfusion with DSC-MRI in both research and clinical settings. It is a robust technique for quantification of cerebral perfusion, however, the quantification of hemodynamic information

cannot be achieved with SVD methods because of the non-physiological behaviour of SVD in microvascular hemodynamic estimation. SVD is sensitive to the noise in the MR signal which appears in the calculated microvascular hemodynamics, thus making it difficult to interpret for pathophysiological significance. Other methods, including model-based approaches or methods based on likelihood estimation, stochastic modeling and Gaussian processes, have been proposed. However, none of these have become established as a means to study tissue hemodynamics in perfusion imaging. Possibly because of the associated constrains in these methodologies that limited their sensitivity to hemodynamic variation *in vivo*.

The objective of the research presented in this thesis is to develop and to evaluate a method to perform a quantitative estimation of cerebral hemodynamics using DSC-MRI. A new Control Point Interpolation (CPI) method has been developed to perform a non-parametric analysis for DSC-MRI. The CPI method was found to be more accurate in estimation of cerebral perfusion than the alternative methods. Capillary hemodynamics were calculated by estimating the transit time distribution of the tissue capillary network using the CPI method. The variations in transit time distribution showed quantitative differences between normal tissue and tissue under ischemic stress. The method has been corrected for the effects of macrovascular bolus dispersion and tested over a larger clinical cohort of patients with atherosclerosis. CPI method is thus a promising method for quantifying cerebral hemodynamics using perfusion imaging. CPI method is an attempt to evaluate the use of quantitative hemodynamic information in diagnostic and prognostic monitoring of patients with ischemia and vascular diseases.

Dedicated to my father

Shri. V.N. Mehndiratta

1948-1992

Acknowledgments

I would like to express profound gratitude to my supervisors Dr. Michael A. Chappell and Dr. Stephen J. Payne for guiding me carefully through this research. I have been benefited from their efficient supervision, great kindness and patience and I wish to say a heartfelt thanks to them. One simply could not wish for better and friendlier mentors.

I am as ever indebted to my parents, including my uncle (mamaji), and sisters for their love, affection and support throughout my life. I attribute the level of my achievements to their efforts in keeping me motivated to progress further in life. I also wish to thank my brother-in-laws for their encouragement and guiding me in the right directions to progress both personally and professionally. And I also thank my wife for her love and support.

I would like to extend my sincere thanks to the Felix Scholarship that supported me financially for my DPhil. studies at University of Oxford. Without the support from the Felix Scholarship I would not have been able to dream of coming to Oxford for this research project. I am also thankful to colleagues and the staff at the Keble College for being so supportive in the whole process of my DPhil.

I would like to thank Brad and Dave for supporting me with the clinical data required for this research. The very useful and constructive discussions with them helped me improve on the work.

And finally thanks to my friends for their continuous support. I would like to thank Siddharth, Prabu, Tee, Chang, Marco and Ilaria for providing me much required discussions, both academic and non-academic. I am also thankful to all people at PUMMA and QuBIc groups for their support.

Table of Contents

List of Figures

List of Tables

Nomenclature

List of Abbreviations

AIF	Arterial Input Function
CBF	Cerebral Blood Flow
CBFratio	Ratio of estimated CBF and true CBF
CBV	Cerebral Blood Volume
CP	Control Point
CPI	Control Point Interpolation
CTC	Concentration Time Curve
CTTH	Capillary Transit Time Heterogeneity
DSC-MRI	Dynamic Susceptibility Contrast Magnetic Resonance Imaging
EDK	Exponential Dispersion Kernel
GDK	Gamma Dispersion Kernel
GPD	Gaussian Process Deconvolution
GRE	Gradient Echo
LNDK	Log-Normal Dispersion Kernel
MTT	Mean Transit Time
NSR	Nonlinear Stochastic Regularization
OI	Oscillatory Index
oSVD	block-circulant Singular Value Decomposition
pdf	Probability distribution function
PWI	Perfusion Weighted Imaging
SNR	Signal to Noise Ratio
SVD	Singular Value Decomposition
SSE	Sum of squared errors
sSVD	standard SVD
tSVD	truncated SVD
tkSVD	Tikhonov SVD

TE	Echo Time
TR	Repetition Time
TRF	Tissue Response Function
TTP	Time-to-peak
VM	Vascular Model
VTF	Vascular Transport Function

English Letter Symbols

B_0	External magnetic Field
C	Tissue Concentration
Ca	Arterial Concentration
h	Transit time distribution
k	Proportionality constant between concentration and transverse relaxation rate
k_H	Difference in hematocrit between capillary and large vessel
M_{xy}	Transverse magnetization
M_z	Longitudinal magnetization
M_0	Maximum tissue magnetization
p	Time-to-peak of Gamma Dispersion Kernel
$Psvd$	Threshold for truncated SVD
R	Residue function
R_{disp}	Dispersed residue function
$R10$	Time taken by the residue function to drop to 10% of its maximum
s	Sharpness of Gamma Dispersion Kernel
S	Signal
Skw	Skewness of the curve
t	Time
$T1$	Longitudinal Relaxation Time
$T2$	Transverse Relaxation Time

Greek Letter Symbols

α	Shape parameter of Gamma Probability Distribution
β	Scale parameter of Gamma Probability Distribution
β_{lrz}	Time constant for Lorentzian residue function
γ	Gyro-magnetic ratio
δ	Delay in bolus arrival
ζ	Time spacing between control points
η	Number of control point in CPI
θ	Time constant for exponential dispersion kernel
λ	Shape parameter of Vascular Model
λ_l	Lagrange multiplier in Tikhonov regularization
μ	Mean
μ_{lk}	Location parameter of the log-normal distribution
ρ	Density of brain tissue
σ	Standard deviation
σ_{lk}	Shape parameter of the log-normal distribution
τ_b	Time constant for box residue function
τ_e	Time constant for exponential residue function
τ_l	Time constant for linear residue function
ω_0	Larmor frequency
Υ	Regression coefficient
Ω	Ratio factor between control points

Related Publications

1) **Mehndiratta, A.**; Calamante, F.; MacIntosh, B.J.; Crane, D.E.; Payne, S.J.; Chappell, M.A.; Modelling and Correction of Bolus Dispersion Effects in DSC-MRI. *Magnetic Resonance in Medicine*, 2014 (In Press).
2) **Mehndiratta, A.**; Calamante, F.; MacIntosh, B.J.; Crane, D.E.; Payne, S.J.; Chappell, M.A.; Modeling the Residue Function in DSC-MRI simulations: Analytical Approximation to in vivo data. *Magnetic Resonance in Medicine*, 2013 (In Press).
3) **Mehndiratta, A.**, MacIntosh, B.J., Crane, D.E., Payne, S.J., Chappell, M.A.; A Control Point Interpolation method for the Non-Parametric Quantification of Cerebral Haemodynamics from Dynamic Susceptibility Contrast MRI. *NeuroImage*, 2013, 64(1), 560-570.
4) **Mehndiratta, A.**; Park, C.S.; Crane, D.E.; MacIntosh, B.J.; Payne, S.J.; Chappell, M.A.; Quantifying cerebral haemodynamics and maximum potential oxygen delivery in patients with chronic ischemia using DSC perfusion MRI; *22nd Proceeding of International Society for Magnetic Resonance in Medicine (ISMRM)*, May 2014, Milan, Italy. (*Summa cum Laude* Merit Award)
5) **Mehndiratta, A.**; Calamante, F.; MacIntosh, B.J.; Crane, D.E.; Payne, S.J.; Chappell, M.A.; Correction of Bolus Dispersion in the quantification of perfusion and haemodynamics using DSC-MRI; *22nd Proceeding of International Society for Magnetic Resonance in Medicine (ISMRM)*, May 2014, Milan, Italy.
6) **Mehndiratta, A.**; MacIntosh, B.J.; Crane, D.E.; Payne, S.J.; Chappell, M.A.; Quantifying Cerebral Haemodynamics beyond CBF using Control Point Interpolation Deconvolution for

DSC MRI Perfusion Analysis; *21st Proceeding of International Society for Magnetic Resonance in Medicine (ISMRM)*, April 2013, Salt Lake City, Utah, USA.

7) **Mehndiratta, A.**; Calamante, F.; MacIntosh, B.J.; Crane, D.E.; Payne, S.J.; Chappell, M.A.; CBF quantification in the face of dispersion and separation of its effects from normal cerebral haemodynamics: a comparison of deconvolution methods in DSC-MRI; *21st Proceeding of International Society for Magnetic Resonance in Medicine (ISMRM)*, April 2013, Salt Lake City, Utah, USA.
8) **Mehndiratta, A.**; Calamante, F.; MacIntosh, B.J.; Crane, D.E.; Payne, S.J.; Chappell, M.A.; DSC-MRI simulations: what is the correct model for the in vivo tissue residue function?; *21st Proceeding of International Society for Magnetic Resonance in Medicine (ISMRM)*, April 2013, Salt Lake City, Utah, USA.
9) Castellaro, M., **Mehndiratta, A.**, Peruzzo, D., Pillonetto, G., Petersen, E.T, Golay, X., Chappell, M.A.; Cerebral Blood Flow Quantification from QUASAR ASL by Stable Spline; *21st Proceeding of International Society for Magnetic Resonance in Medicine (ISMRM)*, April 2013, Salt Lake City, Utah, USA.
10) Payne, S.J., **Mehndiratta, A.**, Crane, D.E., MacIntosh, B.J., Chappell, M.A.; Quantification of Cerebral Haemodynamics beyond CBF using Non-Parametric CPI Method for Dynamic Susceptibility Contrast MRI; *26th International Symposium on Cerebral Blood Flow, Metabolism and Function (ISCBFM)*, May 2013, Shanghai, China.
11) **Mehndiratta, A.**; Calamante, F.; MacIntosh, B.J.; Crane, D.E.; Payne, S.J.; Chappell, M.A.; Bolus Dispersion in Dynamic Susceptibility Contrast MRI Analysis: Can We Differentiate Dispersion from Normal Cerebral Haemodynamics; *ISMRM Workshop on Perfusion MRI: Standardization, Beyond CBF & Everyday Clinical Applications*, Oct. 2012, Amsterdam, The Netherlands.

12) **Mehndiratta, A.**; MacIntosh, B.J.; Crane, D.E.; Payne, S.J.; Chappell, M.A.; Non-Parametric Quantification of Cerebral Haemodynamics from Dynamic Susceptibility Contrast MRI; *20th Proceeding of International Society for Magnetic Resonance in Medicine (ISMRM)*, May 2012, Melbourne, Australia. (*Summa cum Laude* Merit Award)

13) Chappell, M.A.; **Mehndiratta, A.**; Payne, S.J.; Calamante, F; Bayesian Model-Based Correction for Macro Vascular Signal in Dynamic Susceptibility Contrast Perfusion MRI; *20th Proceeding of International Society for Magnetic Resonance in Medicine (ISMRM)*, May 2012, Melbourne, Australia.

14) **Mehndiratta, A.**; MacIntosh, B.J.; Crane, D.E.; Payne, S.J.; Chappell, M.A.; Improved Vascular Model -Based Analysis for DSC-MRI Perfusion Quantification; *20th Proceeding of International Society for Magnetic Resonance in Medicine (ISMRM)*, May 2012, Melbourne, Australia.

Chapter 1
Introduction

1.1 Clinical background

Cerebrovascular diseases are some of the most devastating diseases in an aging population; along with cardiovascular diseases they constitute the second largest burden on global healthcare [1]. Combined vascular diseases are responsible for 30% of morbidity and mortality worldwide; moreover, in the UK alone, cerebrovascular diseases are responsible for 53,000 deaths every year [1–3]. One class of vascular disease is cerebral ischemia, a condition in which blood supply to the brain is compromised to the extent that it is insufficient to meet the metabolic demand of the tissue. Ischemia is most commonly caused by an occlusion in the supplying blood vessel, leading to poor oxygen supply to the brain cells. This initially results in a loss of cerebral sensory or motor functions and finally to the death of the brain cells, i.e. ischemic stroke.

Stroke management is an emergency procedure. The first 3-6 hours of stroke in evolution are considered to be the window of opportunity [4], as quick and appropriate management is potentially lifesaving during that time. Early diagnosis and treatment can avoid permanent neurological damage which can otherwise leave a patient with permanent disability.

Imaging techniques especially perfusion imaging are used in clinical practice for assessment of vascular diseases in diagnosis and monitoring [5,6]. Given that timely diagnosis of ischemia is crucial for starting appropriate treatment, it is imperative to accurately estimate brain blood perfusion metrics. Many perfusion metrics have relevance in planning the clinical management of

the patient, some of the more important ones being cerebral blood flow, cerebral blood volume, mean transit time and tissue oxygenation.

In addition to tissue perfusion, the blood flow variations within the capillary network referred to as capillary hemodynamics is also of wide research (and clinical) interest. The topological structure of the cerebral arterioles and venules is tree-like branching architecture, while that of the capillaries is like an intricate network [7]. It has been speculated that under conditions of ischemia hemodynamics in the capillary bed are altered which might help to maintain adequate delivery of oxygen and nutrients to the tissue to sustain a normal metabolic activity [8–10]. It has been suggested (using rat models) that variations in tissue hemodynamics through the capillaries might be a useful marker to define tissue under ischemic stress [11,12]. In animal models it has been found that capillary flow become more heterogeneous under conditions of ischemia [11,12]. Logistics to perform such measurements in humans and the clinical significance of these metrics however remains a big challenge. Methods to provide quantitative measurement of hemodynamics might be thus helpful to differentiate healthy tissue from pathology.

1.2 Imaging background

Computed Tomography (CT) and Magnetic Resonance Imaging (MRI) both play a vital role in stroke diagnostics. MRI is recommended, if the time permits, as it offers better contrast and resolution in soft tissues like brain [13,14]. Typically, non-contrast MRI (MRI imaging with no dye) is followed by MRI with a Gadolinium contrast (dye injected intravenously) to demarcate the vascular compromised brain area and to plan the clinical management. Tissue perfusion is a dynamic process and flow of the Gadolinium through the tissue capillary bed allows to measure change in tissue susceptibility as a marker of tissue perfusion. This imaging technique is called Dynamic Susceptibility Contrast MRI (DSC-MRI). Analysis of the images from DSC-MRI is

typically based on an understanding of cerebral microvascular hemodynamics. Many image post-processing methods have been proposed to quantitatively analyze DSC-MRI signals [15–24]. Some of them are used in clinical practice, but all have limitations that affect their accuracy.

Broadly there are two families of solutions for perfusion analysis. One is an analytical model dependent approach, where a predefined tissue response is assumed for further analysis; the tissue response function representing the microvascular hemodynamics in a mathematical functional form [15]. The other is a more flexible non-parametric approach that makes fewer assumptions about the tissue response [16,25] and attempts to learn the true functional form from the data. The potential danger of using a simplified model dependent expression is the possibility of large systematic errors when estimating the tissue response function where the actual underlying function is very different from that being proposed. Hence an analytical approach is rejected by a majority of research studies in favor of non-parametric methods [17].

SVD (Singular Value Decomposition) deconvolution is currently the most robust methodology used in perfusion MRI analysis [26,27]. SVD based deconvolution allows for estimation of the flow values without requiring an assumption about the form of the underlying hemodynamics. However, this method introduces non-physiological oscillations in the tissue response function, and hence it is poor in estimating the actual shape of the function [17]. Despite the fact that the perfusion measurements using this method are not accurate, it is in fact the most robust method in practice, as a result of which it is the present standard technique used commonly in a clinical setting.

Accuracy in perfusion quantification can be improved by constraining the oscillations in the tissue response function. Multiple regularization approaches have thus been attempted with SVD, but a completely smooth tissue response function has not been achieved [17,18,22], neither has there been a significant improvement in perfusion estimation. The non-physiological oscillation in the

calculated tissue response function from SVD methods does not allow the tissue response function to be interpreted for hemodynamic assessment *in vivo*. Other model-based methods including a Vascular Model (VM) permitting a family of shapes for the tissue response function [23] and model-free methods based on likelihood estimation [19], Gaussian process [20] and stochastic modeling [24] have also been tried. These methods guaranteed a smooth tissue response function but no one has demonstrated the capabilities of these methods to measure hemodynamic variations in *in vivo* data so far.

1.3 Thesis outline

The objective of the research presented in this thesis is to quantify cerebral hemodynamics using perfusion MRI by developing an analysis methodology to non-parametrically characterize the tissue response function. The research objective will be achieved by: 1) Studying and understanding the limitations of earlier proposed analysis methods; 2) Designing an accurate, more physiological method with which to perform non-parametric perfusion analysis; 3) Testing this new method for valid clinical questions using simulations; 4) Evaluating the method with clinical cases.

Chapter 2 starts with an introduction to the vascular anatomy and pathophysiology of cerebral ischemia and stroke. The types of stroke, their prevalence and mechanisms of progression will be elaborated. It will be followed by the basics of Magnetic Resonance Imaging related to the brain, including the imaging physics and a historical review of the relevant MR physics of brain perfusion measurements. The key points of MRI perfusion that will be used throughout the other sections will be presented. A literature review of all the major analysis methods related to DSC-MRI analysis will be provided. Included here are details of the DSC-MRI simulation protocols that have been used by various research groups, followed by a detailed discussion on the key methods, their

assumptions, benefits and limitations. The chapter ends with a discussion of these methods and a conclusion.

Chapter 3 describes a new Control Point Interpolation (CPI) method for DSC-MRI analysis. The theoretical framework of the CPI method will be outlined followed by its evaluation in comparison to current standard methods. The evaluation will be performed to assess its accuracy in perfusion estimation and its ability to characterize shape of the tissue response function under pathophysiological variations. Testing will be done by Monte Carlo simulations followed by perfusion analysis of *in vivo* data of a subject with atherosclerotic disease and a healthy control participant. The simulation protocol will be elaborated. The results of the simulations and *in vivo* data will be presented and comparisons will be done for CPI and other methods. This chapter will conclude by discussing the benefits of the proposed CPI method over other methods, and illustrating an example of the capability of the CPI method to show variations in the tissue response function on *in vivo* data which could not have been achieved by earlier methods.

Chapter 4 addresses the issue of bolus dispersion in perfusion analysis. The arterial input function tends to 'smear out' as the blood transit from a larger global artery to smaller and peripheral local artery [28,29]. This deformation in the shape of the arterial input function could be a source of error in perfusion quantification as well altering the hemodynamic assessment of the tissue response function [30]. In this chapter the theoretical background of dispersion correction will be outlined followed by an implementation framework to accommodate dispersion in VM and CPI. An evaluation of methods is done to assess the performance in terms of accurate estimation of perfusion and its ability to distinguish dispersion from pathological variations in vascular hemodynamics. The chapter will conclude by discussing the potential benefits and limitations of various dispersion correction methods that are proposed.

In Chapter 5 CPI and its dispersion variant method will be evaluated on a bigger clinical dataset to explore hemodynamic information obtained from perfusion imaging for potential clinical applications. Perfusion analysis will be performed on a cohort of seventeen subjects with atherosclerotic disease undergoing carotid endarterectomy surgery and two healthy control participants. Perfusion imaging data were acquired for all the patients both pre- and post-surgical intervention. A number of hemodynamic parameters will be extracted from analysis of CPI (and its dispersion variant) and evaluated for clinical interpretation. A ROI based analysis will be performed to compare the changes in hemodynamics pre- and post-surgery. The results of the analysis will be presented and the chapter will conclude with a discussion on the useful hemodynamic information that can now be extracted from DSC-MRI using CPI method and a discussion of its clinical significance.

Chapter 6 concludes this thesis and will present the potential future work. CPI has been found to provide clinically useful information about tissue ischemia and to provide a means to quantify variation in tissue hemodynamics. The CPI method could be used for perfusion analysis of brain tumours, cardiac ischemia and perfusion analysis for Arterial Spin Labeling (ASL) techniques. The future plan for voxel wise cardiac perfusion analysis using the CPI method will be illustrated, showing how quantitative estimation of cardiac hemodynamics might be useful in early diagnosis of heart attack, screening patients for recurrent heart attack and quantifying prognosis after surgical intervention. This chapter will also elaborate current analysis methodologies in ASL, their limitations and how CPI could be a useful technique in addressing some of these challenges.

Chapter 2
Literature Review

2.1 Introduction

Stroke is a neurovascular disorder, characterized by a compromised blood supply, that leads to cerebral ischemia and sometimes a sudden death of brain tissue. Annually about 16 million first-time strokes occur worldwide, causing a total of 5.7 million deaths per year [31,32]. In the European Union an estimated 1.1 million new stroke events occur each year, a figure that is projected to increase to 1.5 million per year by 2025 [33]. Stroke represents one of the major public health problems worldwide, having a death rate of 30% globally [4]. In this chapter the vascular anatomy of the brain and the pathophysiology of cerebral ischemia are elaborated, followed by a literature review on MRI based quantitative perfusion measurement techniques and their challenges.

2.2 Clinical Background on Cerebral Ischemia and Stroke

2.2.1 Vascular Supply of Brain

The brain is a highly vascularized organ, the high demand of oxygen and glucose required by the brain resulting in it having very strong collateral blood supply routes [34]. The brain is supplied by two major arterial systems, internal carotid and vertebral arteries. The arterial Circle of Willis is the channel of arteries interconnecting these two sources of blood supply; hence providing a strong collateral blood supply system to the brain. The internal carotid artery system supplies the major part of the brain (anterior and middle) by three branches: the anterior cerebral artery (ACA), the middle cerebral artery (MCA) and the anterior choroidal artery (AChA). The Vertebro-basilar

system supplies the posterior hemispheres by two posterior cerebral arteries (PCA) and the brainstem and cerebellum by two vertebral arteries along with a midline basilar artery.

2.2.2 Pathophysiology of Cerebral Ischemia and Stroke

Survival and normal functioning of brain is dependent on an adequate supply of oxygen and nutrients via blood while any compromise in cerebral perfusion can result in neuronal cell death, which is classified as neurological stroke. Measurements of perfusion are of direct diagnostic value in vascular disorders, but they also serves as biomarkers for a broader range of physiological and pathological functions. A close coupling between cerebral blood flow (CBF), blood flow rate and metabolism allows regional brain function to be assessed through measurements of cerebral perfusion. A reduction in cerebral perfusion leads to ischemia which is a recoverable state if normal blood supply is restored. However, a massive compromise or complete occlusion of cerebral vessels causes irreversible neuronal death called necrosis or infarction which will initiate a self-destructive mechanism of apoptosis. Within the ischemic cerebrovascular bed there are two zones of injury: the core ischemic zone and the "ischemic penumbra" (an ischemic zone which still contains viable cerebral tissue) [37].

In the core ischemic zone, if blood flow is below 10% to 25% of normal levels [38], the loss of adequate oxygen and glucose results in rapid depletion of energy stores. Severe ischemia results in tissue necrosis which slowly expands; this is called the area of infarction. However, brain cells within the penumbra, a rim of mild ischemic tissue lying between normal tissue and the area of infarction, may remain viable for several hours. The penumbral zone (25% to 50% of normal CBF) [38] attempts to maintain the tissue metabolism by altering its capillary hemodynamics or by recruiting blood supply through collateral vessels. The penumbra tissue is clinically referred to as the "tissue at risk" since the altered hemodynamics or collateral supply is not always adequate in

maintaining the neuronal demand. If reperfusion is not established within a few hours (called the "window of opportunity") the cells in penumbra zone will die. The penumbra is where quick medical interventions are most likely to be effective and hence is the zone of high clinical interest. Studies [37] have proved that severe ischemia kills selectively vulnerable neurons; glial cells may be salvaged if blood flow is restored with early intervention.

2.2.3 Normal Cerebral Perfusion

Cerebral perfusion is defined as the steady-state delivery of nutrients and oxygen via blood to the brain tissue. A close coupling of amount of blood flow to the tissue and the amount of nutrient and oxygen it delivers to tissue has allowed cerebral blood flow to be used as a surrogate maker of tissue perfusion. Normal cerebral blood flow (CBF) is approximately 20 to 100 ml/100g/min but it varies in different parts of the brain [39]. In response to an ischemic incident, the cerebral autoregulatory mechanisms attempt to compensate for reductions in CBF by local vasodilation, increasing oxygen extraction and glucose delivery. These hemodynamic mechanisms attempt to preserve the neuronal activity for a few hours but if sustained the condition will proceed to irreversible damage [38].

2.2.4 Evolution of Stroke

The two mechanisms that cause stroke are ischemia and hemorrhage. 80% of all strokes are ischemic, 10% to 15% are because of non-traumatic intracerebral hemorrhage and the rest are trauma related hemorrhagic in nature [40].

Ischemic Stroke: A blood embolus is defined as a detached intravascular mass (solid, liquid or gaseous) that is capable of blocking the arterial capillary bed (arterial occlusion) distant from its point of origin leading to ischemia of a tissue downstream. A thrombus or an embolus originating from any body organ can potentially lodge in the cerebral circulation. This can partially or

completely occlude a cerebral artery causing ischemia in the affected vascular territory supplied by the artery. Most emboli arising anywhere in the body finally lodge in the middle cerebral artery or its branches because 80% of blood is carried by the large neck artery flow through the MCA. The neuronal injury at the cellular level is governed by tissue hypoxia as well as the building up of cytotoxic waste (cellular metabolic products) which is not cleared by adequate blood supply.

Hemorrhagic Stroke: Head trauma can result in the rupture of deep vessels in the brain which causes blood leakage in the extravascular space leading to hematoma formation. Non-traumatic hemorrhage is also very common which is caused by persistent hypertension or a vessel aneurysm that thin downs the vessel wall slowly and ultimately ruptures. Hematoma formation leads to a cellular reaction (response of the brain cells to blood leakage) which exacerbates its impact on the normal surrounding tissue. Hematoma or its associated edema can raise intra-cranial pressure (ICP) causing additional injury to brain tissue or it can cause occlusion of a major vessel which affects a greater territory with an add-on ischemic stroke.

The research in this thesis mainly focuses on cerebral ischemia with possible applications in the monitoring of patients with ischemic stroke, thus it will be discussed in more detail. It is important to be able to measure cerebral perfusion and hemodynamics in patients with ischemia in order to initiate timely and appropriate treatment. Early diagnosis and treatment can save brain tissue and prevent a long term disability in the patient. Perfusion is classically measured using a diffusible tracer that can exchange between the vascular and tissue compartment. However, in clinical practice, the term ‘perfusion imaging’ has also been applied to a range of quantitative and qualitative measures of hemodynamic properties including blood volume, blood velocity and transit times. Many imaging modalities including Computed Tomography, Magnetic Resonance Imaging and Positron Emission Tomography (PET) have been used for measuring cerebral perfusion. The

most widely accepted ‘gold standard’ imaging modality for quantitative perfusion imaging *in vivo* is PET imaging with ^{15}O-labeled water [41]. The associated radiation risk, cost and unavailability in most clinical centers have, however, limited its wider usage; CT and MRI being most commonly used.

MRI has been used extensively because of its high spatial resolution and soft tissue contrast in the brain [13,14]. MR perfusion imaging can provide maps of brain showing tissue with low perfusion (oligemia) however it does not provide information to differentiate tissue that is already dead (infarct) and tissue under hemodynamic stress (penumbra). Diffusion Weighted Imaging (DWI) is often used in addition to perfusion MRI to identify the brain tissue with infarction. The combination of DWI and perfusion MRI is typically used in clinical practice to identify brain tissue that is under hemodynamic stress and is potentially salvageable, using the diffusion-perfusion mismatch [42,43]. A variety of methods and parameters in perfusion imaging have been used to calculate the presence and degree of mismatch to correlate with region of penumbra [44–50]. This has been further complicated by the recognition that sometimes a portion of hypoperfused tissue does not finally infarct, irrespective of the treatment, and therefore should not be considered as part of the penumbra [44,45]. It has also been established that perfusion imaging provides a conservative estimate of the tissue at risk of infarction [51]. Thus, there is no consensus with respect to what constitutes the diffusion-perfusion mismatch [51,52].

It is possible to measure tissue capillary hemodynamics using perfusion imaging and variations in tissue hemodynamics can possibly help to define tissue under stress [8–10]. The hemodynamics in the capillary network are varied under conditions of stress possibly as a mechanism to maintain adequate oxygen and nutrient delivery to the tissue thus to maintain a normal metabolic activity. It has been shown in rat models that hemodynamic variations are a useful marker of ischemic tissue

[11,12], where it was found that distribution in capillary flow tend to become more heterogeneous in conditions of ischemia. However there has been no subsequent clinical proof to support this hypothesis. There is also a question of how to practically measure capillary hemodynamics using perfusion imaging and what is the clinical significance of these measures. The research in this thesis is motivated by the need to provide means to measure cerebral hemodynamics in ischemia with possible applications in diagnostic and prognostic monitoring of ischemic stroke. It is thus useful to first discuss the concepts of MR perfusion imaging and current analysis methodologies.

2.3 Magnetic Resonance Perfusion Imaging

2.3.1 Physics of MRI

Magnetic Resonance Imaging is a powerful diagnostic imaging tool used for perfusion assessment in the brain in the event of cerebral ischemia and stroke. MRI is based on the resonance phenomenon of protons in an externally applied magnetic field. Each atomic proton nucleus spins around its own axis and this spin motion induces a local magnetic moment. The free magnetic moments of protons are normally randomly oriented in the body cancelling out with no net magnetization. When nuclei are exposed to an external magnetic field (B_0, measured in Tesla), the interaction with the proton's magnetic moment causes many of the nuclei to align in the direction of B_0, while some will align in the direction opposite to B_0. The direction parallel to the main magnetic field is called the longitudinal direction and plane perpendicular to it is called the transverse plane. Once aligned, the magnetic moments from many such protons will cancel out, a slight excess of the protons aligned in the direction of magnetic field producing a "net magnetization" in the longitudinal direction. This net magnetization is the source of MR signal used to produce MR images.

The strong external magnetic field interacts with spinning protons and results in precession of these protons. The frequency at which precession occurs is called the Larmor frequency (ω_0), defined by the Larmor equation:

$$\omega_0 = B_0 \cdot \gamma \qquad \text{Equation 2.1}$$

where γ is the gyro-magnetic ratio (measured in megaHertz per Tesla) which is an atom specific property (e.g., for ^{1}H, $\gamma/2\pi$ = 42.57 MHz/T) [53]. The equilibrium alignment attained after application of B_0, can be disturbed by an application of an electromagnetic gradient in the form of a radio frequency (RF) pulse having radiation energy, *Erf*. The RF pulse must be at the precessional frequency of the protons in order for resonance to occur and for efficient transfer of energy from the RF coil to the protons. The radiation energy is again atom specific,

$$Erf = \hbar \cdot \omega_0 \qquad \text{Equation 2.2}$$

where $\hbar = h/2\pi$, h being Planck's constant [53]. The RF pulse causes the net magnetization to flip by a certain angle (called flip angle) with respect to the longitudinal direction.

T1 Relaxation

Before the RF pulse is applied the net magnetization is in the longitudinal direction, called the longitudinal magnetization. As the energy is absorbed by the protons from the RF pulse, the net magnetization flips away from the longitudinal direction; the net magnetization is now at an angle of FA (Flip Angle) from the longitudinal direction. If FA is 90^0 then all the magnetization is flipped to the transverse plane called transverse magnetization. When the RF energy is switched off the magnetization then begins to grow back in the longitudinal direction. This is called longitudinal relaxation or *T1* relaxation. The rate at which this longitudinal magnetization grows back is different for protons associated with different tissues and is the fundamental source of contrast in *T1*-weighted images. *T1* is a parameter that is characteristic of specific tissue (also dependent on B_0)

and is related to the rate of regrowth of longitudinal magnetization. Longitudinal magnetization can be calculated using:

$$M_z\,(t) = M_0\,(1 - e^{-\frac{t}{T1}}) \qquad \text{Equation 2.3}$$

where M_z is the longitudinal magnetization, M_0 is the maximum longitudinal magnetization, *T1* the longitudinal relaxation time. By definition *T1* is the time that it takes for the longitudinal magnetization to reach 63% of its final value, assuming a 90^0 RF pulse. Figure 2.1 a shows an example of the T1 recovery curve.

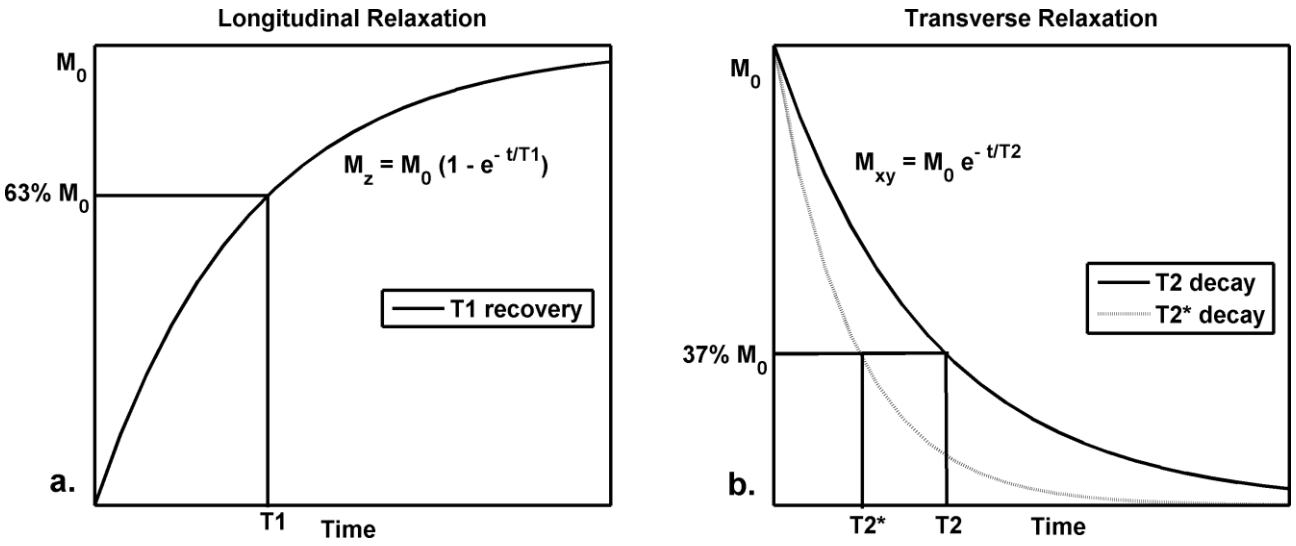

Figure 2.1: a) *T1* relaxation; and b) *T2*/*T2** relaxation showing longitudinal and transverse magnetization components.

T2 Relaxation

When all the spins are flipped in the transverse plane by a 90^0 RF pulse the transverse magnetization, M_{xy}, is at a maximum. Once the RF pulse is switched off, the spins will start to dephase because of spin-spin interaction and the transverse magnetization will start decaying. The transverse magnetization can be calculated using:

$$M_{xy}\,(t) = M_0\, e^{-\frac{t}{T2}}$$ Equation 2.4

where M_{xy} is the transverse magnetization and *T2* the transverse relaxation time. By definition *T2* is the time that it takes for the transverse magnetization to decay to 37% of its original value. The transverse dephasing is also effected by magnetic field inhomogeneity, susceptibility and chemical shift effects, in which case the transverse dephasing is much faster and called *T2** relaxation [54]. *T2** is also called the magnetic susceptibility effect. Different tissues have different value of *T2*/*T2** and these differences are the basis for producing a *T2*/*T2**-weighted contrast in the image. Figure 2.1b shows an example of the *T2* and *T2** decay curve.

Magnetic Susceptibility or *T2**

Dynamic Susceptibility Contrast (DSC or bolus tracking) MR imaging is based on *T2** effects that arise from local field inhomogeneity induced by a Gadolinium contrast agent in the vessels. Gadolinium contrast agents are aqueous solutions of heavy metal Gadolinium based complexes that are injected intravenously. As the contrast flows to the vessels close to the tissue of interest it enhances the transverse relaxation rate (*R2**) of the tissue protons which appears as a fall in the MR signal [55], where *R2** = *1/T2**. Quick repeated image acquisition captures this decrease in signal intensity with contrast agent inflow and a signal recovery as the contrast flows away from the tissue. The effect is very significant in areas where contrast is compartmentalized (since it induces higher gradients) and it is one of the key assumptions in perfusion imaging that the contrast agent will remain within the intravascular compartment throughout its transit from the tissue, thus often being referred to as a single compartment model. Since the bolus passage through the brain parenchyma takes of the order of a few seconds, a very fast image acquisition method is required fully to capture the induced signal change. The most commonly used technique is EPI (echo planer

imaging), which permits a good tradeoff among time resolution (typical Δt ~ 1.5sec), spatial resolution (voxel size ~ 2x2x5mm^3) and volume coverage (~ 10-15 slices).

The change in transverse relaxation rate in a tissue, Δ*R2**, is related to the concentration of the arrival of the contrast agent: the higher the concentration, the larger the change in relaxation rate. For practical purposes most perfusion studies assume a linear relation between the contrast concentration with change in relaxation rate [55–61]:

$$C\ (t) = k \cdot\ \Delta R2^{*}\ (t) \qquad \text{Equation 2.5}$$

where *C(t)* is the time dependent contrast concentration and *k* is the proportionality constant which depends on the tissue type, the contrast agent used, the field strength and the MR pulse sequence.

This change in signal and the concentration time curve (CTC) of the tissue are related by [6]:

$$S\ (t) =\ S\ (t_0)\ \cdot\ (1 -\ e^{-TR \cdot R1})\ \cdot\ e^{-TE\ \cdot\ \Delta R2^{*}(t)} \qquad \text{Equation 2.6}$$

where $S(t_0)$ is the baseline signal in the image prior to the arrival of the bolus, *S(t)* is the signal, *TR* and *TE* are the repetition and echo times respectively, *R1* is the longitudinal relaxation and Δ*R2*(t)* is the change in transverse relaxation over time. The longitudinal relaxation rate (*R1*) is defined as *R1 = 1/T1*. As suggested in the literature [55–61] for practical purposes the *T1* relaxation in DSC imaging can be neglected, thus the CTC and the signal change can be related by:

$$S\ (t) =\ S\ (t_0) \cdot\ e^{-\frac{TE}{k} \cdot C\ (t)} \qquad \text{Equation 2.7}$$

2.3.2 Tracer Kinetic Theory

Analysis of perfusion imaging relies on Tracer Kinetic Theory. According to the tissue vascular topology [7] in the tracer kinetic theory, the microvasculature is modeled as a branching tubular network; bigger arteries dividing into multiple smaller arterioles further dividing into multiple capillaries in the tissue. The capillary bed is modeled as a complex network. It is assumed that an instantaneous bolus injection is performed in the main artery. The injection is defined as an

instantaneous Dirac delta like function produced by the contrast bolus in the artery. When this contrast arrives in the tissue microvasculature, it will be distributed in the capillary bed. This distribution is caused by the multiple paths that the contrast agent can take though the capillary bed. There exist multiple shorter and longer paths in the microvasculature that will guide the amount of contrast flow. Transit time through the tissue is defined as the time taken by a single molecule of contrast to pass through the tissue following an ideal bolus injection. The multiple transit times (corresponding to available multiple paths) through the capillary network can thus be described with a probability density function, *h(t)*. The amount of contrast agent present in the tissue can be calculated as the difference between the total amount of contrast agent injected (input), and the amount of contrast agent that has left the tissue (output). The fraction of the contrast that resides in the tissue at an instantaneous time, *t*, can thus be described as a function of the transit time distribution and is called the residue function.

$$R\,(t) = 1 - \int_0^t h\,(t)\,dt \qquad \text{Equation 2.8}$$

where *h(t)* is the probability density function of transit times and *R(t)* is termed the residue function. According to its fundamental definition the residue function is a monotonically decreasing function with initial value of one i.e. *R(0)=1*; because all the contrast enters the tissue instantaneously and is present in the tissue at that moment, the outflow of the contrast starts only after then.

In reality however the bolus in injection is not instantaneous; the information on how the bolus injection is performed is captured in the shape of the Arterial Input Function (AIF). This shape can be modeled as a series of instantaneous injections and each of these instantaneous injections will result in the contrast agent retention in tissue according to corresponding individual microvascular residue function. The total amount of contrast agent present in the tissue is thus equal to the sum of

all retention values for the series of instantaneous injections. This procedure is mathematically described as *convolution*.

Thus, the contrast concentration in the tissue is not only proportional to total flow to the tissue CBF (Cerebral Blood Flow), but also dependent on how the bolus injection is performed i.e. the Arterial Input Function (AIF), and the tissue capillary hemodynamic properties i.e. the residue function. CTC is linked to the AIF and the residue function through a convolution operation [17,62]:

$$C\,(t) = \frac{\rho}{k_H} \cdot\ CBF\ \cdot\ \left(Ca\,(t) \otimes\ R\,(t)\right)$$

$$= \frac{\rho}{k_H} \cdot CBF \int_0^{\tau} Ca\,(\tau)\ \cdot\ R\,(t-\tau)\,d\tau \qquad \text{Equation 2.9}$$

where, the symbol $\otimes$ represents convolution, *Ca (t)* is the AIF. The proportionality constant, ρ is the density of brain tissue (needed to provide the correct flow units) and $k_H = (1 - H_{art})\,/(1 - H_{cap})$ accounts for the difference in hematocrit (*H*) between capillaries and large vessels, since only plasma volume is accessible to the contrast agent [63].

The total blood supply to this tissue network can be measured as Cerebral Blood Volume (CBV, measured in ml/100g of tissue), Cerebral Blood Flow (CBF, measured in ml/100g of tissue/min) according to the indicator dilution theory [25,62,64–66]. These two parameters are related through the central volume theorem [62,64]:

$$CBV = CBF \cdot MTT \qquad \text{Equation 2.10}$$

where MTT is the Mean Transit Time measured in minutes.

2.3.3 Arterial Input Function

Ideally a true AIF (called local AIF) supplying the tissue of interest is measured for perfusion quantification. However, the shape of the AIF is typically measured *in vivo* in a large artery (internal carotid artery or middle cerebral artery) distant from the true local artery, hence it is called

the global AIF. Measuring global AIF is easy practically as the major arteries have a sufficiently large lumen to be seen with the spatial resolution of a typical MR image. The shape of the AIF is assumed to remain unaltered during the transit of the tracer from the measured global AIF to the level of the true local arteriole supplying the tissue. However, the non-consideration of tracer delay and assumption of no change in shape of AIF in transit can affect the accurate estimation of perfusion.

2.3.4 Quantification of Cerebral Blood Flow

Quantification of cerebral perfusion metrics (CBV, CBF and MTT) requires the inversion of Equation 2.9, a mathematical process called deconvolution [17]. The CTC, *C(t)*, is calculated from Equation 2.7 by measuring the signal, *S(t)* and $S(t_0)$, in the MR image, which has to be deconvolved with respect to the AIF, *Ca(t)*, that is also measured from the MR image as the signal in the main artery supplying the tissue of interest. After deconvolution the result is the scaled residue function, CBF · *R(t)*, known as the Tissue Response Function, TRF.

$$TRF\ (t) = CBF\ \cdot\ R\ (t) \qquad \text{Equation 2.11}$$

Once the TRF has been calculated, perfusion parameters can be obtained from its maximum value, as *R(0)=1* by definition [17]. TRF estimation can be performed either with a model-based method or with model-free and non-parametric method.

Under well-mixed compartment model assumptions, on arrival of the contrast to the tissue there is an instant mixing of the contrast with the tissue blood compartment. This results in the concentration of contrast at venous outflow being proportional to the mean concentration of the tissue capillary blood pool, this being called a well-mixed single compartment model. The residue function is an exponential decay function under such model conditions [64,66]. The Fermi function and Lorentzian functions are also commonly used for estimation of TRF [22][21]; however validity

of these model assumptions for analysis of *in vivo* data is questionable especially under pathological variations. The Vascular Model (VM) permits a family of shapes for the residue function under pathophysiological variation [23] and is discussed in detail under the analysis of perfusion imaging section below.

The other approach for empirical estimation of TRF is a model-free one with no model assumptions, through the process of deconvolution. Deconvolution for TRF estimation is an ill-posed inverse problem: thus even a little noise or small alterations in the CTC will have a large impact on the calculated tissue response function and hence perfusion estimates (CBF, CBV, MTT). Thus deconvolution has been a major challenge in perfusion imaging assessment.

An ideal deconvolution algorithm should be able to provide an estimation of perfusion under all experimental and tissue hemodynamic variations. The process should be computationally fast, easy to use in a clinical environment and accurate. The details of the model-based and model-free deconvolution methods will be discussed below under the analysis methods for perfusion quantification section.

2.3.5 Quantification of Cerebral Blood Volume

DSC-MRI can not only provide an estimate of CBF but also of other perfusion parameters. The Cerebral Blood Volume (CBV) is proportional to the area under the concentration time curve of tissue for first circulation (first peak) [17]. The value is normalized to the area under the AIF to account for the fact that, independent of the CBV, if more tracer is injected a greater concentration will reach the tissue:

$$CBV = \frac{\int_0^\infty C\,(t)dt}{\int_0^\infty Ca\,(t)dt} \qquad \text{Equation 2.12}$$

2.3.6 Quantification of Mean Transit Time

Mean Transit Time, MTT, is the average time for a contrast molecule to pass through the tissue vasculature following an ideal bolus injection. MTT can either be calculated as mentioned earlier, based on the central volume theorem in Equation 2.10 [17] or calculated from the area under the curve of the residue function [39,67,68]:

$$MTT = \int_0^\infty R(t)dt \qquad \text{Equation 2.13}$$

Hence, it can also be calculated from the Tissue Response Function (*TRF (t) = CBF · R (t)*), where TRF_{max} is its maximum value:

$$MTT = \frac{\int_0^\infty TRF(t)dt}{TRF_{max}} \qquad \text{Equation 2.14}$$

2.3.7 Dispersion in the Arterial Input Function

The AIF represents the concentration of the tracer entering the tissue at time *t*. The assumption of no delay and of no change in the shape of AIF from the measured global location to the local arteriole level is often not realistic. The AIF is often delayed and 'smeared out' during transit resulting in a reduction in peak amplitude and a broadening of the AIF shape, called bolus delay and dispersion respectively [29,69,70]. If these effects are not considered in the estimation routine, they can lead to considerable errors in the quantification of the perfusion parameters [29], which can have serious implications for diagnosis and management of a patient with cerebral ischemia.

Various mathematical solutions have been proposed to correct for bolus dispersion by adding a Vascular Transport Function (VTF) in the perfusion analysis [28,30,71] Equation 2.9 is thus rewritten as:

$$C\,(t) = \frac{\rho}{k_H} \cdot\ CBF\ \cdot \left(Ca\,(t) \otimes VTF(t) \otimes\ R\,(t)\right) \qquad \text{Equation 2.15}$$

where *Ca(t)* is now the measured AIF and *VTF(t)* is the vascular transport function. The VTF is sometimes also referred to as the dispersion kernel because it captures the dispersion information that affects the AIF when the blood transits from the large artery where the AIF is measured to the local tissue artery. A few models of VTF have been proposed in the literature [28,29,71–76]. Since convolution follows the associative law, the VTF could be instead convolved with the residue function (keeping AIF unaltered) to associate the effects of dispersion with the residue function. In that case, the *measured* residue function might no longer start from one [29,69].

The ideal solution for this problem might be to bypass the effects of dispersion by using a local AIF, i.e. choosing the AIF as close to the tissue as possible, for perfusion quantification, this could minimize both the delay and dispersion arising in bolus transit [77]. The approach is highly sensitive to partial volume effects, giving poor spatial resolution and leading to no differentiation of vessels and tissue voxel, but a couple of solutions have been proposed to solve this issue [78–80] . However, presently there is no ideal model which completely incorporates the effects of dispersion in AIF calculations.

2.4 MR Perfusion Simulation

In this section the process of simulating DSC-MRI data which has been well established over the last 15 years is discussed. Validation of a new method for analysis of DSC-MRI using such Monte Carlo simulations is essential before it can be tested in patient images by a pilot clinical study. Figure 2.2 shows the steps in signal simulation and analysis for typical MR perfusion study.

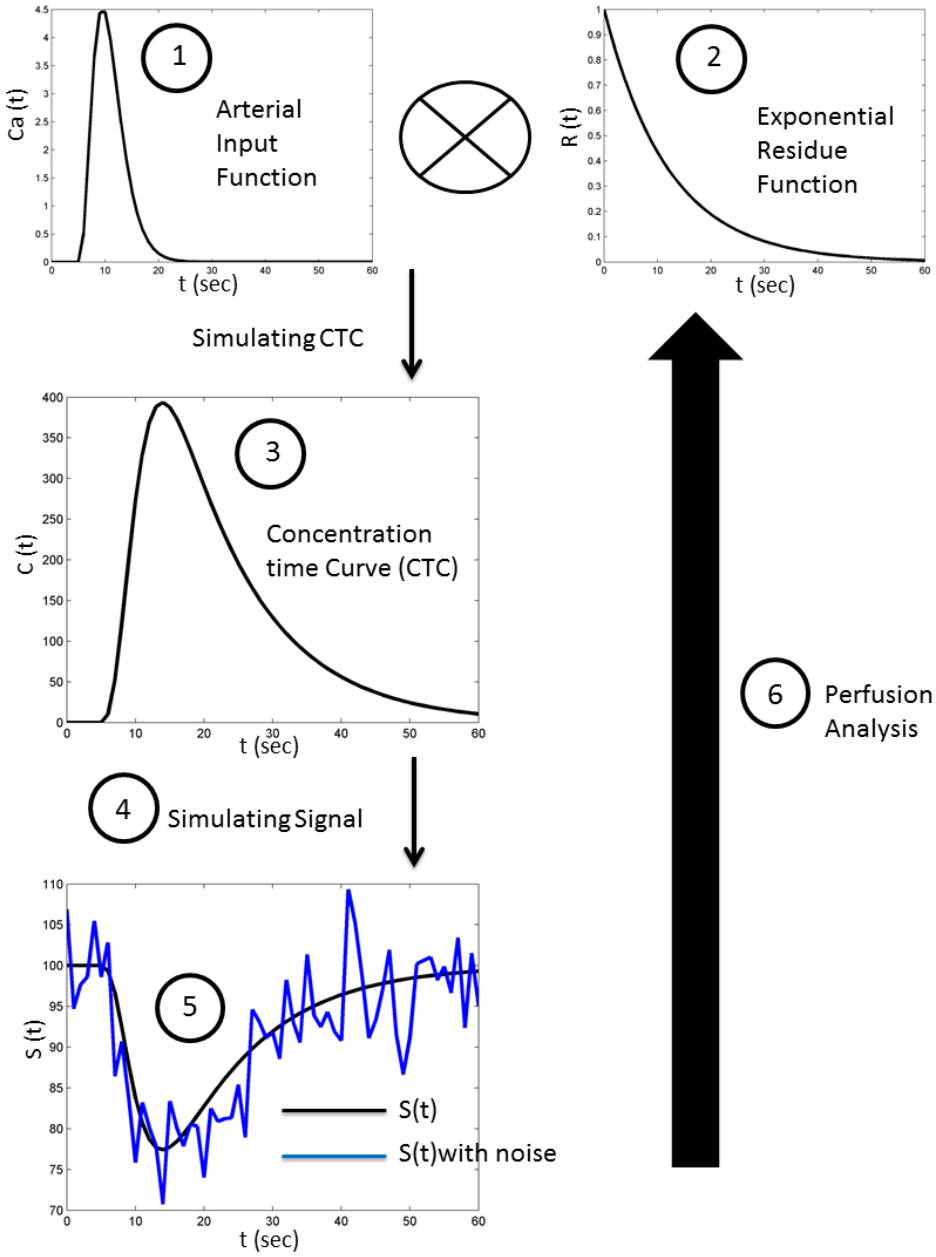

Figure 2.2: Simulation protocol for DSC-MRI analysis studies includes simulation of typical perfusion MRI signal (step 1-5) followed by analysis (step 6). Step 1: Simulate AIF; Step 2: Simulate residue function; Step 3: Simulate CTC; Step 4: Simulate signal; Step 5: Add Noise; Step 6: Analysis.

These steps are:

1. Simulate an AIF;

2. Simulate a residue function with typical MTT values;
3. Simulate a concentration time curve by convolution of the AIF with the residue function and scaling factor of typical CBF value;
4. Convert the concentration time curve to the signal time curve based on a linear relationship between the vascular concentration of the contrast agent and the susceptibility contrast;
5. Add noise to signal: Gaussian noise is normally assumed and added to the signal based on a typical signal to noise ratio observed in clinical settings.

2.4.1 Simulating Arterial Input Function

In all simulation studies an arterial input is used with a shape and size that is typically obtained from a standard instantaneous bolus injection. This was first developed in 1994 by adjusting the parameters of a gamma-variate function to resemble the averaged bolus size and shape observed in the large vessels of six normal volunteers in a clinical study [81]. Since then all the Monte Carlo simulations have used the same gamma-variate function with recommended parameters for AIF simulation:

$$Ca\,(t) = \begin{cases} 0 & t \le t_0 \\ a \cdot (t - t_0)^b \cdot e^{-\frac{t-t_0}{c}} & t > t_0 \end{cases} \qquad \text{Equation 2.16}$$

where *Ca(t)* is the concentration of the contrast in the artery, t_0 is the bolus arrival time and *a*, *b* and *c* are constants. Typical values of these constants are: *a*=1, *b*=3, *c*=1.5.

2.4.2 Simulating Tissue Residue Function

There is a set of residue functions published in the literature which also represents the extremes of potential residue shapes *in vivo*. The most popular residue functions are described below and illustrated in Figure 2.3. MTT calculation for these residue functions can be analytically performed as shown in Table 2.1.

1) **Exponential residue function:** The exponential residue function describes a well-mixed single compartment model with the assumption of an instantaneous mixing of the contrast on arrival to the tissue blood compartment [15,64,66]. The exponential residue function is described with a time constant τ_e.

$$R\,(t) = e^{\frac{-t}{\tau_e}} \qquad \text{Equation 2.17}$$

2) **Linear residue function:** This residue function is described as a linear decay [17,18] with time constant τ_l.

$$R\,(t) = \begin{cases} 1 - \dfrac{t}{2 \cdot \tau_l} & t \leq 2 \cdot \tau_l \\ 0 & t > 2 \cdot \tau_l \end{cases} \qquad \text{Equation 2.18}$$

3) **Box residue function:** This residue function describes a vascular bed with "plug" flow where the capillaries are described in parallel with equal length and time constant τ_b [17,18]:

$$R\,(t) = \begin{cases} 1 & t \leq \tau_b \\ 0 & t > \tau_b \end{cases} \qquad \text{Equation 2.19}$$

4) **Lorentzian residue function:** The residue function is described by a Lorentzian shape curve [22] with time constant β_{lrz}:

$$R\,(t) = \frac{1}{1 + \left(\dfrac{t}{\beta_{lrz}}\right)^2} \qquad \text{Equation 2.20}$$

5) **Fermi residue function:** The residue function is described by a Fermi shape curve [82] with two free parameters μ_f and κ_f:

$$R\,(t) = \left(1 + e^{\frac{-\mu_f}{\kappa_f}}\right) / \left(1 + e^{\frac{t-\mu_f}{\kappa_f}}\right) \qquad \text{Equation 2.21}$$

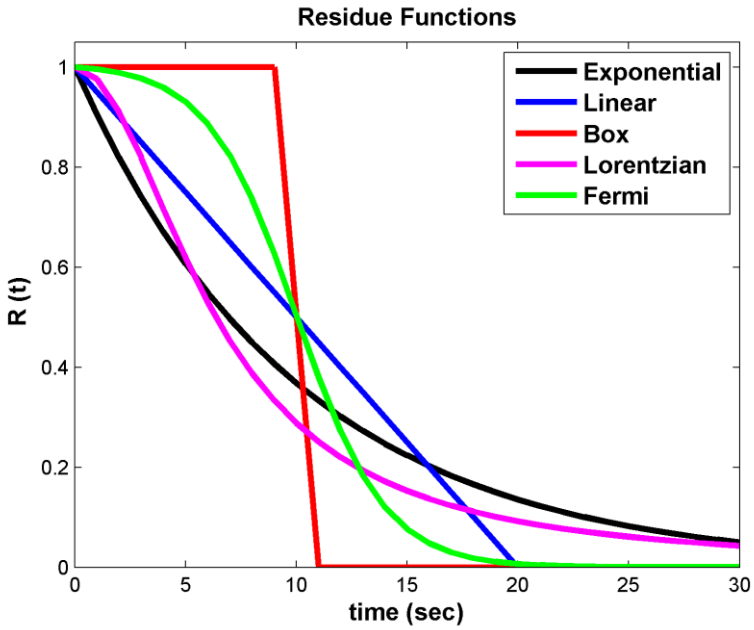

Figure 2.3: Illustrates an example of Exponential, Linear, Box, Lorentzian and Fermi residue function.

Table 2.1: Analytical residue functions, functional free parameters and mean transit time.

Residue Function	Free parameters	Mean Transit Time
1) Exponential	τ_e	τ_e
2) Linear	τ_l	τ_l
3) Box	τ_b	τ_b
4) Lorentzian	β_{lrz}	$\frac{\pi}{2}\beta_{lrz}$
5) Fermi	μ_f, κ_f	$\left(1+e^{\frac{-\mu_f}{\kappa_f}}\right)[\mu_f+\kappa_f \ln\left(1+e^{\frac{-\mu_f}{\kappa_f}}\right)]$

τ_e – time constant for Exponential function

τ_l – time constant for Linear function

τ_b – time constant for Box function

β_{lrz} – time constant for Lorentzian function

μ_f & κ_f – Fermi function parameters

2.4.3 Simulating Tissue Residue Function with Dispersion

The dispersion effect can be described mathematically as a convolution of *R(t)* with a vascular transport function (VTF):

$$R_{disp}\,(t) = R\,(t) \otimes VTF\,(t) \qquad \text{Equation 2.22}$$

Normally $R(0)=1$ and $\int_0^\infty R(t)\,dt = MTT$ but with dispersion $R_{disp}(0)=0$ and $\int_0^\infty R_{disp}(t)\,dt = MTT$ after VTF is normalized such that area under VTF is one. Three VTFs have been commonly used in the past to model the effect of dispersion.

1) An Exponential Dispersion Kernel (EDK) [28,29]:

$$EDK\,(t) = \frac{1}{\theta} \cdot e^{-t/\theta} \qquad \text{Equation 2.23}$$

where θ represents a time constant for the exponential dispersion kernel, such that the larger the value of θ, the larger the dispersion, and in the limit θ → 0, *VTF(t)* tends towards the Dirac delta function with no dispersion [29].

2) Gamma Dispersion Kernel (GDK) [83]:

$$GDK\,(t) = \frac{s^{1+sp}}{\Gamma\,(1+sp)} \cdot t^{sp} \cdot e^{-st} \qquad \text{Equation 2.24}$$

where *s* characterizes the "sharpness" of the kernel and *p* is the time-to-peak. When *p*=0 and *s* → ∞ this kernel approximates a delta function resulting in zero dispersion; whereas with larger values of *p* and smaller values of *s* the kernel will be associated with a greater amount of dispersion [83]. It is also noteworthy that EDK is a special case of GDK when *p*=0.

3) Log-Normal Dispersion Kernel (LNDK) [76]:

$$LNDK\,(t) = \frac{1}{t\sigma_{lk}\sqrt{2\pi}}\; e^{-\frac{1}{2\sigma_{lk}^2}(\ln t-\mu_{lk})^2} \qquad \text{Equation 2.25}$$

where μ_{lk} and σ_{lk} are the mean and standard deviation of the normally distributed ln(t). In the dispersion kernel μ_{lk} is the location parameter that must be a real number and σ_{lk} is the shape parameter with values greater than zero.

2.4.4 Simulating Perfusion Parameters

Values of CBV, CBF and MTT are simulated in agreement with the central volume theorem (Equation 2.10). CBF is typically simulated from 10 ml/100g/min to 70 ml/100g/min in steps of 10 ml/100g/min for grey matter and from 5 ml/100g/min to 35 ml/100g/min in steps of 5 ml/100g/min for white matter. CBV for grey matter is considered to be 4% (4 ml/100g) and 2% (2 ml/100g) for white matter [84]. Thus simulated MTT typically is in the range 3.43 s to 24 s.

2.4.5 Simulating Signal Time Curve

CTC is calculated as described in Equation 2.9. For practical purposes, in simulations ρ/k_H is considered to be one, where ρ/k_H indicates the measure of brain tissue density and difference in hematocrit between capillaries and large vessels (as described already). CTC is converted to the signal curve as described in Equation 2.7.

2.4.6 Simulating Signal Noise

Gaussian noise is typically added to the signal with a signal to noise ratio (*SNR*) of 20 to100 which represents the range of clinical image noise, *SNR*=100 representing the best possible quality clinical image, *SNR*=50 the best image quality which can be obtained practically and *SNR*=20 simulating a typical clinical image DSC MRI signal. *SNR* is here defined as the ratio of the baseline signal and the standard deviation on the noise, hence is called the baseline SNR:

$$SNR = \frac{S\,(t_0)}{\sigma\,(noise)} \qquad \text{Equation 2.26}$$

2.5 MR Perfusion Analysis

The section below describes the most frequently used analysis methods in perfusion imaging, their assumptions, benefits and limitations.

Analysis approaches are divided into two main categories: model-based and model-free. Various deconvolution methods have been proposed under both model-based and model-free analysis methodologies. These include:

I. Model based methods
    1. Exponential [15,64,66]
    2. Fermi [82]
    3. Vascular Model [23]

II. Model-free methods
    1. Frequency domain deconvolution (Fourier Transform) [16,25]
    2. Singular Value Decomposition (SVD) [17]
    3. Block-circulant SVD (oSVD) [18]
    4. Tikhonov Regularization (tkSVD) [22]
    5. Maximum Likelihood [19]
    6. Gaussian Processes Deconvolution [20]
    7. Nonlinear Stochastic Regularization [24]

In model-based techniques, a specific analytical expression or shape of *R(t)* is assumed, most often exponential [15,64,66] or Fermi [82]. The perfusion analysis problem can, at least in theory, be circumvented by performing non-parametric deconvolution without *a priori* knowledge of *R(t)*. These are model independent approaches, where the tissue response function, i.e. the flow and shape of *R(t),* are determined from the data. These deconvolution methods will now be explained.

2.5.1 Exponential and Fermi Model

A model for the residue function is presumed for the tissue and analysis is performed using this specific model. Often an exponential shape for the residue function, Equation 2.17, is considered an appropriate choice as it models a single well-mixed compartment model for the tissue capillary bed [15,64,66]. In the exponential model the contrast once arrived in the tissue is considered to mix with the blood instantaneously such that the concentration of the contrast in the tissue blood is the same as the concentration in the venous outflow. It is still one of the widely used models for use in simulation studies.

The Fermi function, Equation 2.21, has also been found to be an appropriate model for tissue hemodynamics and thus is still used in cardiac perfusion imaging [21,82]. The presumption of a specific shape for *R(t)* imposes assumptions on the tissue microvasculature hemodynamics which cannot be known ahead with sufficient precision, especially in pathology. It is also found to have considerable amounts of error in the estimation of perfusion when the actual underlying tissue residue function cannot be characterized with the model expression considered. For this reason the complete model-based approach is not very popular currently.

2.5.2 Vascular Model

Motivated to improve CBF estimation by a proper characterization of the shape of the residue function, a Bayesian approach was proposed by Mouridsen et al. with a new model based methodology, the Vascular Model (VM) [23]. The choice of the Bayesian method allowed for incorporation of prior knowledge about the estimated parameters of the model.

The Vascular model assumed a parallel distribution of capillaries supplied by a feeding arteriole to the tissue with the gamma distribution function used to parameterize the tissue transit time distribution, *h(t)*:

$$h\,(t;\,\alpha,\beta) = \frac{1}{\beta^{\alpha}\,\cdot\,\Gamma\,(\alpha)}\,\cdot\,t^{\alpha-1}\,\cdot\,exp^{\,-t/\beta}\;;\;\alpha,\beta > 0 \qquad \text{Equation 2.27}$$

where, α (>0) is the shape and β (>0) the scale parameter. The gamma distribution is very flexible and covers a wide range of shapes in the residue function. An exponential residue function can be achieved at α =1 and a box function at approximately α =100.

The product of the two parameters of the gamma distribution is the mean of the distribution, which in this case is the mean transit time. To ensure that the product of α and β is the MTT, α was replaced with a shape parameter λ such that, α=λ and β= MTT/λ. MTT was calculated using the central volume theorem, CBV being calculated directly from the data as the ratio of the area under CTC and AIF, using Equation 2.12, and CBF was a free parameter in the VM. The residue function was calculated from *h(t)* using Equation 2.8. Thus *R(t)* in the VM was parameterized by only two free parameters, CBF and shape parameter λ. To correct for bolus arrival delay a third parameter, δ, was introduced in the VM, the AIF was moved temporally by δ units, thus making the VM bolus arrival delay insensitive. Figure 2.4 shows the architecture of the vascular model which can be considered as a single input and single output system, the free parameters of the complete model being CBF, λ and δ. The parameters were estimated with a Bayesian framework using a Levenberg–Marquart type Expectation–Maximization (EM) algorithm.

The Bayesian approach incorporates prior information for the vascular model; results from model-free oSVD method (explained below) were used as prior information for parameters of the VM. The maximum of the estimated tissue response function from oSVD was used as a prior on CBF and the location of the maximum as a prior on δ and λ had a prior value of 10, modeling a smoothly decreasing residue function.

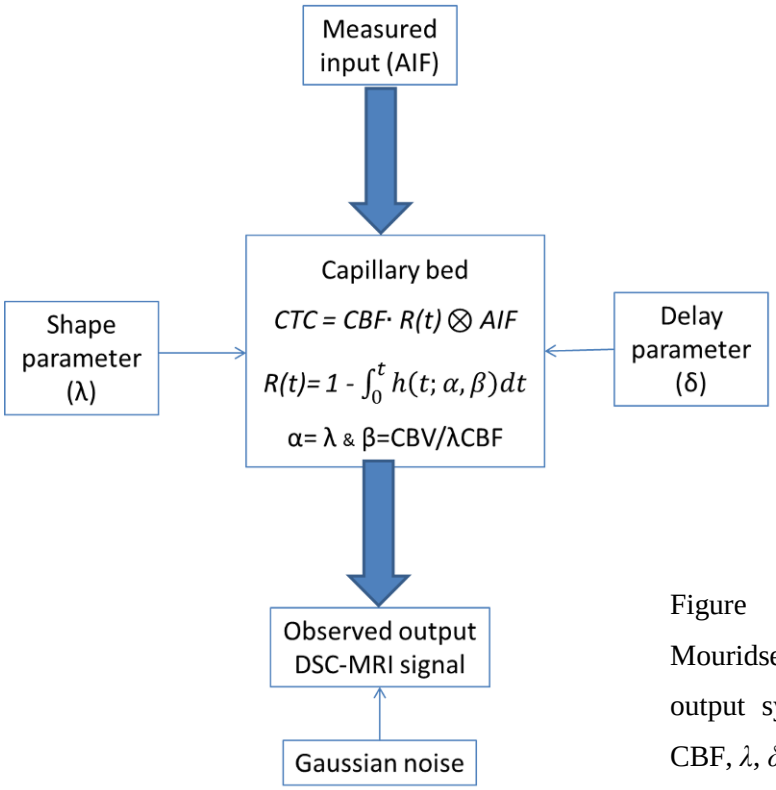

Figure 2.4: Vascular model proposed by Mouridsen et al. [23] as single input and single output system controlled by model parameters CBF, λ, δ.

VM showed a good variability in shape for *R(t)* depending on selection of the shape parameter λ. Simulations showed that VM was able to characterize the residue function in agreement with the true curves. At a high SNR of 100, VM estimated flow values were in good agreement with true values. However, at a more realistic *SNR* of 20, an underestimation for CBF was observed with VM. VM showed considerable underestimation in CBF with the simulated delay in the bolus arrival.

2.5.3 Fourier Transform Approach

The transform based approach was initially proposed by Rempp et al. [16] in 1994 and was one of the initial attempts to quantify perfusion using DSC-MRI. In this approach the convolution theorem of the Fourier Transform (*FT*) was used, where the residue function and flow were determined by taking the inverse Fourier Transform (FT^{-1}) of the ratio of the transforms of the AIF and CTC:

$$\frac{\rho}{k_H} \cdot \mathrm{CBF} \cdot R(t) = FT^{-1}\{\frac{FT\{\,\mathrm{C\,(t)}\,\}}{FT\{\,\mathrm{Ca(t)}\,\}}\} \qquad \text{Equation 2.28}$$

Since this approach was found to be very sensitive to noise, a frequency domain filtering process (Wiener filter) was used before performing the inverse *FT*. The perfusion estimates calculated using this approach were found to be in the expected physiological range but were slightly overestimated compared to the standard PET imaging [16].

2.5.4 Non-parametric Deconvolution using Singular Value Decomposition

Ostergaard et al. originally proposed two subcategories of the deconvolution techniques for perfusion quantification: transform approach and algebraic approach [17]. In the transform approach the convolution theorem of the Fourier transform (*FT*) was used as suggested by Rempp et al. [16] but it was found that by taking the *FT* of the AIF and the CTC, noise was represented at high frequencies whereas the "*real*" physiological signal has more power in lower frequencies. An automated filtering process described by Gobbel and Fike [25] was thus implemented which dynamically increases the strength of the filter until a global constraint on the degree of oscillation is fulfilled. It has been shown in [17,85] that this transform approach is very close to the algebraic approach (described below).

The algebraic approach was based on an algebraic reformulation of the convolution process and has been used extensively in the analysis of tissue response functions. The AIF and CTC are measured at a set of equally spaced *($\Delta t \approx TR$)* time intervals, with an assumption that over small time intervals, Δt, the residue function and arterial input functions are constant. *TRF(t)* in the following equations represents the tissue response function as in Equation 2.11. The convolution expression of CTC can be reformulated to an algebraic expression as:

$$C\,(t) = \left(Ca\,(t) \otimes\ TRF\,(t)\right) = \int_0^{\tau} Ca\,(\tau)\ \cdot\ TRF\,(t-\tau)\,d\tau\ \approx\ \Delta t \sum_{i=0}^{j} Ca\,(t_i)\ \cdot TRF\,(t_j -\ t_i)$$

Equation 2.29

This can be expressed in matrix form as:

$$\begin{pmatrix} C(t_1) \\ C(t_2) \\ \cdots \\ C(t_n) \end{pmatrix} = \Delta t \begin{pmatrix} Ca(t_1) & 0 & \cdots & 0 \\ Ca(t_2) & Ca(t_1) & \cdots & 0 \\ \cdots & \cdots & \cdots & \cdots \\ Ca(t_n) & Ca(t_{n-1}) & \cdots & Ca(t_1) \end{pmatrix} \cdot \begin{pmatrix} TRF(t_1) \\ TRF(t_2) \\ \cdots \\ TRF(t_n) \end{pmatrix}$$

Equation 2.30

which, can in turn be written in vector notation as:

$$\mathbf{c} = \mathbf{Ab}$$

Equation 2.31

Here **c** is the measured tissue tracer concentration (*C(t)*), **A** is the arterial input function and **b** is the tissue response function. This equation can be solved for **b** by calculating the inverse of **A** such that $\mathbf{b}=\mathbf{A}^{-1}\mathbf{c}$. The 'inverse' of **A** can be calculated using a SVD technique. Using SVD the matrix **A** is decomposed into three matrices **U**, **S** and **V** such that:

$$\mathbf{A} = [\mathbf{U} \cdot \mathbf{S}\ \cdot \mathbf{V}^{\mathrm{T}}]$$

Equation 2.32

where, **S** is a diagonal matrix of singular values and **U** and **V** are eigenvectors for the corresponding singular values.

The (pseudo-) inverse of **A**, $\mathbf{A}^{+}$, can be computed using SVD as [86]:

$$\mathbf{A}^{+} = \mathbf{V} \cdot \mathbf{W} \cdot\ \mathbf{U}^{\mathrm{T}}$$

Equation 2.33

where **W** is a diagonal matrix and is the pseudo-inverse of **S**. **W** is formed by replacing every non-zero diagonal entry of **S** by its reciprocal and transposing the resulting matrix, **V** and **U** are orthogonal matrices. After calculating $\mathbf{A}^{+}$, **b** is found from:

$$\mathbf{b} = \mathbf{V} \cdot \mathbf{W} \cdot (\mathbf{U}^{\mathrm{T}} \cdot \mathbf{c}) \qquad \text{Equation 2.34}$$

However this method is found to be extremely sensitive to noise in **c**. By eliminating diagonal elements below a set threshold value in **W**, non-physiological oscillations in **b** can be minimized. This is equivalent to calculate and minimize $\| A \cdot b - c \|_2$, where $\| \cdot \|_2$ denotes the L_2 norm (minimizing sum of squared errors). The process of dampening oscillations is known as regularization and the set threshold used in the method was referred to as *Psvd*. The method is commonly known as standard SVD (sSVD) or truncated SVD (tSVD). This method was found to be robust for wide ranges of physiological flow and MTT values and to be relatively independent of the underlying residue function. However, it was very sensitive to delay in bolus arrival and noise, these being reflected as significant non-physiological oscillations in the estimated tissue response function shape. These oscillations have hampered the use of the tissue response function for estimation of hemodynamic information such as the transit time distribution.

The popular sSVD method for calculating CBF and MTT in perfusion imaging by deconvolving the tissue signal from first pass bolus with an AIF has been widely accepted. The method was very sensitive to noise, bolus delay and dispersion, leading to significant underestimation of the perfusion metrics [17,18]. Also sSVD was unable to correct for negative delay, if the bolus arrives in the tissue before the selected AIF (i.e. the tissue of interest is not fed by the selected AIF but by another fast flowing collateral vessel). Whilst the Fourier technique was insensitive to delay, it has been shown to be a poor estimator of high flow rates in lower SNR conditions [17].

2.5.5 SVD using block-circulant Deconvolution Matrix

Block-circulant SVD (oSVD) method proposed by Wu et al. [18] attempted to compensate for some of the limitations of sSVD. It improved the flow estimates in two ways:

- Deconvolution with a block-circulant matrix reduced the sensitivity to bolus arrival delay;

- Local regularization improved the estimated shape of the tissue response function.

Instead of performing a linear deconvolution for an inverse matrix problem after representing the convolution equation in a discretized matrix format (Equation 2.30), Wu et al. proposed a circular deconvolution to solve the problem of bolus delay. Circular convolution has been shown to be equivalent to linear convolution with time aliasing, and mathematically the same as a standard inverse Fourier method [87]. Time aliasing was avoided by zero-padding the time points in *Ca(t)* and *C(t)* to length *L*, where $L \geq 2N$, *N* being the total number of time points in the CTC. Thus replacing matrix **A** (Equation 2.31) with a block-circulant matrix, **D**, such that:

$$\mathbf{D}_{i,j} = \begin{cases} \mathbf{A}_{i,j} & \text{if } j \leq i \\ \mathbf{A}_{L+i-j,0} & \text{otherwise} \end{cases} \qquad \text{Equation 2.35}$$

Equation 2.31 can be reformulated as $\mathbf{g} = \mathbf{D} \cdot \mathbf{f}$, where **g** is the zero padded *C(t)* and **f** is the tissue response function. **f** can thus be calculated using a SVD approach:

$$\mathbf{D}^{+} = \mathbf{V}_c \cdot \mathbf{W}_c \cdot \mathbf{U}_c^{T} \qquad \text{Equation 2.36}$$

$$\mathbf{f} = \mathbf{D}^{+} \cdot \mathbf{g} = \mathbf{V}_c \cdot \mathbf{W}_c \cdot (\mathbf{U}_c^{T} \cdot \mathbf{g}) \qquad \text{Equation 2.37}$$

When using circular deconvolution, due to discontinuities at *t=0* and *t=L*, leakage frequencies were amplified giving rise to spurious oscillations. Increasing *Psvd* (the threshold for diagonal matrix regularization) could potentially reduce these oscillations. Wu et al. also proposed a local regularization parameter, the Modified Oscillation Index (*OI*), as described by Gobbel and Fike [25], to control these oscillations by varying *Psvd* until the estimated tissue response function's oscillation index falls below a pre-specified value:

$$OI = \frac{1}{L} \cdot \frac{1}{\mathbf{f}_{max}} \cdot \left(\sum_{k=2}^{L-1} \left| \mathbf{f}(k) - 2\mathbf{f}(k-1) + \mathbf{f}(k-2) \right| \right) \qquad \text{Equation 2.38}$$

where $\mathbf{f}_{max}$ is the maximum amplitude of **f** and *L* the number of sample points after zero padding.

Wu et al. compared sSVD with circulant SVD (cSVD) (using *Psvd* regularization) and block-circulant SVD (oSVD) (using the circulant matrix with *OI* for regularization). The performance of sSVD, cSVD and oSVD was found to be comparable in estimating CBF, similar underestimation of CBF values at lower MTTs being observed with all three. The underestimation of CBF was however more pronounced at low *SNR*. oSVD demonstrated some benefits compared to cSVD and sSVD in reducing the oscillations in the estimated TRF because oSVD optimized the regularization threshold for each signal curve rather than assuming a global threshold (*Psvd*). This improvement was in accordance with another study by Liu et al. [88] which promoted an adaptive threshold for DSC analysis. However, a completely smooth tissue response function was still not achieved with the oSVD method. To improve the CBF estimates, Wu et al. recommended two *OI* values based on signal *SNR*, *OI* values of 0.065 and 0.035 were suggested at *SNR* of 100 and 20 respectively [18]. Another advantage of block-circulant deconvolution was that it was found to be time insensitive for both negative and positive delay in the AIF.

2.5.6 SVD with Tikhonov Regularization

To improve the CBF estimation and to reduce the undesired oscillations in the residue function with sSVD method there has been one more regularization technique suggested, by Calamante et al., using Tikhonov regularization with the L-curve criterion [22]. Tikhonov regularization (tkSVD) added a side constraint to stabilize the solution to an ill-posed problem [89,90]. The term which stabilizes the solution was $\lambda_l^2 \|\mathbf{L_p b}\|^2$, where $\mathbf{L_p}$ is a penalty matrix chosen based on prior information (e.g. non-oscillating smooth *R(t)* in this case) and λ_l the Lagrange multiplier, the regularization parameter in the Tikhonov technique. The selection of λ_l is the most critical step in Tikhonov regularization, for which the corner of the L-curve [89] was chosen. This curve displays the trade-off between minimizing the residual norm ($\|\mathbf{Ab-c}\|$) and the constraint norm ($\|\mathbf{L_p b}\|$). The

corner of the curve (the point of maximum curvature) was found to give the best parameter for optimal regularization.

The Tikhonov regularization method thus involved minimizing a weighted combination of the residual norm and the side constraint:

$$r_\lambda = min\{\|\mathbf{Ab} - \mathbf{c}\|^2 + \lambda_l^2 \|\mathbf{L_p b}\|^2\} \quad \text{Equation 2.39}$$

The matrix $\mathbf{L_p}$ introduces a "penalty" if the **b** behaves undesirably (with large oscillations) in the solution. The first order difference operator (a bidiagonal matrix) was used for $\mathbf{L_p}$ to limit the oscillations in **b** [89].

$$\mathbf{L_p} = \begin{pmatrix} -1 & 1 & & \\ & -1 & 1 & \\ & & \ddots & \ddots \\ & & & -1 \quad 1 \end{pmatrix} \quad \text{Equation 2.40}$$

The constraint term, $\mathbf{L_p b}$, calculated the gradient in **b**, a measure of the amount of oscillations present in the **b**. Minimizing this penalty term with a residual norm helped to achieve a regularized solution for **b**.

However, $\mathbf{L_p}$ was found to be inappropriate to regularize a dispersed *R(t)*. Since a dispersed *R(t)* starts from zero reaching a peak followed by a decay; the initial part of this residue function was considered as "unwanted" oscillation by $\mathbf{L_p}$, and the regularization tended to oversmooth this part of the curve, distorting the true shape. Therefore, another penalty matrix was used for the residue function with dispersion. The penalty matrix for dispersed *R(t)* was similar to $\mathbf{L_p}$ except the first two points in the residue function were not used for calculating the gradient in **b**, thus only the oscillations in **b** after the first two points were regularized during the minimization process.

Tikhonov regularization showed no significant improvement in estimation of CBF compared to sSVD but estimated a much smoother solution for the residue function. However a complete monotonicity in the residue function was still not achieved. The method performed better in residue function shape estimation in the presence of dispersion, however using a different penalty matrix for the dispersed residue function required a prerequisite model selection.

2.5.7 Maximum Likelihood Method

A Maximum Likelihood estimation of cerebral perfusion was recommended by Vonken et al. [19] using an expectation maximization algorithm. This model was designed to estimate the amplitude of the tissue response function at every measured time point. The method considered the CTC to be the measured response of the AIF interaction with a smooth kernel for the tissue response function (υ). The kernel, υ, was conditioned with a positivity constraint to model a physiological tissue response function. The CTC, measured in the form of T2* relaxivity, was assumed to be governed by a probability density function f(*C(t)*, υ), describing the likelihood that CTC could be mapped, given υ, AIF and the noise model. The maximum likelihood method estimated the corresponding tissue response function by an iterative algorithm achieving maximization of the probability density function with respect to υ.

The method was found to demonstrate some improvements over sSVD including an automatic correction of delay in the AIF and a lower bias for *SNR* in CBF estimation. The assumption of Gaussian noise in the likelihood estimation means that the approach is identical to a least squares solution, which means that it would tend towards the SVD solution. The positivity constraint on the υ curve did not guarantee an oscillation-free estimation of the TRF. The results offered some improvement in CBF estimates at the expense of extra computational effort. However, the method

was tested only on monotonically decreasing exponential and linear residue functions and did not correct for the effects of bolus dispersion on CBF estimation.

2.5.8 Gaussian Process Deconvolution

Gaussian processes for regression have been used for a number of years in geostatistics [91] but the statistical framework for other applications was developed only in 1996 [92] following which the Gaussian process for deconvolution (GPD) problem was suggested by Andersen et al. [20] in 2002 for use in DSC-MRI perfusion analysis. Using the GPD method the tissue residue function was estimated as the mean of an optimized joint Gaussian distribution. The method extended the smoothness constraint in the residue function by incorporating a *priori* information. The method was designed to improve the residue function shape estimation which in turn was expected to improve the perfusion estimation.

The GPD method assumed the tissue response function to be a smooth kernel (*ℌ(t)*) of the convolution operation where the maximum of the kernel was the perfusion:

$$C\,(t) = \frac{\rho}{k_H} \cdot \left(Ca\,(t) \otimes \mathfrak{h}\,(t)\right) \qquad \text{Equation 2.41}$$

$$\mathfrak{h}\,(t) = CBF \cdot R\,(t) \qquad \text{Equation 2.42}$$

The GPD also assumed that each measured value of the kernel is distributed normally around the true value and since there is some correlation between the points on the curve, the data belonged to one joint Gaussian distribution [20]. When the underlying kernel was expected to be smooth, GPD provided a predictive distribution for any point in time over the *ℌ(t)* using measured data for *C(t)* and *Ca(t)* [20].

As noise in the MR signal was considered to be Gaussian and the level of noise was small compared to signal, the measured kernel ($ɦ_{data}$) was thus calculated from the concentration time curve by minimizing the squared error such that [20]:

$$ɦ_{data} = (Ca \cdot Ca^T)^{-1} \cdot Ca^T \cdot C(t) \quad \text{Equation 2.43}$$

Since this is an ill-posed inverse problem, inversion of *Ca* might cause significant oscillations in $ɦ_{data}$. Observed $ɦ_{data}$ belongs to a joint normal distribution such that:

$$ɦ_{data} \in \mathcal{N}(ɦ, A) \quad \text{Equation 2.44}$$

where $ɦ$ is the vector of means of the joint normal distribution and *A* the covariance matrix describing the correlation between points on the kernel. Nothing was assumed about the values of priors on ɦ; however nearby points on ɦ were expected to be correlated to enforce smoothness. As the distances between the sampling points increased the covariance of the points decreased; thus the nearby points had a larger influence on the shape of the curve to maintain the smoothness [20]. Decrease in covariance as a function of temporal spacing was thus further controlled by two additional hyperparameters [92,93]. Thus, the GPD attempted to estimate a joint probability distribution for ɦ by optimizing these hyperparameters and the standard deviation of noise in the system.

The results of residue function analysis using GPD were very promising compared to SVD methods in simulation studies as GPD could now provide a smooth residue function shape. The perfusion values and residue function shape could be calculated with an associated uncertainty around it for each voxel which was not the case with the SVD method. The mean of the GPD perfusion estimates were, however, not very different compared to SVD; GPD underestimated the higher flow values similarly to SVD and the performance of GPD dropped with higher level of simulated noise. The effect of bolus arrival delay, which is a very significant problem in perfusion analysis, was not

evaluated in the study. Bolus dispersion was also not accommodated in the method. Finally the computational time for perfusion analysis was extremely high for practical usage in clinical routine.

2.5.9 Nonlinear Stochastic Regularization

To improve the accuracy of CBF estimation and to characterize the residue function without oscillations, as observed with SVD, an approach based on stochastic modeling has also been proposed called Nonlinear Stochastic Regularization (NSR) [24]. This method relies on the nonlinear Bayesian deconvolution method developed in [94] and consists of formulating a filtered version of a log-normal prior for *R(t)* such that negative realizations for *R(t)* are not possible. In NSR the tissue residue function was described by the convolution of the exponential of a Brownian motion, *β(t)*, with a deterministic exponential function, *d(t)*:

$$R\,(t) = d(t) \otimes exp^{R_1(t)} \qquad \text{Equation 2.45}$$

where:

$$d\,(t) = \frac{1}{\theta} exp^{-\frac{t}{\theta}} \qquad \text{Equation 2.46}$$

$$R_1(t) = \lambda_1 + \lambda_2\,\beta(t) \qquad \text{Equation 2.47}$$

with *β(t)* being Brownian motion, and λ_1, λ_2 and θ unknown model parameters. A Brownian motion function was used to characterize a smoothness constraint over the calculated shape of the residue function. The exponential transformation of $R_1(t)$ guaranteed the non-negative behaviour of the estimated residue function. In this formulation, the model was able to accommodate dispersion in the residue function via the deterministic component, which is an exponential dispersion kernel as in Equation 2.23. Inclusion of the dispersion kernel thus allowed the undispersed solution (residue function) to be reproduced afterwards. It was thus claimed that this method could handle many classes of non-negative signals for perfusion analysis [24].

NSR was shown to characterize the smooth residue function both in the presence and the absence of bolus dispersion during the simulations [24,95]. It also showed improvements in CBF and MTT estimates along with parameterizing the bolus dispersion in the parameter θ [24,95]. However, the main drawback of the methodology was a lack of consideration of the bolus arrival delay which might introduce bias in the solution if the macrovascular transit times are long, thus leading to an underestimation of CBF.

In summary of the perfusion analysis methods, model-free deconvolution is commonly used for DSC-MRI analysis compared to model-based approaches. oSVD is bolus arrival delay insensitive and a robust methodology, thus is widely used in research and clinical settings. Other regularization techniques are also available in the form of sSVD and tkSVD but an accurate estimation of CBF at low MTT and an oscillation free residue function cannot be achieved with any SVD based methods. The non-physiological oscillatory nature of the residue function obtained with SVD provides an opportunity to explore other deconvolution methods where the residue function can be modeled as a monotonic function. GPD, VM and NSR provide a smooth residue function with more accurate CBF estimation. The monotonic behaviour of the residue function might be useful for residue function analysis in pathophysiological variation. However it still needs to tested if these methods are sensitive to these hemodynamic variations *in vivo*.

2.6 Discussion

Bolus tracking MRI plays a vital role in the diagnosis, assessment and management of cerebral ischemia and acute stroke. DSC-MRI analysis is an ill-posed inverse problem requiring deconvolution of the measured CTC with the measured AIF. Several approaches have been used in the past to perform the deconvolution reliably, ranging from model-based deconvolution to non-parametric and model-free deconvolution. Model-based deconvolution [15,21,66], assuming a

predefined functional form to characterize the residue function, is not generally accepted, as it could result in large systematic errors where the actual underlying function is different from that proposed, as might be the case in pathology.

Model-free deconvolution is more appropriate in this case, however being an ill-posed inverse problem a complete deconvolution of CTC with respect to AIF gives rise to amplification of high-frequency noise. Thus, model-free deconvolution is mostly performed with a low pass filter or with a regularization procedure to damp this high frequency noise in the signal. Fourier transform deconvolution [16,25] provides the benefit of being model-free in its approach but using a low pass filter substantially underestimates the CBF. The algebraic method, sSVD with regularization, introduced by Ostergaard et al. [17], is also a model-free approach where the level of oscillation in the solution depends on the threshold (*Psvd*) used for the singular values. The study by Liu et al. [88] suggested that selection of the threshold should be optimized for each *SNR* but Andersen et al. [20] found that the empirical relationship between the threshold value and the *SNR* is more complex than expected by Liu et al. and is influenced by many other factors. Also the proposed adaptive threshold by Liu et al. was only optimized for exponential residue functions [88] with no consideration to hemodynamic variations in shape of the residue function. The accuracy in CBF estimation was found to be highly dependent on the level of threshold used with the SVD procedure, Murase et al. showing discrepancies in appropriate threshold selection for multiple residue functions with and without the effects of bolus arrival delay and dispersion in AIF [96].

A similar problem is also expected with the oSVD approach by Wu et al. [18] where the empirical regularization parameter, Oscillatory Index, is shown to be dependent on SNR values of the perfusion signal. Threshold selection plays a very crucial role in any regularization technique: a low

value leads to a more accurate estimate of CBF but extremely noisy *R(t)*, while a high value provides smoother *R(t)* but underestimation of CBF, more at high flows.

In addition to threshold selection for the SVD method, bolus arrival delay is a source of significant error in CBF estimation if not corrected in the deconvolution routine. When using SVD based methods, a poor estimation in delay reduces the accuracy of CBF estimation by as much as 50-70% [30,97,98]. oSVD is, in theory, a delay insensitive technique, but it has its own limitations with respect to characterization of the residue function shape. Dispersion in AIF is also reflected in the shape of the residue function obtained from SVD and introduces error in CBF estimation.

Dispersion correction in perfusion analysis is difficult as it is hard to separate the effects of microvascular hemodynamics variation from the macrovascular hemodynamics due to strong association of the relevant parameters. In theory, a voxel specific AIF could be estimated by convolving the AIF with a VTF [22,76] but VTF itself is a presumed analytical expression. The shape of the selected VTF depends on a global vascular architecture and might not be adequate in pathological conditions. An alternative to dispersion correction is the use of methods that derive local AIFs [77,99–106], these would bypass the errors introduced using analytical dispersion kernels. However, they suffer from issues due to partial volume effects [79,80] and these are difficult to reduce. Additionally, it still remains to be shown whether these methods can reliably measure the local AIF.

Blood perfusion is a dynamic process; a single acquisition represents an instantaneous flow value which might not be a sensitive predictor of tissue under hemodynamic stress. There are situations where the shape of the transit time distribution and the actual shape of *R(t)* is of interest: in calculating flow heterogeneity and tissue oxygen delivery [8–10], the SVD methods may no longer be suitable and a method which has the least oscillation in *R(t)* is recommended. The oscillations in

R(t) may be reduced by regularization or by adding a penalty term in the optimization. The dependency on the regularization threshold in achieving a smooth residue function has already been shown [96], also its impact on the accuracy of CBF estimation. One additional limitation of regularization techniques is the use of two different regularizing routines, based on the presence or absence of the bolus dispersion, as suggested when using Tikhonov regularization [22]. This is not ideal because it would require the pre-assessment of the presence or absence of dispersion to enable an appropriate model selection which is not possible in practice with clinical data. The monotonicity of the residue function shape is never guaranteed with SVD methods [17,18,22,88].

To improve accuracy in CBF estimation and to achieve a smooth residue function shape, other methodologies have also been proposed but each faces its own limitations. The nonlinear stochastic regularization model has been proposed [24,95], parameterizing *R(t)* as the convolution of a deterministic and a stochastic function. The approach has yet to be validated in clinical settings but NSR performed badly even in simulations of pathological MTT and a non-exponential residue function. The other key limitation was the lack of compensation of the bolus arrival delay. The effects of bolus delay were partially incorporated in the methodology by accommodating dispersion, as both delay and dispersion have similar implications on tissue signal (both cause the signal to shift temporally). However, this factor completely ignores the fact that bolus arrival delay is the delay in the leading edge of the signal and it does not affect the shape of the signal; whereas dispersion can affect both at the same time. The correction of bolus arrival delay in NSR was later implemented in [107] but still a simultaneous correction for delay and estimating dispersion in a nonlinear formulation can give misleading results (as will be discussed in Chapter 4).

A key limitation in the VM model was the parameterization of the transit time distribution with a gamma probability density function. Even though it encompasses a wide range of residue function

shapes it still uses an analytical expression to estimate shapes. Thus assuming a parametric form of residue function, only the flow, delay and shape parameter can be estimated, whereas in the non-parametric approach every point on the residue function must be estimated. The dispersion effect was also not accommodated in the VM. As the residue function was analytically represented and only three parameters were estimated, the dispersion effect can only be reflected as changes in the residue function shape by alterations in the shape parameter (λ) and scaling in the estimated CBF. The influence of dispersion in AIF on final estimation of CBF by VM is thus still unclear.

The VM, GPD, NSR showed an improvement over SVD in estimation of CBF by estimating a smooth monotonic residue function behaviour. It was anticipated that these residue functions might show potential to analyze tissue hemodynamics *in vivo*. The residue functions from *in vivo* data were however not reported in any of these studies which would have shown the potential to interpret this new information for pathophysiological significance. Thus the sensitivity of these methods to show variations in residue function for clinical interpretation remains questionable.

Variations in the shape of *R(t)* and transit time distribution have been proposed as a good marker for flow heterogeneity and tissue hemodynamics [8–10,108]. It has been shown in rat models that variations in flow heterogeneity might show changes in normal and tissue under hemodynamic stress [11,12]. Ostergaard et al. proposed that capillary transit time heterogeneity (*CTTH*), measuring the standard deviation of the transit time distribution, could be a potential indicator for assessing cerebral hemodynamics beyond CBF [9]. However, because of the oscillatory nature of *R(t)* observed with standard SVD methods it is highly challenging to interpret the variations in the shape of the residue function for clinical use. The VM guarantees a physiologically smooth residue function but it still remains to be tested if its assumptions of a gamma probability distribution function to model the underlying hemodynamics could offer sufficient versatility to capture

pathological variations. Therefore a non-parametric deconvolution methodology that could offer the flexibility of a SVD method whilst keeping the residue function regularized for physiological quantification of capillary hemodynamics beyond CBF would be highly desirable.

Thus none of the currently available deconvolution techniques can offer a solution to quantify cerebral hemodynamics from *in vivo* perfusion imaging. Variations in tissue hemodynamics are expected under pathology, i.e. ischemia and infarction, but none of the deconvolution methods have been shown to be sensitive to these variations. A novel deconvolution method that could provide a physiologically smooth residue function could also serve as a means to quantify these subtle variations in capillary hemodynamics. A method to quantify transit time variations in pathology could aid intervention at a much early stage of cerebral ischemia that could lead to earlier diagnosis and timely initiation of treatment.

2.7 Conclusion

Magnetic resonance perfusion imaging with contrast is the imaging modality of choice for assessment of cerebral ischemia in clinical settings. SVD based deconvolution methods are commonly used in quantification of cerebral perfusion with MRI. In addition to perfusion quantification, estimation of capillary hemodynamics is also of wide research interest. SVD based methods, however result in the non-physiological oscillations in the calculated residue function. Quantification of cerebral hemodynamics for pathophysiological variations has been attempted in the past by reducing the non-physiological oscillations in the residue function through various regularization approaches to the most commonly used SVD based deconvolution method. However, a completely smooth residue function was never achieved with any of the SVD methods, making capillary hemodynamics quantification challenging. Model-based methods such as VM and model-

free methods such as GPD and NSR guarantee a monotonic residue function but no one has demonstrated the sensitivity of these methods to residue function variations *in vivo*.

Given the significant limitations of existing methods, it is highly desirable to have a method that is accurate in perfusion quantification and is able to estimate a positive and smooth residue function (i.e. more physiologically realistic) both in the presence and the absence of delay and dispersion. The residue function can then be used to examine hemodynamic variations in diseases such as cerebral ischemia.

Chapter 3

A Control Point Interpolation method for the Non-Parametric Quantification of Cerebral Hemodynamics from Dynamic Susceptibility Contrast MRI[1]

3.1 Introduction

Dynamic susceptibility contrast magnetic resonance imaging is frequently used in the measurement of cerebral perfusion in stroke and other pathological conditions. It has been shown that perfusion parameters like cerebral blood flow, cerebral blood volume and mean transit time can be used in acute stroke patients for quantification of cerebral ischemia [5,6,27]. The measurement of these perfusion parameters is based on tracer kinetic theory [17,25,62] that considers the tissue concentration time curve as the convolution of the arterial input function with a CBF-scaled tissue residue function. The residue function describes the fraction of tracer remaining in the tissue vasculature at a time after its arrival. One major concern in inferring the crucial perfusion parameters from DSC-MRI is reliable and accurate deconvolution of the observed concentration time curve with respect to the measured AIF.

Initially an analytical model-dependent deconvolution technique was proposed [15] but it has been superseded by more flexible non-parametric approaches like frequency domain deconvolution

[1] This chapter has been published as Mehndiratta, A.; MacIntosh, B.J.; Crane, D.E.; Payne, S.J.; Chappell, M.A; *Neuroimage*. 2013; 64:560-70

(Fourier transform) [16,25] and later by algebraic singular value decomposition (SVD) method [17]. Variants of the SVD approach such as tSVD (truncated SVD) [17] and the time insensitive oSVD (circular-SVD) [18] are widely used to estimate the tissue response function (TRF; defined as residue function multiplied with CBF), its maximum value being used to estimate CBF. The key issues with SVD-based methods are the underestimation of CBF and also the introduction of non-physiological oscillations in the resulting residue function, making the residue function difficult to interpret. There have been attempts with various regularization approaches to reduce the oscillation in the residue function. Some of the widely used regularization methods involve: truncated SVD (threshold using Psvd [17]), oSVD using oscillation index (OI) [18] or adding of a penalty term in the optimization, for example the Tikhonov regularization of Calamante et al. [22]. Despite all these efforts the estimation of realistically smooth residue functions has not yet been achieved with SVD methods.

Mouridsen et.al [23] have proposed a vascular model (VM) implemented within a Bayesian framework as an alternative to SVD methods. The model is based on a vascular architecture where a gamma probability distribution function is assumed to model the underlying tracer transit times. The VM perfusion values are believed to produce more accurate estimates compared to the SVD method, but, being a model-based solution, it lacks the flexibility of SVD methods. In particular, the underlying gamma distribution in the VM is controlled by two parameters that permit only a restricted family of shapes for the tissue response function which might not be appropriate in modeling altered vasculature in pathologies like ischemia and stroke.

The shape of residue function is also of interest because it contains information about tissue vascular integrity [8,9]. For *in vivo* analysis the actual residue function shape is not known *a priori* and, particularly in pathology, might not be drawn from the set of functions currently assumed for

typical residue functions. Hence an analysis approach that is both model-free and non-parametric would be desirable. The goal of this work is therefore to develop a deconvolution algorithm that produces accurate perfusion values by improved estimation of the residue function over a wide range of physiological conditions. A Bayesian Control-Point Interpolation (CP-Interpolation, CPI) deconvolution method is proposed in this chapter that can estimate cerebral perfusion along with a physiologically plausible residue function without requiring it to belong to a specific class of functional shapes. The resulting residue function shapes can be used to assess the residue function variability among different brain regions and changes in the residue function in pathology.

Theoretical concepts of tracer kinetic theory, SVD deconvolution and VM method have already been described in Chapter 2. In this chapter the framework for the CPI method and its estimation procedure will be elaborated followed by the simulation protocol that was used to evaluate the method. Finally, examples are given where the CPI method is applied to analyze data from a healthy participant and a cerebrovascular diseases patient and the results compared with SVD and VM methods.

3.2 Theory of the CPI Method

Like Mouridsen et al. [23] the CPI method proposed here takes a model-based approach to CBF quantification (Figure 3.1). However, the model is structured so that it can provide the flexibility afforded by non-parametric approaches subject to suitable constraints on the smoothness of the residue function. In place of the gamma distribution used in the VM to define the residue function, the CPI method models the residue function using a restricted number (η) of control points that have freedom in both amplitude and time. These control points are further parameters of the model to be determined from the data (Figure 3.2). The control points act as virtual nodes, the full shape of the residue function being generated using piecewise cubic spline interpolation [109]. Constraints

on the control points are implemented in the model such that the resulting residue function would be plausible. Each consecutive control point is related to the precursor by the ratio factor (Ω) and a time spacing (ζ):

$$r_i = r_{i-1} * \Omega_i \qquad \text{Equation 3.1}$$

where r_i is the amplitude of the i^{th} CP and :

$$t_i = t_{i-1} + \zeta_i \qquad \text{Equation 3.2}$$

where t_i is the time point of the i^{th} CP.

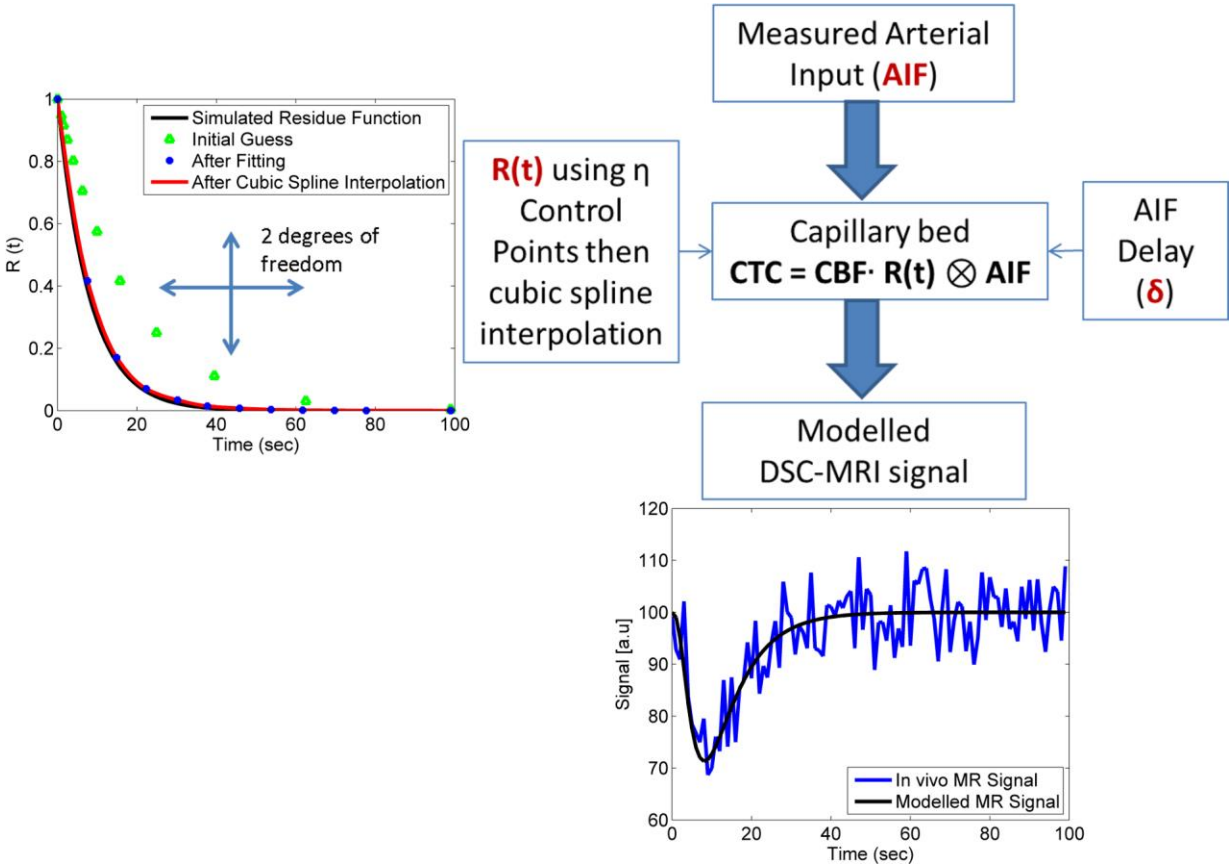

Figure 3.1: The non-linear single-input single-output system for the CPI. The tissue residue function is estimated by setting control points (η) that form the basis of a smooth piecewise cubic spline interpolation along with the parameters CBF and δ. Signal fitting optimisation is performed using Bayesian non-linear model fitting algorithm.

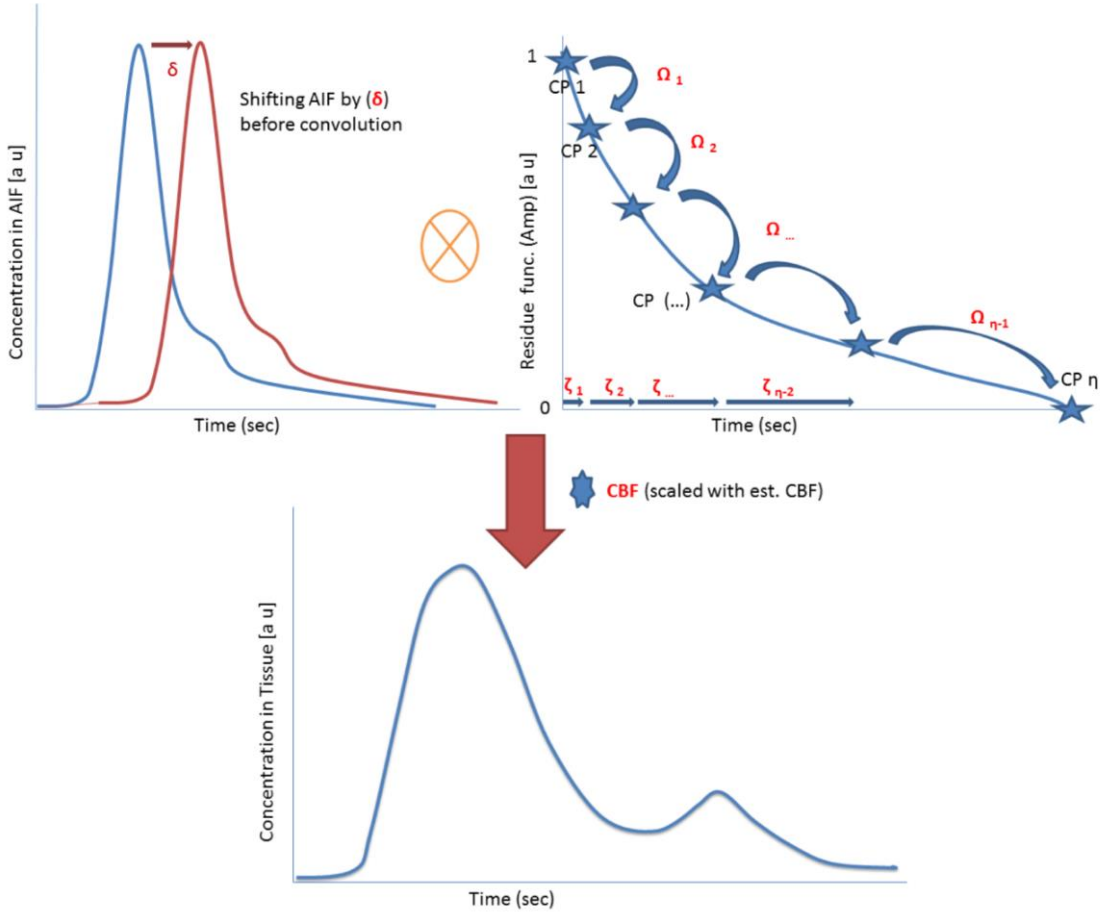

Figure 3.2: Compensating for delay (δ) in AIF and estimating the shape of residue function with η control points (CP), such that CP_1 (t=0, r=1) and CP_η (t=last time point of CTC, r=variable). The convolution is performed between the AIF and the parameterized residue function scaled with estimated CBF to generate a CTC. The parameters are estimated by optimizing the resulting signal (from estimated CTC) with respect to the measured MR signal. The estimating parameters (in red) are Ω, ζ, δ and CBF.

The first control point is fixed so that $t_1 = 0$ with $r_1 = 1$ to meet the fundamental definition of the residue function that $R(0) = 1$. Additionally, t_η is fixed at the last time point of the measured CTC, but with free amplitude calculated from Equation 3.1, to avoid extrapolation errors. To encourage physiologically plausible residue function shapes and numerical convergence of the solution a few other constraints are incorporated in the CPI method such as: CBF cannot be negative ($CBF \geq 0$); the maximum value permitted for Ω was 1.5 ($\Omega \leq 1.5$) and a maximum of three control points could be put within a *TR* ($\zeta \geq TR/3$). Thus the total number of estimating parameters in the CPI method is

2η-1 (from parameters CBF (1), δ (1), Ω (η-1) and ζ (η-2)). The CTC estimate is found using Equation 2.9 and converted to the signal estimate using Equation 2.7. The measured signal (*S(t)*) is considered both with a deterministic (*s(t)*) and a Gaussian noise component (*ε(t)*), $S(t) = s(t) + \varepsilon(t)$. The estimated parameters are then optimized iteratively by maximizing the posterior probability of the predicted signal from the method with respect to the measured MR signal using a Bayesian non-linear model fitting algorithm [110].

3.3 Methods

3.3.1 Model Implementation

The implementations of oSVD, VM and CPI method were all performed using MATLAB with in-house algorithms. The oSVD method was implemented as in [18]. The VM was implemented with priors supplied from the oSVD solution as described in [23], model-fitting was performed using the Bayesian non-linear model fitting algorithm of [110], which is broadly similar to that used by [23]. The CPI method was also implemented using the same Bayesian non-linear model fitting algorithm [110]. A total of 12 (η=12) control points were used; these were initialized according to an exponential residue function shape with a logarithmic temporal spacing to encourage more control points at earlier time points where the residue function will have larger amplitudes. The number of control points was chosen based on preliminary simulation studies where it was found that having fewer than 5 control points (η<5) was insufficient to approximate the residue function shape and that being more than 12 control points (η>12) led to an extra computational time (results not shown) with no significant improvement in results. The complete estimated residue function curve was generated from the control points by interpolation using cubic Hermite piecewise splines [109]. The final residue function curve generated with splines was used in convolution with the measured AIF to form a predicted CTC after scaling with the CBF estimate. The AIF was shifted according to

the bolus delay estimate (δ), such that the AIF shape remained the same but moved temporally by δ units. The CTC was converted into a predicted signal using Equation 2.7. Ω, ζ were estimated on a logarithmic scale, since this makes the model more linear with respect to these parameters, aiding the convergence of the fitting algorithm, which depends upon a local linear approximation to the function using a Taylor expansion [110]. Hence the estimated parameters (Figure 3.2) in the CPI method were $\boldsymbol{\Theta}$ (log (Ω), log (ζ), δ, CBF).

Prior Distribution

Prior knowledge was incorporated in the form of a Gaussian distribution for each parameter with mean and standard deviation values given in Table 3.1. A non-informative prior was implemented for CBF using a large standard deviation and zero mean, whereas δ had a reasonably informed prior. For Ω and ζ the priors were chosen so as to promote a smooth residue function whilst retaining the flexibility of the residue function shape to adapt to the data.

Table 3.1: Priors for the CP-interpolation method.

Parameter	Mean (μ)	Variance (σ^2)
CBF (a.u)	0	10^6
Delay (δ) (sec)	0	10
Log (Ω)	Log (0.5)= -0.69	0.67
Log (ζ)	Log (8) = 2.08	0.40

The method was initialized with CBF and δ values from the oSVD since these may provide a reasonable first estimate in the vicinity of the true solution.

3.3.2 Simulations

An AIF was simulated using a gamma-variate function (Equation 2.16) which has been described previously with typical constant values as: a=1, b=3, c=1.5 [17,18,23,29,81]. Simulations were

performed with CBV= 4% (4 ml/100g) and 2% (2 ml/100g) which are representative of normal grey and white matter [84] respectively. CBF values were varied from 10 to 70 ml/100g/min in increments of 10 ml/100g/min for CBV=4% and from 5 to 35 ml/100g/min in increments of 5 ml/100g/min for CBV=2%. Thus MTT varied in the range 3.43s to 24s. The actual tissue response function is usually not known *a priori* and in the literature fairly simple residue functional shapes have been assumed. In accordance with the literature [17] three different types of residue functions were simulated: Exponential (Equation 2.17), Linear (Equation 2.18) and Box-car function (Equation 2.19). The exponential residue function describes a well-mixed compartment model whereas the box-car function describes a vascular bed with "plug" flow where the capillaries are in parallel with equal length and mean transit times.

Concentration time curves were generated as described in Equation 2.9. A linear relationship was assumed between tissue relaxivity (R_2*) and *C(t)* [56]. The measured MR Signal to CTC conversion and vice versa were performed using standard equation (Equation 2.7) that has been used for similar studies [6,17,18,23]. The CTC was converted to signal curves *S(t)* as in Equation 2.7 with *S(t0)*=100 and *TR*/*TE*=1s/65ms. The constant *k* was chosen such that 40% peak signal drop was achieved at a flow of 60 ml/100g/min with CBV=4% [18]. The AIF signal curve was generated similarly but a value of proportionality constant *k* was chosen such that 60% peak signal drop was achieved. Zero mean Gaussian noise was added to the signal curves (Equation 2.26) to produce a baseline SNR of 20 and 100 simulating typical DSC- MRI and the best possible image data acquired respectively. Values of +5sec, 0sec and -5sec were used to evaluate the model for sensitivity with respect to bolus arrival delay (δ). For each combination of CBV, CBF, residue function and delay a total of 100 CTC were generated. Thus a total of 12,600 (2 x 7 x 3 x 3 x 100) concentration curves were analyzed during each simulation process with three methods: oSVD [18], VM [23]and CPI method.

3.3.3 In-vivo Clinical Data

For clinical evaluation of the methods *in vivo* data was retrospectively analyzed from one healthy participant and one patient with a history of atherosclerotic disease (data was provided by Dr. Bradley J. MacIntosh, and AIFs by David E. Crane, University of Toronto, Canada). Images were acquired under Institutional Review Board (IRB) approved protocol for DSC-MRI study. The MRI acquisition was performed on Siemens 3T Trio, GRE-DSC:*TR*/*TE*=1.5sec/30msec, 78 volumes, 128 x 128 x 22 matrix, 1.7 x 1.7 x 5 mm^3 voxels. An intra-venous (IV) bolus injection of 0.1 mmol/kg Magnevist® was performed at an injection rate of 10 ml/s followed by a 20 ml saline flush. DSC images were then analyzed with the three methods: oSVD, VM and the CPI method.

The AIF was selected in the *in vivo* clinical data using an automated algorithm as in [111] on a 30mm slab centered at the Circle of Willis. CTC features including the first moment (FM), peak height (Pmax), time to peak (TTP) and bolus arrival time (Td) were extracted and using a K-means clustering algorithm voxels were grouped into five classes (grey matter, white matter, vessel, CSF and background). The AIF was defined in the vessel subclass with highest Pmax and lowest FM and a venous output function (VOF) in the same class but with highest Pmax and greatest FM. The AIF was then scaled such that the mean value after the first passage of bolus (the tail of AIF) was equal to the tail of the VOF using the tail scaling technique [26].

3.3.4 Statistical Analysis

A regression coefficient (ϒ) was calculated for estimated vs. absolute simulated flow values and used to compare the different analysis methods. Coefficients of determination (R^2) were calculated using the sum of squared error method and employed to evaluate the signal fit achieved from each of the methods as well the fit of the estimated residue function against those simulated. R^2 varies in

range from 0 to 1, where zero means a poor estimation and values close to one represent a good agreement between simulated and estimated shape.

3.4 Results

3.4.1 Simulations

Figure 3.3 shows the mean estimated CBF (10-70ml/100g/min) for all three methods (SNR=20 and CBV=4%), regression coefficients being given in Table 3.2. Lower CBF values were estimated accurately by all the three methods. CPI method showed more accurate CBF estimates at high flow rate with the exponential residue function. With linear residue function oSVD and VM were found to underestimate perfusion but CPI overestimated the higher perfusion values. All three of the methods showed an overestimation in CBF for the box residue function, CPI being the highest. The regression coefficient of the CPI was most dependent on the shape of the residue function (see Table 3.2). The mean percentage error in estimation of CBF and absolute error in bolus arrival delay is shown in Figure 3.4 for δ= 0sec and ±5sec. The CPI method exhibited the smallest absolute error in estimated CBF (7.5-11%) in comparison to other methods (oSVD: 20-21.5%; VM: 14-17%) across the range of delays simulated (Figure 3.4 a). The error in CBF estimation with CPI was slightly higher (11%) for negative delay against 7.5% for positive or no delay. The CPI method and VM were able to estimate the actual delay values with greater accuracy than oSVD (Figure 3.4 b).

Table 3.2: Regression coefficient (Υ) for estimated vs. absolute simulated flow values. SNR= 20

	CBV = 4 %			**CBV = 2 %**		
Method	Exp. Func.	Linear Func.	Box Func.	Exp. Func.	Linear Func.	Box Func.
oSVD	0.71	0.84	1.05	0.70	0.82	0.98
VM	0.83	0.87	1.21	0.82	0.98	1.25
CPI	0.96	1.17	1.55	0.94	1.15	1.43

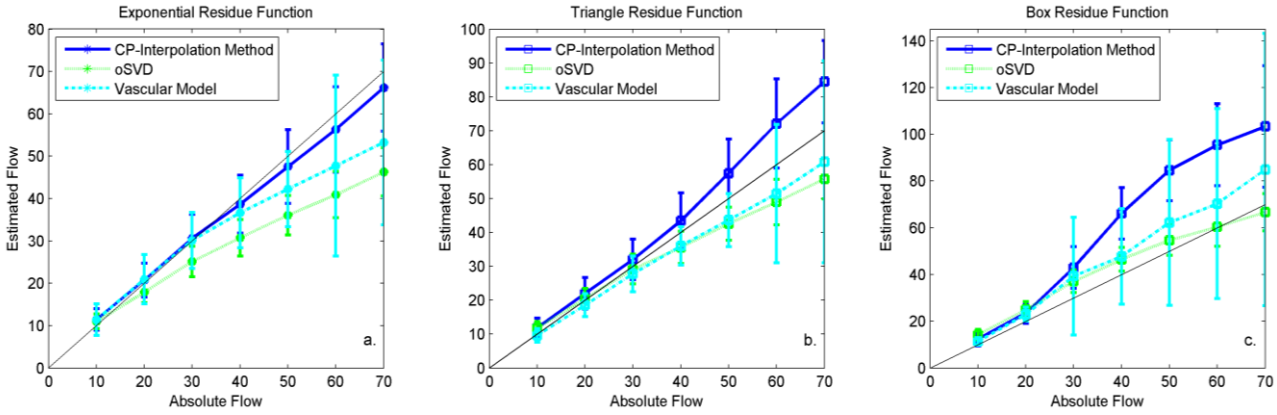

Figure 3.3: Simulation results showing the estimated CBF plotted against the true CBF values (SNR=20 and CBV 4%; note the different scale of estimated CBF in a, b and c).

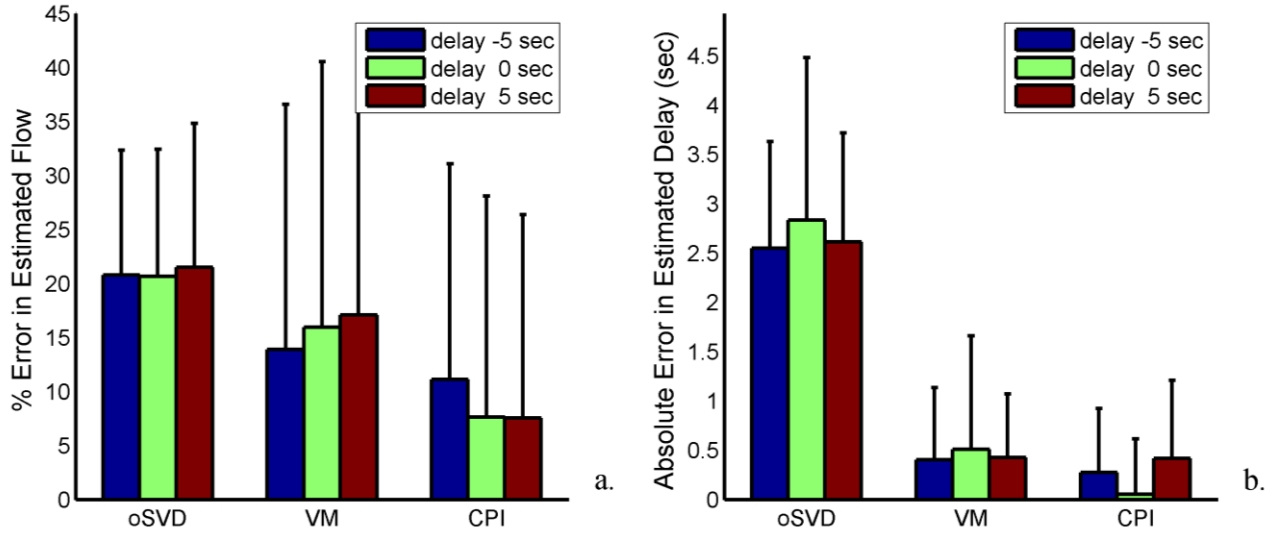

Figure 3.4: Mean percentage error in estimation of CBF (a) and absolute error in bolus arrival delay (b) for the three methods with respect to simulated delay values of 0 sec and ±5 sec with CBF=10-70ml/100gm/min, CBV 4% and SNR=20.

Figure 3.5 (a,b,c) illustrates the results from one of the simulated datasets comparing the TRF shape estimation for a typical grey matter with CBF of 60 ml/100g/min. The CPI method was generally found to be able to estimate a residue function shape in keeping with the original without the oscillations seen in the oSVD solution. The vascular model was found to fit the linear residue

function with a squarish shaped function and the CPI method approximated the box shape with a linear shape function at high flow values (60 ml/100g/min). CPI performed better in approximating the box residue function shape at lower CBF values (Figure 3.6) that would be consistent with cerebral ischemia (CBF=10 ml/100g/min). Figure 3.5 (d,e,f) shows the mean and standard deviation (σ) over the 100 datasets of the estimated residue function from CPI method for data generated with exponential, linear and box residue functions at CBF=60 ml/100g/min, CBV=4% and SNR=20. The mean estimate of the shape of residue function was found to closely resemble that simulated with a narrow variability across the 100 separate instances for exponential and linear residue function. The residue function fitting was found to be improved and variation in fit was reduced at high SNR and high MTT values (Figure 3.6 (d,e,f) with CBF=10 ml/100g/min simulating ischemic tissue).

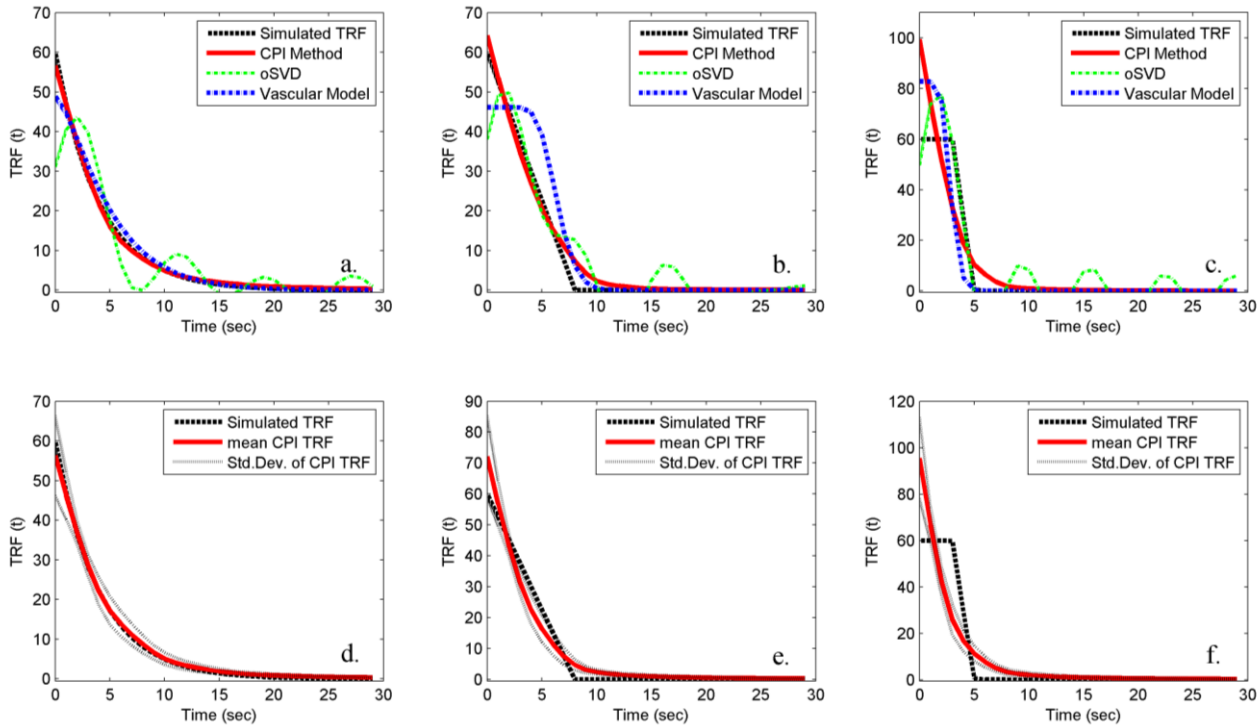

Figure 3.5: Typical residue function obtained with oSVD, VM and CP-interpolation method simulating normal grey matter (CBF=60ml/100g/min, CBV=4%, δ=0, SNR=20) for a) Exponential, b) Linear and c) Box residue function. The oSVD estimate exhibits large oscillations whereas CP-interpolation and VM yield smooth solutions. d), e) and f) illustrate the mean shape estimated for the corresponding simulated residue functions with ± σ bands for CP-interpolation method.

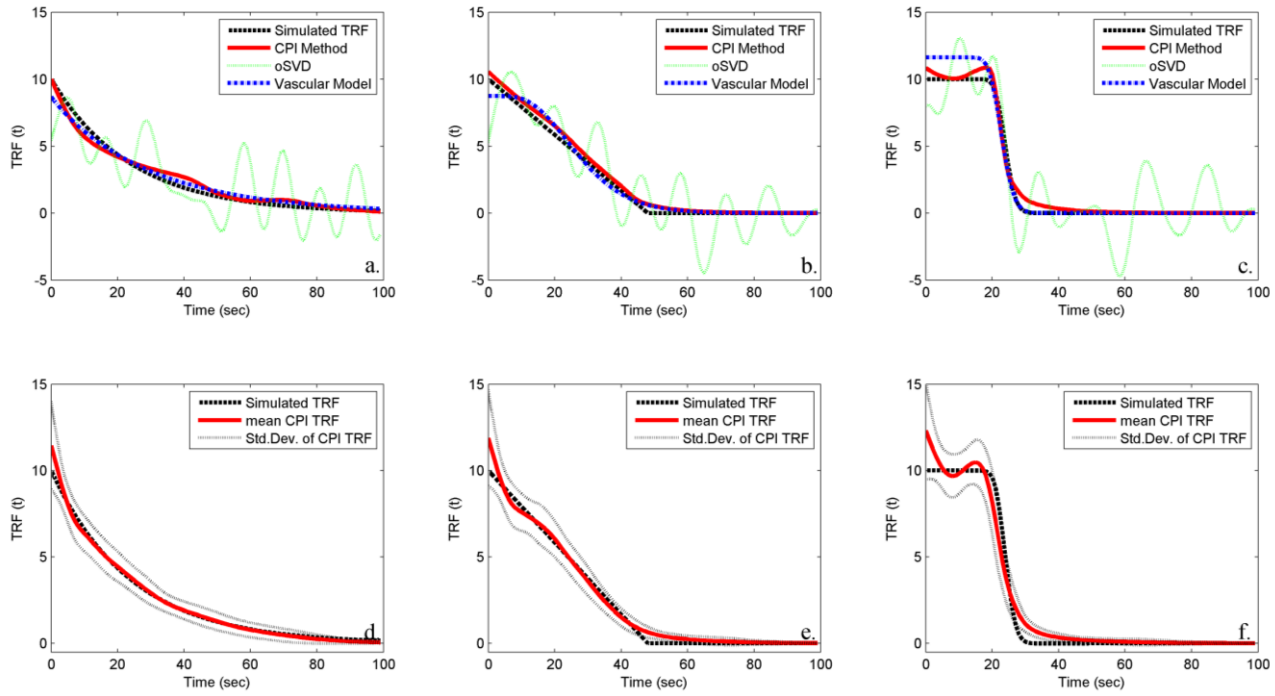

Figure 3.6: Typical residue function obtained with oSVD, VM and CP-interpolation method simulating cerebral ischemia (CBF=10ml/100g/min, CBV=4%, δ=0, SNR=20) for a) Exponential, b) Linear and c) Box residue function. Large oscillations were seen with oSVD; CPI and VM both were found to produce smooth solutions. d), e) and f) illustrate the mean shape estimated for the corresponding simulated residue functions with ± σ bands for CPI method.

Table 3.3: Coefficient of determination (R^2) for estimated residue function against the simulated residue function (mean ± σ(R^2))

Method	R^2 (Exp. Func.)	R^2 (Linear Func.)	R^2 (Box Func.)
oSVD	0.62 ± 0.13	0.70 ± 0.11	0.75 ± 0.09
VM	0.93 ± 0.13	0.92 ± 0.14	0.82 ± 0.51
CPI	0.96 ± 0.03	0.95 ± 0.04	0.82 ± 0.10

All methods exhibited a good correlation as measured by the coefficient of determination (R^2) for the fitted signal against the true simulated signal, the CPI method having the best correlation (0.98±0.02) followed by VM (0.97±0.03) and then oSVD (0.93±0.02). Table 3.3 illustrates the corresponding coefficients of determination between the estimated residue function shapes and the simulated residue functions. The VM and CPI had a higher value of R^2 than the oSVD method but

the VM showed considerable variation as reflected by its larger value of standard deviation ($\sigma(R^2)$) for exponential, linear and box residue functions compared to the CPI method.

3.4.2 In vivo Data

Figure 3.7 shows representative perfusion maps for a healthy participant estimated by the three methods along with residue function from two ROIs (region of interest of 3x3 voxels). The oSVD estimates of CBF were the lowest of the three methods. CBF values estimated from both the VM and CPI method were substantially higher than those from oSVD; unlike the simulation studies VM consistently estimated the highest CBF within any given voxel. The CBF maps showed a good grey/white matter contrast and a larger dynamic range for CBF estimates with both CPI and VM methods. MTT estimates from the oSVD method were observed to be higher than other two methods, but a larger variation in MTT was observed with VM and CPI methods. All the methods showed a higher MTT in the ventricles as expected in the case of normal intact blood brain barrier. The residue function shapes estimated by CPI method were found to be smooth as anticipated, whereas the oSVD showed oscillatory variations.

The data from a patient with atherosclerotic disease are shown in Figure 3.8, where it was found that VM CBF estimates were the highest of the three methods. The oSVD and CPI methods showed higher values of MTT in a small region of the left parietal lobe; the diffusion weighted image (DWI) confirmed the presence of infarcted tissue within this lobe. Two ROIs were selected (3x3 voxels), one in the region of infarcted tissue and other in a nearby normal appearing brain parenchyma. The CPI method demonstrated substantial change in the residue function shape between the two ROIs whereas no appreciable change in shape was observed with VM solutions. With CPI method the residue function from infarcted tissue ROI (Figure 3.8 l) appeared to have a slower decay in consistent with high MTT observed in the region (Figure 3.8 f).

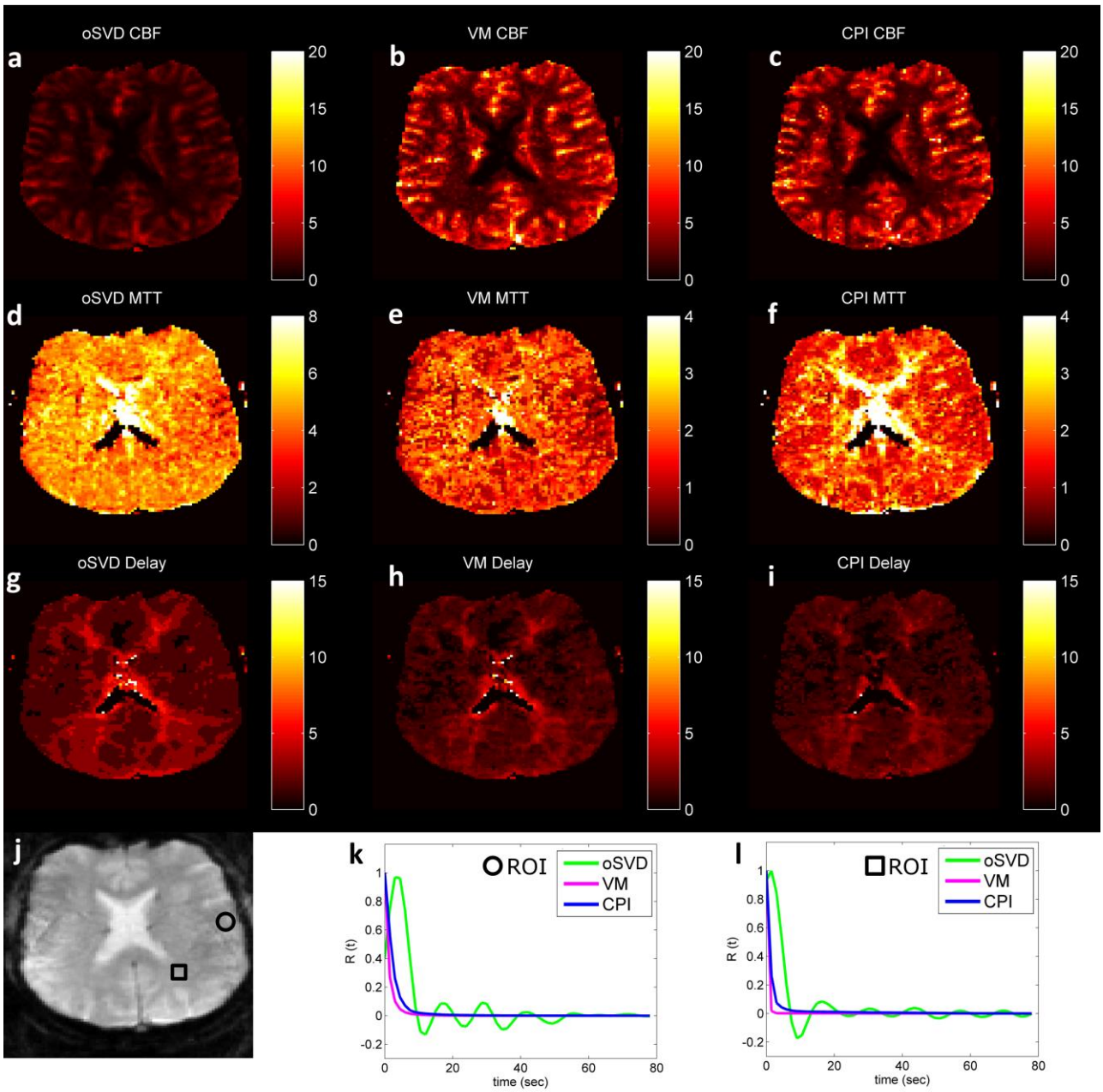

Figure 3.7: Axial brain slices showing perfusion maps estimated by oSVD (a,d,g), VM (b,e,h) and CPI (c,f,i) method for a healthy participant. CBF estimates by VM (b) were highest among the three methods (a,b,c). MTT values obtained from oSVD (d) were substantially higher thus are shown in a different scale. Delay maps (g,h,i) demonstrated no differences between the methods. j) shows a T2* grey scale image with two selected ROIs for residue function shape analysis. In estimated shape of residue function (k,l) for two representative ROIs (3x3 voxels), an oscillatory function shape was obtained from oSVD, resulting in a lower CBF estimate compared to the other two methods whereas the residue functions obtained from VM and CPI methods were smooth.

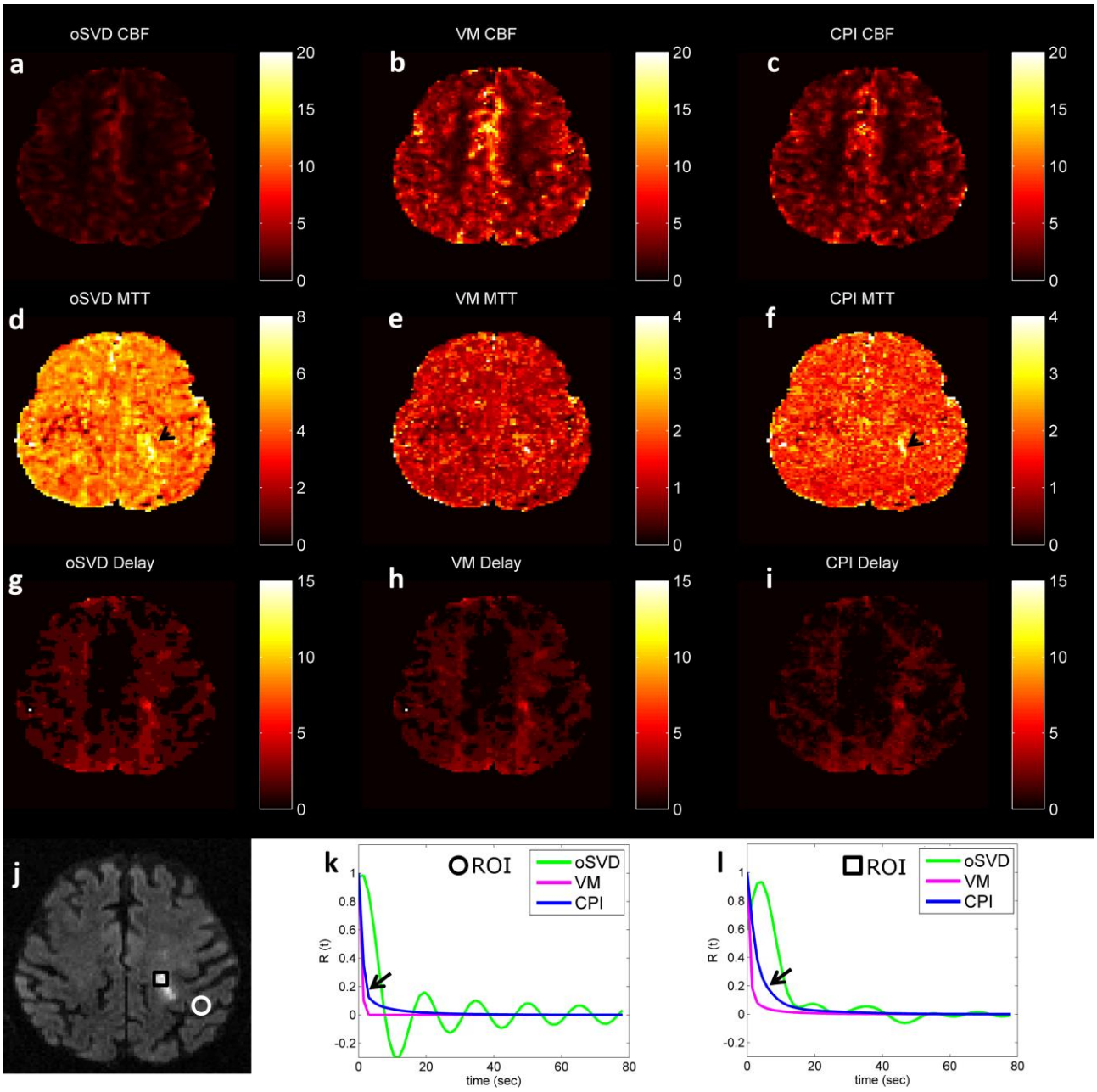

Figure 3.8: Axial slice showing perfusion estimates from oSVD (a,d,g), VM (b,e,h) and CPI (c,f,i) method for a patient with atherosclerotic diseases. CBF estimates from VM (b) were the highest among three methods (a,b,c). The diffusion weighted image of this patient (j) showed an area of infarcted tissue in left parietal lobe. The MTT map from oSVD (d) and CPI (f) showed a higher MTT in the infarcted region (arrow head). The obtained residue function for two ROIs (3x3 voxel) (k,l) demonstrated considerable difference in shapes with CPI method (arrow).

3.5 Discussion

A CPI technique using Bayesian optimization has been developed for the estimation of perfusion-related metrics in DSC MRI. Singular value decomposition and its variants have been used extensively in DSC MRI analysis despite estimating physiologically unrealistic oscillatory residue functions. As an alternative the VM can estimate smooth residue functions and has been shown to offer some improvement in CBF estimation but represents a constrained model-based approach, which introduces bias if the model assumptions were not reasonable such as might be the case in pathological tissue. The principle behind the novel CPI methodology is to improve the estimation of CBF by accurate estimation of the tissue residue function. In the proposed approach, the tissue residue function is estimated at a subset of points and then cubic spline interpolation is used to generate the complete smooth function. The simulation study showed that oSVD and VM both produced an underestimate of CBF at higher flow values while the CPI method is more accurate as shown by the larger values of the regression coefficients for simulated exponential residue functions. The regression coefficient of the CPI was most dependent on the shape of the residue function (Table 3.2). CPI is also more accurate in residue function shape estimation as shown by large value of coefficient of determination in Table 3.3. The vascular model is found to estimate a squarish residue function shape when the true shape is linear, thus resulting in underestimation of CBF. This arises because a linear shape is not possible within the VM equations demonstrating a limitation of the VM in that it can only call upon a limited set of residue function shapes. The CPI method estimated the box shape with a linear shape at high flow values; this is less pronounced at low flow and high MTT values. In practice extreme residue function shapes like the linear and box residue functions are unlikely to be observed, smooth functions like the exponential being the most likely approximation to true physiology.

The residue function shapes as estimated from CPI method in the clinical perfusion data (Figure 3.7 and Figure 3.8) are smooth and revealed that the residue function has both fast and slow components. From simulation studies, the CPI method was expected to have higher CBF estimates than both oSVD and VM method but Figure 3.7 and Figure 3.8 show that the VM estimates of CBF are comparatively higher than both other methods. This may be due to the underlying residue function shape, since VM would not be able to represent the residue function accurately if residue function actually has both fast and slow decay component that is observed from the CPI method. Thus an additional simulation study to investigate this hypothesis was performed. The residue function as obtained from CPI method in normal healthy participant was averaged over a region of interest (4x4 voxels); further simulated data were generated using this function and the similar methodology used above.

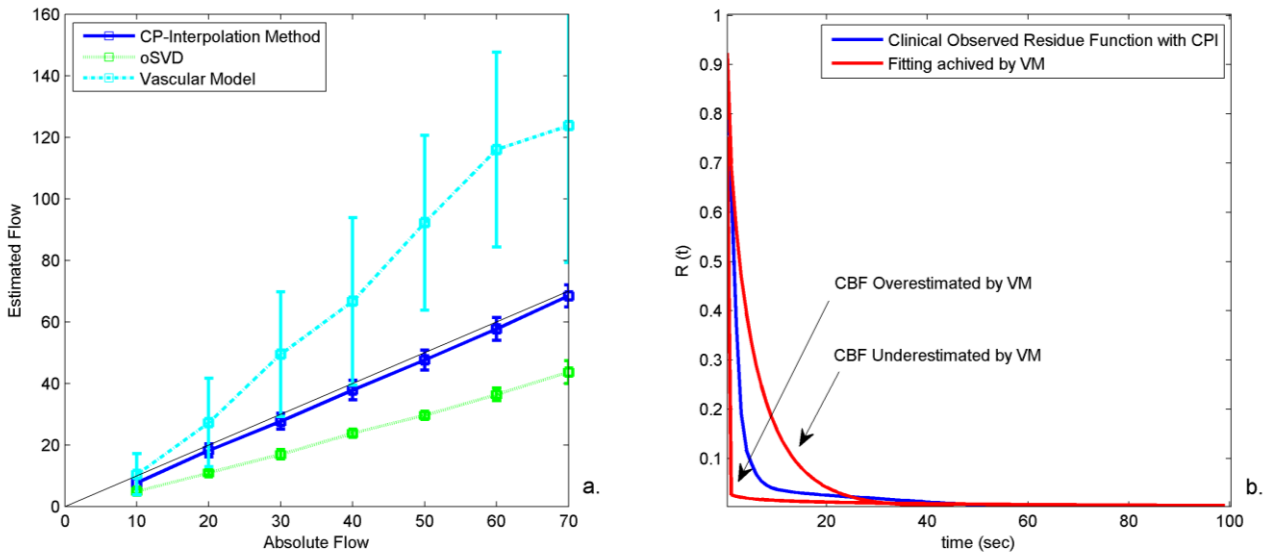

Figure 3.9: a) Absolute simulated CBF against estimated CBF (SNR=100) for simulation study where residue function used to generate MR signal was the residue function observed using the CPI method in the analysis of a healthy participant, b) example estimated residue functions from VM for the occasions where it over and underestimated the CBF.

As might be expected even with this complex shape of residue function the CPI method estimated the CBF values correctly (ϒ (CPI) = 0.96), where oSVD method underestimated (ϒ (oSVD) = 0.60) and VM overestimated (ϒ (VM) = 1.79) the absolute simulated CBF values (Figure 3.9 a). The overestimation of CBF by VM seen in these simulations is consistent with the *in vivo* data thus supporting the hypothesis. There was a wide variation observed in the estimation of the residue function shape by the VM in this additional simulation study. Over all the data sets simulated, on the majority of occasions (more than 90%) the absolute CBF was overestimated by the VM with residue function solution (Figure 3.9 b) being similar to that observed in the *in vivo* data; whereas only in some cases (less than 10%) the absolute CBF was underestimated by the VM with a much slower decaying residue function shape (Figure 3.9 b).

The results from the CPI method suggest that in the *in vivo* data the residue functions deviate from those assumed by the gamma distribution of transit times that form the basis of the VM. This may partially reflect in the presence of contamination from contrast agent in larger arteries. Dispersion of the contrast bolus between the site of measurement of the AIF and the voxel is also a widely documented effect that will be represented by a change in the residue function shape if not accounted for elsewhere in the analysis [29,77,79,112]. One of the strengths of a non-parametric deconvolution method is that it is adaptable to such sources of variation that otherwise would violate the assumptions of a model-based approach such as the VM. The CPI method can be viewed as effectively non-parametric, in that it retains the flexibility in the residue function shape. However, the estimation of the residue function is subject to constraints that regularize the shape avoiding the oscillations that plague SVD solutions. Attempts have previously been made to reduce the oscillation in the estimated residue function through various regularization approaches [17,18,22] but the estimation of realistically smooth residue functions has not yet been achieved

with any of the SVD-based methods. Model-based approaches provide a means by which well-behaved residue functions can be estimated.

The effectiveness of the CPI solution is illustrated in a patient, where changes in the residue function were observable between healthy and infarcted tissue. These changes are subtle and require further validation. However, they suggest that the CPI method might be able to offer residue function estimates that could be interpreted in terms of the underlying physiology. This would include the use of the residue function to probe the heterogeneity of the flow within the tissue [8,9].

Bolus dispersion is common in ischemia and stroke as suggested by [29]. It is an issue even in the healthy brain (probably to a less extent than ischemic tissue) – given that a global AIF is measured remote from the site of perfusion for analysis. Bolus dispersion can mathematically be represented as a convolution of the residue function with a vascular transport function [29,112]. As per the fundamental definition, the residue function is a monotonically decreasing function, $R(0)=1$; but when bolus dispersion in included the residue function no longer starts from one ($R(0)\neq 1$) instead starts from zero, $R_{disp}(0)=0$. In CPI method the first control point is fixed at one ($CP_1=1$) to satisfy the fundamental definition of the residue function. The issue of bolus dispersion will be further investigated and the modifications in the CPI method to accommodate the effects of bolus dispersion will be evaluated in the next chapter.

The CPI method overestimated CBF for linear and box residue function at high flow values, where it was unable to perfectly represent the true residue function shape. Whilst the CPI method has the flexibility to represent these functions, the estimation is performed on the signal curve and not the residue function directly. For high flow values, with consequently short MTT, the effects of different residue function shapes on the signal curve is small, making accurate residue function shape estimation difficult. Where it is difficult to choose between a range of possible shapes the CPI

method will opt for something that is smooth, hence the shapes found in (Figure 3.5). With longer MTT it was able to more accurately estimate these functions and the true residue function shape (Figure 3.6) and CPI would be expected to perform better at high flows with data with shorter TR. A further modification that might improve estimation and avoid the oscillation seen in the box residue function result in (Figure 3.6) would be to limit Ω to values only lower than 1. However, with the optimization algorithm chosen here hard limits can be problematic potentially leading to numerical stability issues when placed quite tightly around expected range of the parameter's values. In the results here oscillations were only observed in a very limited subset of cases often reflecting features of the residue function such as the transition in the box function.

Another limitation of the CPI method is the greater computational cost over SVD or VM methods for the *in vivo* analysis (oSVD ~3 minutes, VM ~15minutes and CPI ~90minutes for a 128x128 image). The main source of increase in computation time of the CPI method over VM arises from the greater number of parameters to be estimated within the method. However, these figures represent non-optimized code and the method would be highly suitable for parallel implementation. The CPI method is far less computationally costly than other non-parametric Bayesian methods such as those based on Gaussian processes [20]. Whilst those methods should also provide flexibility in the residue function with smoothness constraints, they typically require a time consuming sampling procedure for their implementation. The CPI method in contrast benefits from a relatively fast non-linear model-fitting algorithm [110]. Addition of spatial prior information would considerably improve the data processing with CPI method. The algorithm processing time could be significantly improved by implementation in C/C++ and parallel processing.

3.6 Conclusion

Perfusion analysis has always been a challenge as it is an ill-posed inverse problem and commonly used SVD-based methods have been shown to underestimate the perfusion along with a non-physiological oscillatory estimate of the residue function. The use of a Vascular Model offered some improvement in perfusion estimates, but constrains the residue function to a specific set of shapes based upon assumption of microvascular physiology. Here a CPI method has been proposed to provide estimation of both residue function shape and perfusion metrics. The method retains the flexibility in residue function shape afforded by non-parametric methods through the use of control points. However, it also constrains these control points such that physiologically realistic smooth functions are favored. The CPI method has been demonstrated in simulation to provide greater CBF accuracy than the alternatives, with the flexibility to adapt to a relatively wide range of residue functions shapes. In patient data some preliminary evidence for changes in residue function shape with pathology were observed. Changes in residue function shape in vascular pathologies are expected but remain to be validated, including the effects of dispersion and the role of flow heterogeneity in the brain. However, the novel control point interpolation technique proposed here offers a viable means to measure residue function shape that has previously not been available with SVD-based deconvolution.

Chapter 4

Modeling and Correction of Bolus Dispersion Effects in DSC-MRI[2]

4.1 Introduction

Perfusion MRI is widely used in neurological diagnostic imaging for ischemia, stroke and brain tumour assessment [113,114]. Cerebral blood flow estimation using dynamic susceptibility contrast MRI requires the injection of a bolus of paramagnetic contrast agent followed by measurement of the MRI signal loss during its passage through the tissue [16,17,56]. The quantification of DSC-MRI data is based on indicator dilution theory [15,62,64], and requires the measurement of an arterial input function for the voxel-wise deconvolution of the concentration time curve calculated from the MRI signal time series.

There are multiple methods to perform deconvolution and non-parametric deconvolution techniques [17,18] have superseded the initially proposed model-based analysis [15,64,66]. Since then, singular value decomposition has been commonly used for perfusion analysis [26]. One of the typical assumptions in the DSC-MRI quantification process is the absence of bolus delay and dispersion between the site of the AIF measurement and the tissue voxel i.e. the measured AIF is assumed to reflect the exact input function to the tissue voxel being analyzed. Partial volume effects in the AIF measurement arise due to the spatial resolution of a typical DSC-MRI acquisition, whereby both arterial and non-arterial components occupy AIF chosen voxels. To minimize partial volume effects, the AIF is typically measured at a major cerebral artery, such as the middle cerebral

[2] This chapter has been published as Mehndiratta, A.; Calamante, F.; Macintosh, B.J.; Crane, D.E.; Payne, S.J.; Chappell, M.A.; *Magnetic Resonance in Medicine*. 2014

artery [69,76,77,79,80]. A global AIF is also sometimes calculated by selecting local AIFs using automatic or semi-automatic algorithms and merging these into a single global AIF [16,115]. This single AIF is then used as the input function for the whole brain and this strategy can contribute to bolus delay and dispersion. Such errors might cause inaccuracies in perfusion quantification, particularly in patients with cerebral ischemia, but they may even be present to a lesser extent in healthy volunteers [29,98].

Bolus delay has long been recognized as a source of systematic error in CBF quantification and deconvolution strategies have been designed to be delay insensitive [16,18,19,23,24,116,117]. Dispersion causes a smearing of the AIF function in time, altering the bolus profile and affecting the features of the AIF prior to its arrival at the tissue voxel [29,69,70]. If the temporal spread is not considered in the perfusion analysis modeling, these distortions can lead to considerable errors in the quantification of the perfusion parameters [29,72], which can have serious implications for diagnosis and management of patients with cerebral ischemia.

Of the various deconvolution algorithms that have been proposed in the last 15 years [16,18,19,23,24], none have fully addressed dispersion. In the current chapter the accuracy of the Vascular Model [23] and Control Point Interpolation methods (Chapter 3) will be examined in the presence of dispersion. Additionally, both methods will be extended to correct explicitly for dispersion. The effects of dispersion in perfusion quantification will be investigated on two levels: 1) in terms of CBF accuracy; and 2) the ability to isolate dispersion effects from the residue function and thus to be able to derive quantitative measures of microvascular hemodynamics.

4.2 Theory of Bolus Dispersion in Perfusion Imaging: Modeling and Analysis

According to indicator dilution theory, the concentration time curve, *C(t)*, is the result of a convolution operation between an arterial input function and the tissue residue function as in

Equation 2.9 [15,62,64]. Bolus dispersion affects the AIF, by altering its shape and amplitude while in transit between the measured AIF location and the tissue. This can be reconciled by means of dispersion parameters in the DSC model: for example, through the inclusion of a Vascular Transport Function (VTF) in convolution with the AIF [29]. The VTF thus encapsulates the effects of dispersion in a simple mathematical function, giving a modified $C(t)$ as described in Equation 2.15.

The residue function is defined as a monotonically decaying function with an initial value of one, $R(0)=1$. Once dispersion is included in the perfusion model, the sharp AIF profile is now 'smeared out' over time by the VTF. Since convolution is associative, the VTF can instead be convolved with the residue function (keeping AIF unaltered) to examine the effects of dispersion on the residue function as would be estimated by perfect deconvolution. In such a scenario, the *measured* residue function may no longer start from one (i.e. $R(0)\neq 1$) [29,69].

4.2.1 Vascular Transport Function model

The VTF depends on several factors, such as vascular topology, tissue type, site of AIF measurement, CBV and the pathological condition of the vessels (vessel lumen, elasticity, stenosis). Depending on these pathophysiological conditions, an assumed VTF kernel functional form could be employed; for example, a gamma dispersion kernel has been considered as a reasonable approximation to model the effects of dispersion as in Equation 2.24 [83]. The Gamma dispersion kernel is characterized by two parameters, sharpness, s, and time-to-peak (ttp), p. When $p=0$ and as $s \rightarrow \infty$ this kernel approximates a delta function resulting in zero dispersion; whereas with larger value of p and smaller value of s the kernel will be associated with a greater amount of dispersion [83].

4.3 Methods

4.3.1 Deconvolution methods

Block-circulant SVD, (oSVD) [18], vascular model (VM) [23], and control point interpolation (CPI) methods (Chapter 3) were used in this study. Both the VM [23] and CPI (Chapter 3), in their original implementation, were designed to model the residue function as per its fundamental definition with (*R(0)=1*). To explicitly accommodate dispersion, both methods were thus modified, as described below.

4.3.2 Dispersion Modification for VM

A gamma dispersion kernel was implemented in conjunction with VM, referred to here as VM+VTF. The VM has three parameters, CBF, δ and λ, where δ is the bolus arrival delay and λ is the shape parameter of the gamma probability density function to describe the transit times through the voxel [23]. VM+VTF has five free parameters, with the addition of *s* and *p* to describe the gamma dispersion kernel. Figure 4.1 shows the versatility available in VM with a range of λ values (0.5-100) to represent various residue functions, and the corresponding versatility in dispersed residue function shapes for VM+VTF with a typical gamma dispersion kernel.

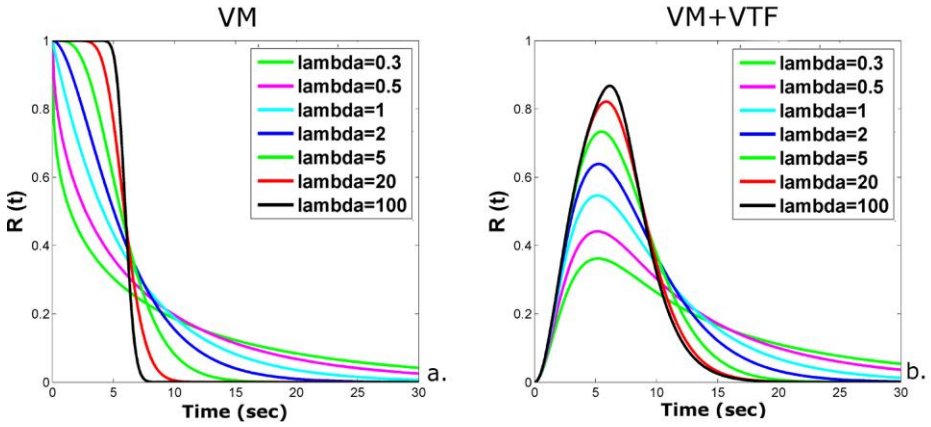

Figure 4.1: a) The family of residue function shapes that could be achieved with VM; b) corresponding family of dispersed residue function shapes which could be achieved with VM+VTF, gamma dispersion kernel with *p*=2 and *s*=0.7.

4.3.3 Dispersion Modification for CPI

In the original CPI method (Chapter 3), the residue function is estimated from a set of control points (CP) that form the basis of a smooth piecewise cubic spline interpolation. Each CP is allowed to vary in both amplitude and time, except for the first CP, which is set to 1 (CP_1=1). This CP_1 restriction therefore does not permit assessment of dispersion [112]. Two modifications were considered to accommodate dispersion in the CPI method. Figure 4.2 shows two implementations of CPI with dispersion: i) CPI_0: CP_1 fixed at 0, ii) CPI+VTF: CPI method implemented with the VTF. CPI+VTF attempts to characterize both the true underlying residue function (via the CPI residue function) and the dispersion effects (via the VTF), whereas, the CPI_0 variant retains the 'model-free' nature of the original CPI since no assumptions are made for residue function shape or for dispersion kernel. The trade-off is that it cannot separate capillary hemodynamics from dispersion; thus neither the true residue function nor the dispersion kernel can be estimated separately.

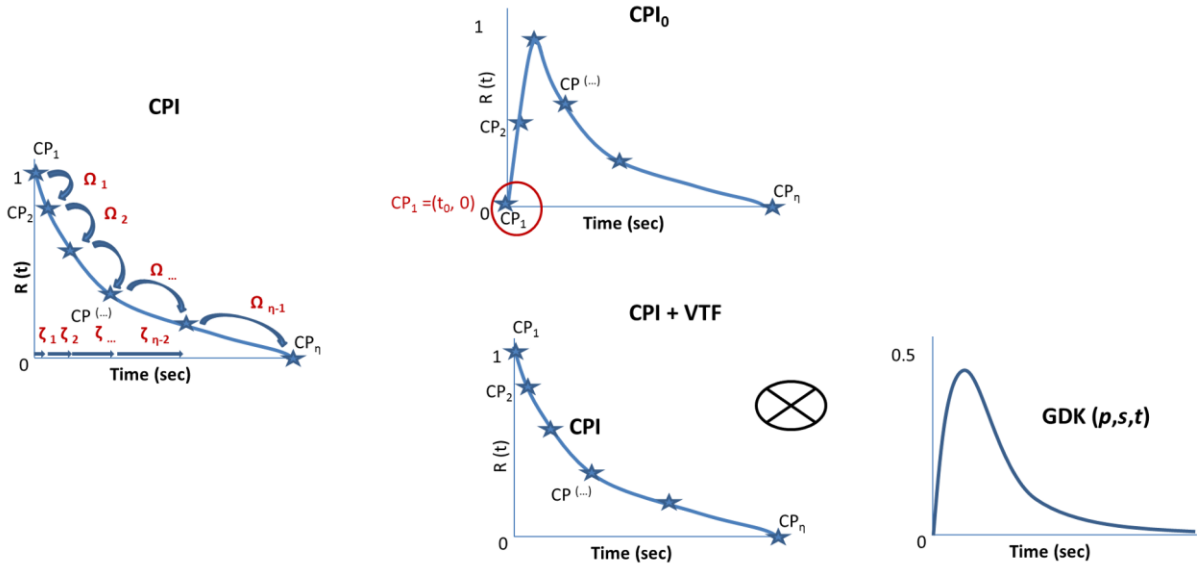

Figure 4.2: (left) Control Point Interpolation methods as elaborated in Chapter 3; (right) top: CPI_0 dispersion variant of CPI method, CP_1 fixed to zero (CP_1=0), bottom: CPI+VTF variant of CPI accounting for dispersion with Gamma Dispersion Kernel (GDK) as a function time-to-peak (*p*), sharpness (*s*) and time (*t*) as vascular transport function (VTF).

4.3.4 Implementation

The delay insensitive variant of SVD, oSVD (block-circulant SVD), was implemented as in [18]. The VM was implemented with priors supplied from the oSVD solution as described in [23], model-fitting being performed using a Bayesian non-linear model fitting algorithm [110] which is broadly similar to that used by [23]. The CPI method was implemented using the same Bayesian non-linear model fitting algorithm [110] using priors as elaborated in Chapter 3. The six deconvolution methods (oSVD, VM, CPI, VM+VTF, CPI_0 and CPI+VTF) were implemented in MATLAB using software written in-house. Note that four of the six methods were in principle able to model a dispersed residue function oSVD, VM+VTF, CPI_0 and CPI+VTF.

The Bayesian non-linear model fitting algorithm used for optimization also required prior information for the VTF. Priors for the VTF were provided in the form of a Gaussian distribution with high probability for low-to-medium level of dispersion (based on empirical preliminary analysis, data not shown); priors used on p and s were log(2)±2 (mean±SD) and the same values were used for initialization of the optimization routine. Parameters p and s were estimated on a logarithmic scale, since this makes the model more linear with respect to these parameters, aiding the convergence of the fitting algorithm, which depends upon a local approximation to the function using a Taylor expansion [110].

4.3.5 Simulations

An initial set of simulations was performed with no dispersion. Next, a range of values of bolus dispersion and delay were introduced. In all cases, accuracy was calculated as the ability to estimate CBF and to separate the effects of dispersion from the simulated tissue hemodynamics (residue function).

The AIF was simulated using a gamma-variate function as in Equation 2.16 [17,18,23]. Simulations were performed with Cerebral Blood Volume (CBV) = 4 ml/100g (4%), representative of normal grey matter [84], and CBF in the range 10-60 ml/100g/min, in increments of 10 ml/100g/min. Thus MTT varied from 4s to 24s. A well-known model of the vasculature bed as a single well-mixed compartment was assumed to model tissue hemodynamics [17]: the residue function was hence modeled as an exponential decay function, Equation 2.17. The Gamma VTF (Gamma Dispersion Kernel, GDK) was used to model dispersion, Equation 2.24 [83,112]; a range of low to high dispersion values were evaluated using the parameters shown in Table 4.1.

Figure 4.3 shows the effect of low-high dispersion (GDK) on MR signal for a typical grey matter voxel (CBF = 60 ml/100g/min). The increase in the level of dispersion is associated with an increase in the time-to-peak, decrease in the signal drop, and broadening of the tissue signal; the area under the corresponding CTC remains the same, as was also illustrated by Calamante et al. in [112].

Table 4.1: Gamma Dispersion Kernel (GDK) coefficients used in simulation for low-high dispersion in the MR signal.

Level of Dispersion	*p*	*s*
Low (L)	1	2
Medium (M)	3	1
High (H)	5	0.5

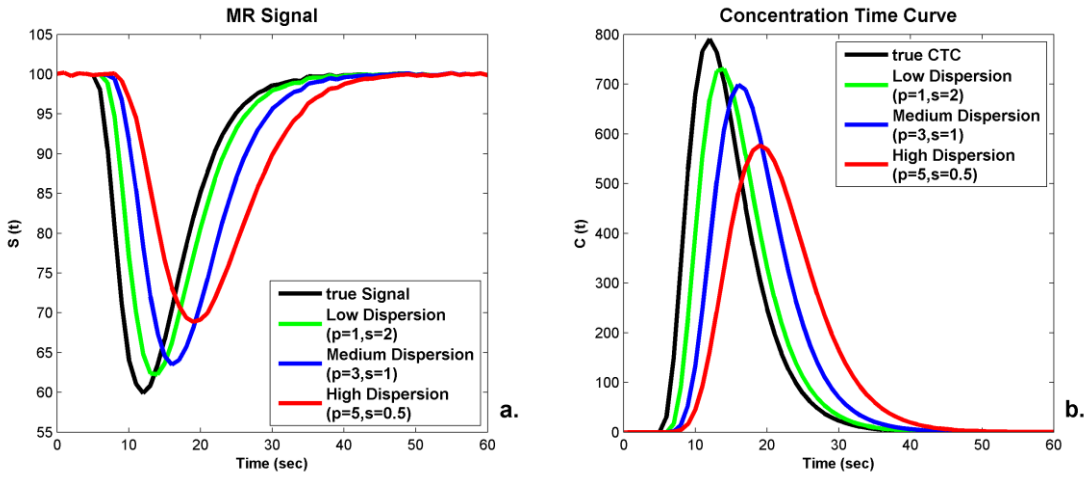

Figure 4.3: The effect of low, medium and high level of dispersion on (a) MR Signal; and (b) concentration time curve from typical grey matter using GDK.

Concentration time curves were generated using Equation 2.9 as described in [17,18]. A linear relationship was assumed between tissue relaxivity (R_2*) and $C(t)$ as in Equation 2.5 [56]. The CTC was converted to signal curves $S(t)$ with $S(t0)$ arbitrarily set to 100 and TR/TE=1s/65ms, using Equation 2.7. The linear proportionality constant was chosen such that 40% peak signal drop was achieved at a flow of 60 ml/100g/min with CBV=4% [18]. The AIF signal curve was generated similarly, but with a constant that produced a 60% peak signal drop. Zero mean Gaussian noise was added to the signal curves to produce a baseline SNR of 50. Values of 0-5s were used to evaluate the models for sensitivity with respect to bolus arrival delay (δ) and its effect when combined with dispersion. The simulations were thus performed under three conditions:

I) no dispersion and no delay;

II) dispersion with no delay: low, medium and high dispersion;

III) dispersion with delay: low, medium and high dispersion and delay (δ=0-5s).

For each combination of CBF, dispersion coefficients and delay, a total of 100 CTC were generated. Thus a total of 14,400 (6 x 4 x 6 x 100) concentration curves were analyzed during each

simulation process with six deconvolution methods: a) delay insensitive SVD (oSVD) [18]; b) vascular model (VM) [23]; c) VM+VTF; d) CPI (Chapter 3); e) CPI_0; and f) CPI+VTF.

4.3.6 In vivo Clinical Data

For empirical evaluation, the various methods were retrospectively applied to DSC data acquired on a Siemens 3T Trio using gradient-echo EPI: *TR*/*TE*=1.5sec/30msec, 78 volumes, 128x128x22 matrix, 1.7x1.7x5 mm^3 voxels. An intra-venous (IV) bolus injection of 0.1 mmol/kg Magnevist® was performed at injection rate of 10 ml/s followed by a 20 ml saline flush. DSC perfusion data were acquired from one healthy participant (age= 40yrs, male) and two patients (76yrs male and 65yrs female) with a history of atherosclerotic disease. Both of the patients had left internal carotid artery (ICA) stenosis, one with 75% and the other with 90% occlusion. Patients underwent left carotid endarterectomy (CEA) and DSC-MRI data were acquired both pre- and post-CEA. Images were acquired under an Institutional Review Board (IRB) approved protocol for DSC-MRI study as part of a larger study [111,118]. Diffusion weighted imaging (DWI) (*TR/TE* = 4.4s/93ms, b-values = 0, 1000 s/mm^2, 27slices, 1.6x1.6x3mm^3 voxels) was also acquired along with the DSC data. The AIF for the *in vivo* data was selected same as elaborated in Chapter 3 using an automated algorithm as in [111] with tail scaling technique [26]. The *in vivo* data were provided by Dr. Bradley J. MacIntosh and AIF selection was performed by David E. Crane, University of Toronto, Canada.

4.3.7 Analysis of Simulated data

The ratio of CBF (CBFratio) as estimated CBF / true CBF was calculated to quantify the absolute error in CBF estimation. rCBFratio (relative CBFratio) was also calculated by normalizing the estimated CBF in presence of dispersion against the estimated CBF with no dispersion. Calculation of rCBFratio simulates a clinical scenario where relative CBF is often measured by normalizing the whole brain with the CBF value in a contralateral ROI (where no or minimal dispersion might be

expected). The accuracy of residue function estimation for each method was evaluated by calculating the sum of squared errors (SSE) between the estimated and true residue function shapes. Statistical significance at $p<0.05$ was calculated using the Student paired t-test for comparison among methods.

4.3.8 Analysis of in-vivo data

In addition to CBF, MTT and CBV parametric maps, the residue functions obtained from deconvolution methods were also analyzed for spatial variations in shape for the patients both pre- and post-CEA. For visualization purposes, residue functions from two ROIs (2x2x1 voxels), one in infarcted and another in normal tissue, will be shown. Since the residue function is a monotonically decreasing function the time taken for the residue function to drop to 10% of its maximum value was calculated, this being referred to as *R10* maps. Larger values of *R10* would represent more time taken by the residue function to decrease, which might be an indication of tissue under hemodynamic stress [108]. To see the spatial variations in dispersion, p and S ($S=1/s$) parametric maps were also analyzed; larger values of p and S are likely to be associated with a higher amount of dispersion. Note that S is the inverse of sharpness of the GDK, such that an increase in S is associated with an increase in dispersion. Time to peak from the residue function from CPI_0 was also recorded and treated in the same way as the parameter, p, in CPI+VTF as a measure of dispersion.

4.4 Results

4.4.1 Simulations

Figure 4.4a shows the CBFratio for the six deconvolution methods for no, low, medium and high levels of simulated dispersion. Figure 4.4b shows the rCBFratio (Estimated CBF in Dispersion/No Dispersion) for low, medium and high level of simulated dispersion. The results in Figure 4.4

represent the mean (±σ) CBFratio across simulated CBF values. A nonlinear relationship was observed between estimated and true CBF values, particularly at high values, for all the methods, the same as has been observed previously in [18,23] and in Chapter 3.

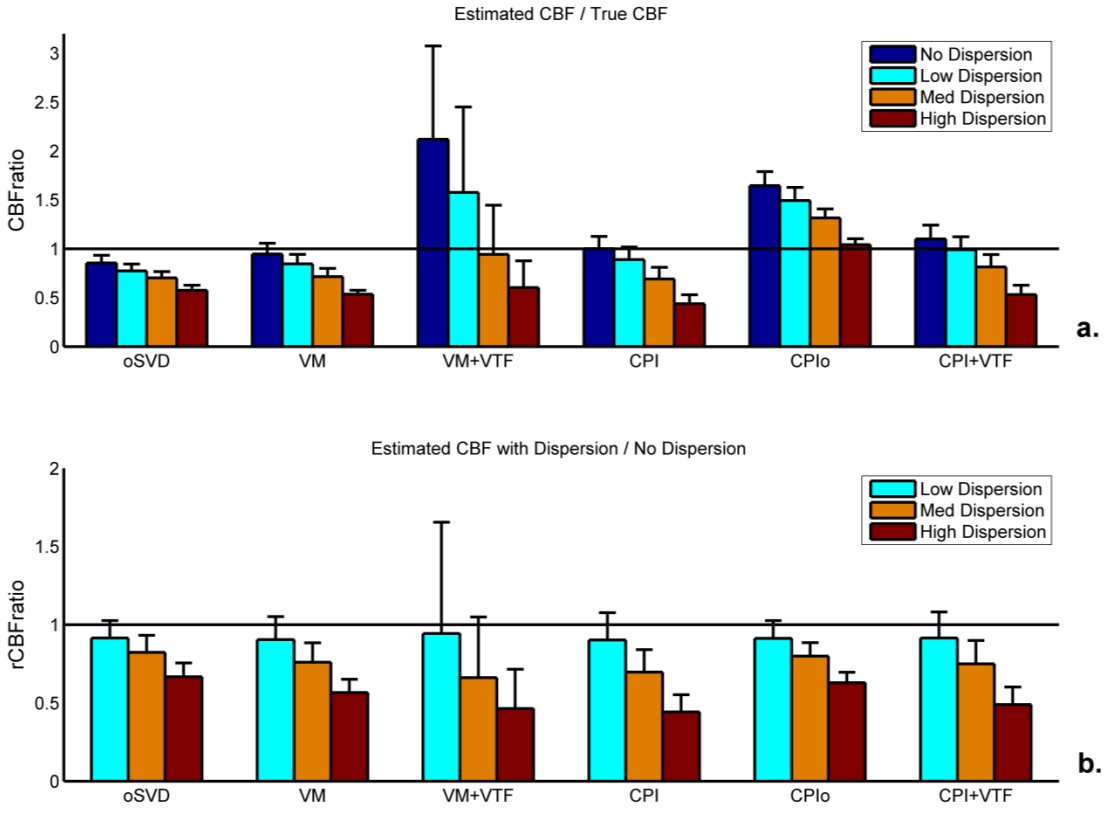

Figure 4.4: a) CBFratio (estimate/true CBF) and b) rCBFratio (estimated CBF with dispersion/no dispersion) with six deconvolution methods using Gamma dispersion kernel for simulations at no delay; black line representing line of unity.

4.4.1 No dispersion and no delay

CPI (CBFratio = 1.00±0.12) was the most accurate in case of no dispersion, followed by VM (CBFratio = 0.95±0.11) which significantly underestimated CBF ($p<0.05$). CPI+VTF (CBFratio = 1.1±0.14) significantly overestimated CBF in the case of no dispersion; whereas CPI_0 and VM+VTF overestimated CBF by approximately 1.6-2 times. Table 4.2 shows the SSE in the

estimation of residue function; the methods having the lowest SSE are marked in bold where (*) indicates statistical significance ($p<0.05$) and § indicates methods with statistically significant lower SSE within the groups but which could not be differentiated among themselves. In the case of no dispersion and no delay CPI had the lowest error, but the error with the CPI, VM and CPI+VTF methods showed no significant difference.

Table 4.2: Sum of squared error (SSE) for simulated and estimated residue function with oSVD, VM, VM+VTF, CPI and CPI+VTF at no, low, medium and high dispersion with and without delay. Lowest SSE are marked in bold.

Dispersion	oSVD	VM	VM + VTF	CPI	CPI + VTF
			No Delay		
No	0.91±0.28	0.17±0.16§	1.13±0.90	**0.14±0.18§**	0.16±0.16§
Low	1.91±0.35	0.24±0.20	0.83±0.89	0.22±0.34	**0.16±0.17***
Medium	4.28±0.51	0.83±0.42	0.63±0.47	1.19±1.26	**0.47±0.62***
High	7.25±0.16	2.69±0.72	**2.33±0.74***	6.19±3.83	3.18±2.39
			With Delay		
Low	4.77±0.49	0.26±0.24	0.32±0.46	0.56±0.66	**0.16±0.21***
Medium	6.81±0.82	0.85±0.42	**0.58±0.42§**	1.95±1.38	**0.58±0.79§**
High	9.18±1.18	2.71±0.07	**2.36±0.75***	3.32±2.38	3.06±2.36

* indicate the method with statistically significant lowest SSE ($p<0.05$)

§ indicate methods with statistically significant lowest SSE ($p<0.05$) but that are no better than each other

4.4.2 Dispersion with no Delay

As expected, the value of the both CBFratio and rCBFratio decreased when dispersion levels went from low to high (Figure 4.4). All the methods underestimated CBF in the presence of dispersion with poorer performance at the highest level of dispersion.

CPI+VTF was most accurate for absolute CBF estimation with a small standard deviation at low (0.99±0.13) and medium (0.81±0.13) dispersion values. CPI_0 tended to overestimate CBF at low and medium levels of dispersion but was most accurate compared to other methods at the highest level (1.04±0.06) of dispersion. VM+VTF was found to overestimate CBF at a low dispersion level by 1.6 times and to underestimate at medium and high dispersion levels. VM+VTF also had the highest level of uncertainty in CBF estimation among all other methods (VM+VTF: Low=1.57±0.87, Med=0.94±0.50, High=0.60±0.27).

rCBFratio calculations (Figure 4.4b) showed that at low level of dispersion all the methods were very similar in rCBF estimation, highest rCBF observed with VM+VTF (0.94±0.71) which also had the highest level of uncertainty (large standard deviation). oSVD, CPI_0 and CPI+VTF had the next best rCBFratio (with reasonable level of uncertainty) and were very similar in rCBF estimation at low level of dispersion, rCBFratio= 0.91±0.11, 0.91±0.11 and 0.91±0.17 respectively. At medium and high levels of dispersion oSVD had the highest accuracy with rCBFratio= 0.82±0.11 and 0.67±0.09 respectively, followed by CPI_0 at rCBFratio= 0.80±0.08 and 0.63±0.07, VM at rCBFratio= 0.76±0.12 and 0.57±0.08 and CPI+VTF at rCBFratio= 0.75±0.15 and 0.49±0.11 respectively.

Figure 4.5 shows the residue functions for typical grey matter (CBF=60 ml/100g/min), together with the mean of the estimated residue functions over the 100 realizations from oSVD, VM, CPI and with dispersion corrected methods. Figure 4.5a shows that in the presence of dispersion VM

and CPI tend to estimate a residue function that is broader and that decays more slowly than the true residue function. CPI+VTF could estimate the residue function accurately as illustrated in Figure 4.5b.

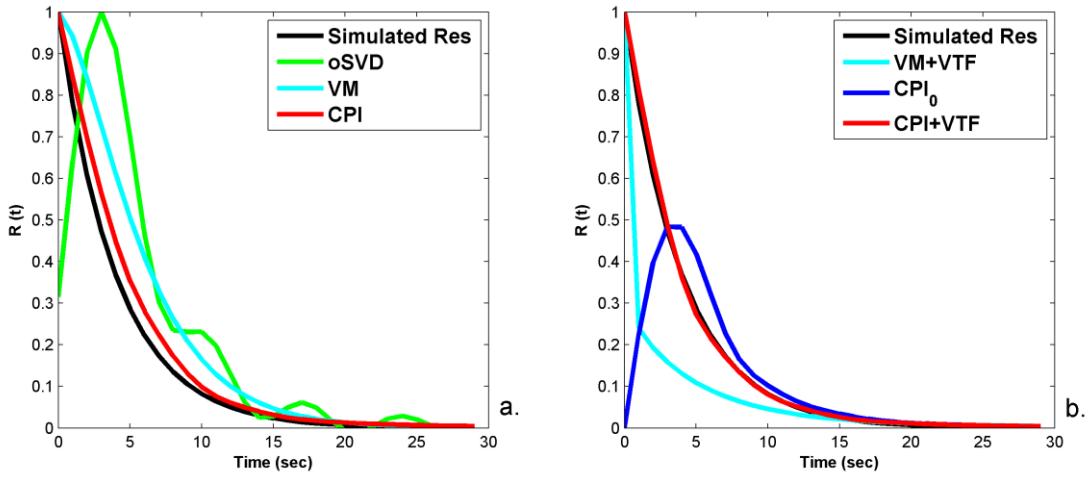

Figure 4.5: Residue function simulated for typical grey matter (CBF=60ml/100g/min) at (dispersion coefficients, p=1, s=2) and mean fit achieved with (a) oSVD, VM, CPI; (b) VM+VTF, CPI_0, CPI+ VTF.

Table 4.2 shows the sum of squared errors in the estimation of residue function shape with low, medium and high degrees of simulated dispersion. At low and medium dispersion levels CPI+VTF had the lowest error in residue function shape estimation, significantly lower than other methods. The accuracy in estimation of residue function decreases with an increase in the level of dispersion for all methods. At the highest level of dispersion all the methods were found to perform poorly, among which though VM+VTF showed the lowest error.

4.4.3 Dispersion with Delay

The methods that attempt to account for dispersion were found to perform better in the case of dispersion combined with delay. Introduction of delay together with dispersion led to an impaired performance by both VM and CPI, which was found to exacerbate as dispersion and/or delay was increased. CPI+VTF was found to be the most accurate in CBF estimation at low (CBFratio =

0.99±0.13) and medium (CBFratio = 0.80±0.14) levels of dispersion; whereas CPI_0 was more accurate at the highest (CBFratio = 1.03±0.06) level of dispersion simulated. oSVD always underestimated the CBF (CBFratio = 0.77±0.07 to 0.57±0.5) and VM+VTF overestimated CBF at low dispersion (CBFratio = 1.30±0.69) and tended to underestimate at medium and high (CBFratio = 0.85±0.35 and 0.56±0.05 respectively) dispersion levels. At the medium dispersion levels, the mean CBFratio for VM+VTF was found to be close to CPI+VTF, but VM+VTF had approximately three times higher variability than CPI+VTF. Table 4.2 shows the sum of squared errors from the estimation of residue function at low, medium and high degrees of dispersion along with delay. At low dispersion, CPI+VTF had the significantly lowest SSE ($p<0.05$) but at the medium level of dispersion CPI+VTF and VM+VTF both performed similar in residue function shape estimation.

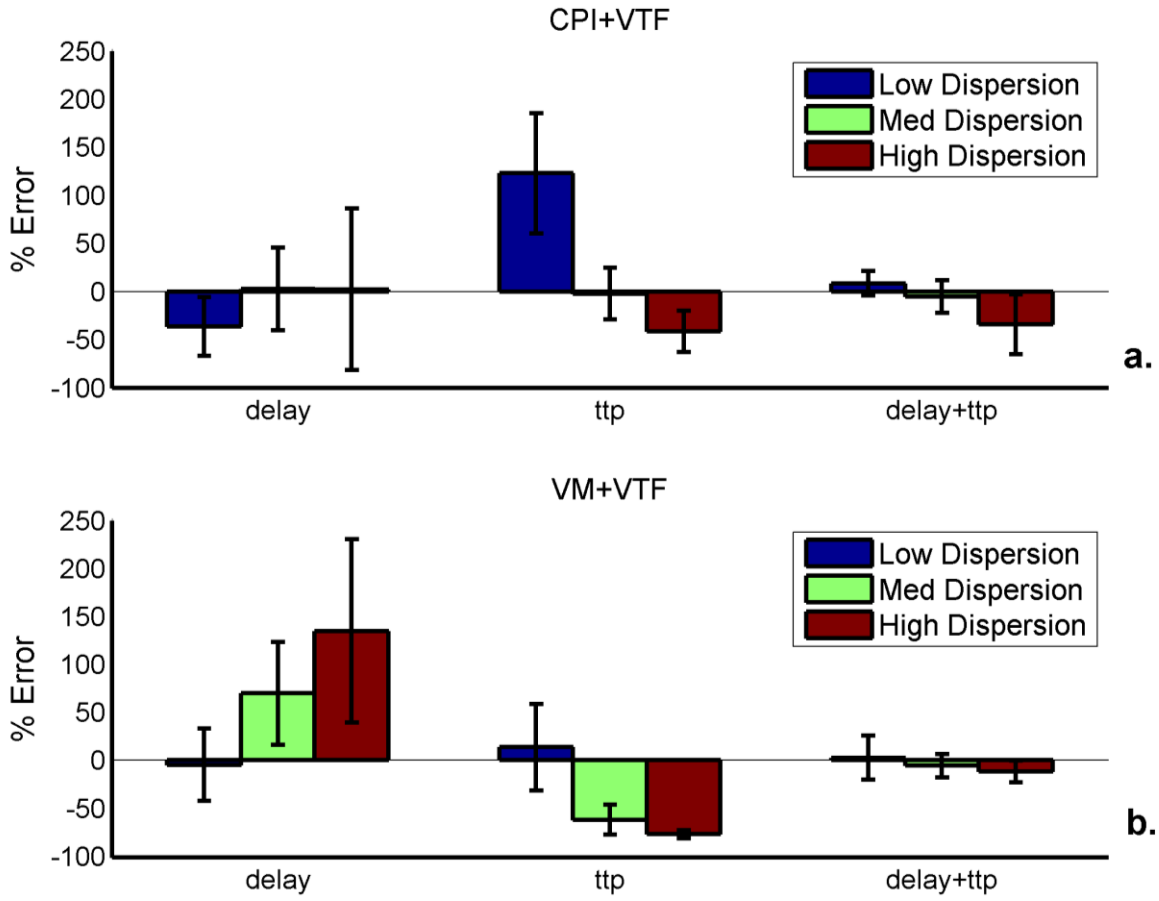

Figure 4.6: Error in estimation of delay, ttp (referred to, *p* one of the GDK parameters), and sum of delay and ttp for CPI+VTF and VM+VTF method.

Figure 4.6 shows the error in the estimation of delay and the time-to-peak of the gamma dispersion kernel (*p*) with CPI+VTF and VM+VTF. With CPI+VTF, delay was underestimated for low dispersion and overestimated with medium and high dispersion. For VM+VTF delay was overestimated and *p* underestimated. However, for both deconvolution methods the sum of delay and *p* (i.e. delay+*p*) had consistently smaller error at all dispersion values.

4.4.4 In vivo data

The oSVD estimates of CBF were the lowest among all methods; in agreement with the simulation study, VM+VTF consistently estimated the highest CBF within any given voxel (data not shown). MTT values estimated by oSVD were observed to be higher than other methods, however a larger variation in MTT was observed with other methods.

Figure 4.7 shows the MTT estimates from a patient calculated with CPI and CPI+VTF; higher values of MTT being observed in the left parietal white matter region. The DWI confirmed a region of ischemic tissue in parietal white matter (shown in Figure 4.8). CPI and CPI+VTF also showed higher values of MTT in some parts of the left MCA territory surrounding DWI positive ischemic tissue. Figure 4.7 shows the residue functions from within normal and infarcted tissue from one patient. The residue function with CPI (Figure 4.7d) was found to be broader and to decay more slowly in infarcted ROI compared to healthy ROI (Figure 4.7c) (as was also observed during simulations for dispersion in Figure 4.5). The residue function from CPI+VTF showed a faster decay compared to CPI in the infarcted ROI (Figure 4.7d), but was still broader in the infarcted ROI (Figure 4.7d) compared to the normal ROI (Figure 4.7c). The residue function from CPI_0, i.e. the dispersed residue function, also showed broadening (higher dispersion) in the infarcted ROI (Figure 4.7c) compared to the normal ROI (Figure 4.7d).

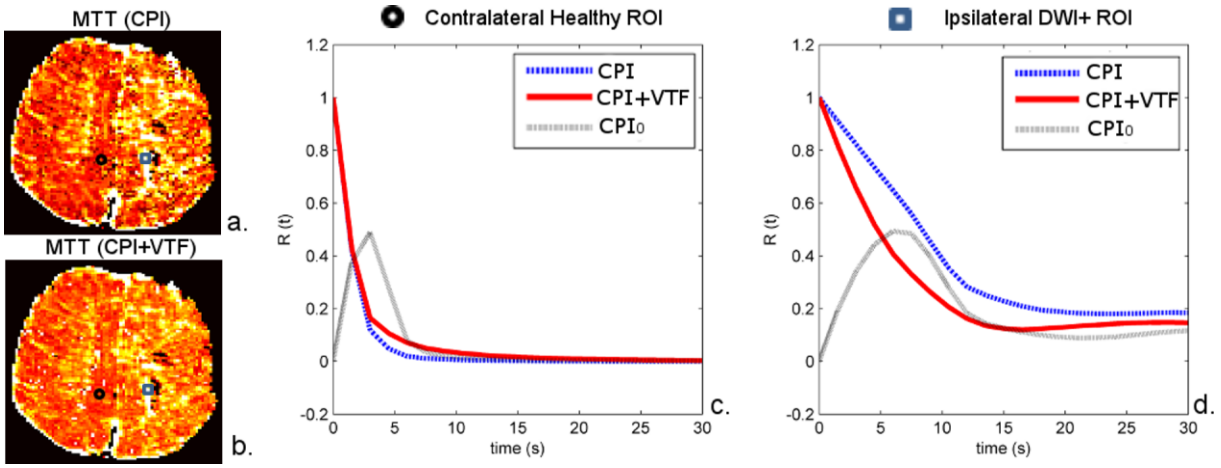

Figure 4.7: MTT maps: (a) CPI; (b) CPI+VTF; showing ROI selected in healthy and in DWI positive ischemic tissue. c) CPI and CPI+VTF shows similar residue function in contralateral ROI with no dispersion. d) Infarcted ROI showed broader and slower decay in residue function with CPI compared to CPI+VTF. CPI+VTF also showed slower decay than ROI in healthy ROI as in c. Residue function shape was more broader in ischemic ROI than normal ROI with CPI_0 method.

R10 maps for CPI and CPI+VTF, and a map of the dispersion coefficient (*S*) from the gamma dispersion kernel for CPI+VTF are shown in Figure 4.8 for the patient before and after CEA. The CPI method showed the area of infarction with very high *R10* values (Figure 4.8b), along with increased values elsewhere in the left hemisphere mainly in the MCA territory. CPI+VTF showed similar areas of higher values in *R10* (Figure 4.8c) but the values in the left MCA territory were much reduced compared to the values seen in the CPI results. The dispersion coefficient (*S*) indicated a higher amount of dispersion in the left MCA territory (arrow in Figure 4.8d). Post-CEA perfusion analysis showed a decrease in *R10* across the brain for both CPI (Figure 4.8f) and CPI+VTF (Figure 4.8g) and *S* (Figure 4.8h) with CPI+VTF methods.

Figure 4.9 shows the delay and *p* parameter value estimation from the patient; the sum of delay and *p* with CPI_0 and CPI+VTF were found to closely resemble the delay estimated by the CPI method, as will be described below.

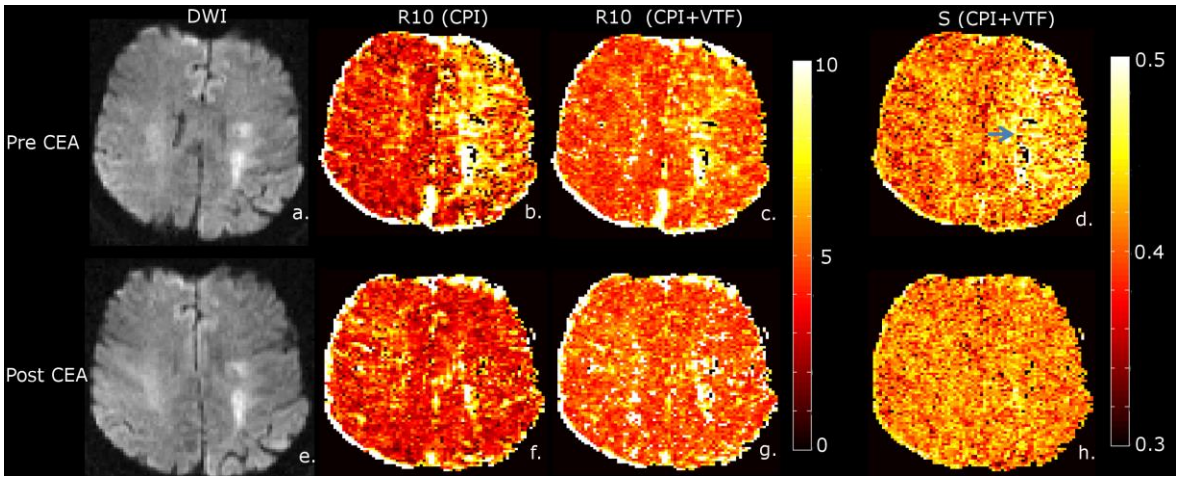

Figure 4.8: DWI (a, e), *R10* (b, c, f, g), *S* (dispersion) (d, h) maps for CPI (b, f) and CPI+VTF (c, d, g, h) showing area of infarction (from DWI) with higher values of *R10* with both CPI and CPI+VTF. b) *R10* with CPI also showed higher values in left MCA territory which improved post-CEA (f). c) *R10* with CPI+VTF showed much reduced values in left MCA territory where high amount of dispersion was found (marked with arrow in d.). Dispersion was found to completely decrease post-CEA (h).

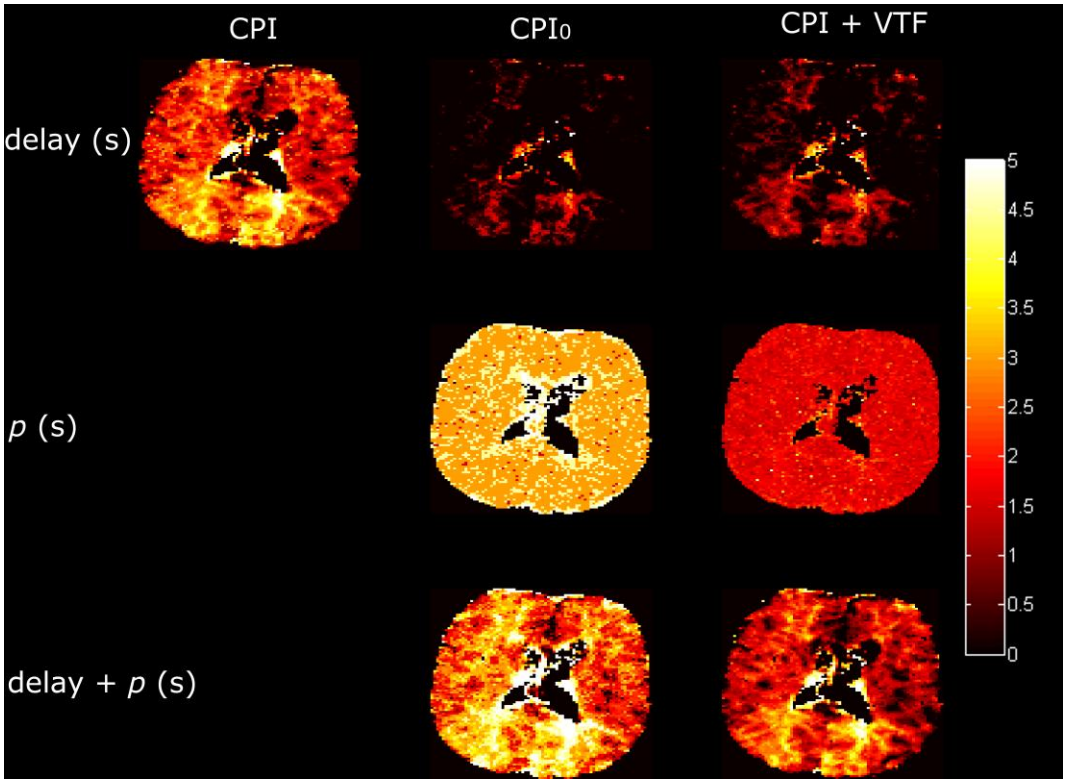

Figure 4.9: (top) Estimated delay with CPI, CPI_0 and CPI+VTF; (middle) *p* and (bottom) delay+*p*. Delay estimate with CPI appears similar to the delay+*p* estimate with other two methods, highlighting the ambiguity in delay and *p* estimation during the deconvolution process.

4.5 Discussion

Bolus dispersion is challenging to quantify in DSC-MRI, and more problematic in clinical populations such as cerebrovascular patients [29,30,112]. In the current chapter, analysis methods have been developed as a means to assess dispersion and how it contributes to error in: 1) CBF estimation; and 2) tissue residue function estimation. It was found that in the presence of dispersion the accuracy in CBF estimation is considerably improved with dispersion corrected CPI methods and that this also allows for separation of the tissue residue function from effects of dispersion with greater accuracy. The CPI+VTF method corrected the residue function for dispersion and showed variation in tissue residue function in *in vivo* data from patients with atherosclerotic diseases.

Calamante et al. [112] showed that dispersion reduces the accuracy in CBF estimation when using the standard SVD methods by as much as 70% [30]. Similar findings were observed in this study, where oSVD was found to underestimate absolute CBF by a large amount (CBFratio: range 0.57-0.77). However, modified methods designed to specifically handle dispersion, (VM+VTF, CPI+VTF and CPI_0), were more accurate in absolute CBF estimation (CBFratio: range 0.94-1.04). CPI+VTF was most accurate in CBF estimation at low to medium levels of dispersion whereas CPI_0 was better at high level of dispersion.

However, due to the practical difficulties with quantifying CBF in absolute units [76], relative CBF measurements are often used in the clinical evaluation of patients with vascular abnormalities, by making a comparison of the CBF in a region in the contralateral hemisphere. For simulations, relative CBF measurements were best performed by oSVD (rCBFratio=0.67-0.91) over a range of simulated dispersion; which was followed by CPI_0 (with rCBFratio=0.63-0.91). However, the better performance of oSVD for rCBF quantification is primarily a result of serendipitous underestimation of CBF both in the presence and absence of dispersion. It is clear from the other results that oSVD

does not inherently handle dispersion well and is substantially affected when it comes to absolute quantification, leading to a poor characterisation of the shape of the true residue function. For rCBF calculation it is therefore apparent that methods that explicitly correct for dispersion do not necessarily offer a direct advantage, and their major role is when the shape of the residue function is of interest or when absolute quantification of CBF is required.

In vivo neither the actual residue function shape nor the effects of dispersion (VTF) are known *a priori*, particularly in pathological conditions. Thus it might be useful to evaluate the performance of the methods (including CPI+VTF) under plausible variation in macrovascular dispersion and microvascular residue function. To investigate the variation in residue function, additional data were generated using a linear (Equation 2.18) and Lorentzian (Equation 2.20) residue function and the similar methodology used above. Table 4.3 shows the error in estimation of true linear and Lorentzian residue function. For both linear and Lorentzian function CPI and CPI+VTF both had the lowest error but no better than each other.

To investigate effects of variation in dispersion, additional data were generated using exponential dispersion kernel (EDK) as in Equation 2.23 and log-normal dispersion kernel (LNDK) as in Equation 2.25 at low, medium and higher dispersion values. For EDK, dispersion coefficient θ with value of 1s, 2s and 4s was used to model low, medium and high dispersion respectively; and for LNDK values were used as recommended by Calamante el al. in [76] (low: $\mu_{lk} = -1.0$ and $\sigma_{lk} = 1.0$s, medium: $\mu_{ln} = -0.15$ and $\sigma_{ln} = 0.75$s and high: $\mu_{ln} = 0.59$ and $\sigma_{ln} = 0.78$s). Concentration time curve and signal were generated with similar methodology used above. Analysis was performed with all six methods as above; note in analysis CPI+VTF method still used a gamma dispersion kernel to model the effects of dispersion. Table 4.4 shows sum of squared error in estimation of the true

residue function for simulated EDK and LNDK. The CPI+VTF consistently showed significantly lowest error compared to other methods.

Table 4.3: Sum of squared error (SSE) for simulated linear and Lorentzian residue function and estimated functions with all the methods at low dispersion using GDK with no delay. Lowest SSE are marked in bold.

Residue function	oSVD	VM	VM + VTF	CPI	CPI + VTF
Lorentzian	1.89±0.35	0.34±0.24	0.85±0.75	**0.15±0.22**§	0.19±0.17§
Linear	1.78±0.33	0.57±0.27	1.25±1.09	**0.22±0.28**§	0.23±0.23§

* indicate the method with statistically significant lowest SSE ($p<0.05$)

§ indicate methods with statistically significant lowest SSE ($p<0.05$) but are no better than each other

Thus it can be concluded that the CPI+VTF approach provides a method to avoid the strict model-based assumptions for the microvascular residue function (same as CPI method in Chapter 3) with a plausible approximation of the macrovascular dispersion kernel whilst still offering a smooth interpretable residue function estimate. Using CPI+VTF a better estimation of CBF was achieved even in the presence of dispersion in simulations. CPI+VTF was also found to isolate the effects of dispersion and to estimate cerebral hemodynamics at low and medium levels of dispersion, which represents the most likely clinical scenario. All methods performed poorly at extreme levels of high dispersion, suggesting that this may well present a limit to what can be accommodated in perfusion analysis.

In order to account for dispersion effects which cannot be parameterized, a non-parametric deconvolution method accommodating dispersion has also been proposed in this study in the form of CPI_0. CPI_0 performed within acceptable limits in CBF estimation but the residue function and

dispersion remained inseparable. The estimated residue function has the combined information of the residue function and dispersion similar to the SVD solution, although with the benefit of no oscillations.

Table 4.4: Sum of squared error (SSE) for simulated and estimated residue function with all methods at low-high dispersion with no delay using EDK and LNDK. Lowest SSE are marked in bold.

Dispersion	oSVD	VM	VM + VTF	CPI	CPI + VTF
			LNDK		
Low	1.26±0.32	0.25±0.22	0.88±0.83	0.24±0.42	**0.15±0.19***
Medium	1.55±0.32	0.28±0.24	0.79±0.74	0.21±0.27	**0.15±0.15***
High	2.61±0.43	0.64±0.40	0.73±0.82	0.73±0.85	**0.34±0.45***
			EDK		
Low	1.41±0.33	0.30±0.24	0.77±0.75	0.27±0.45	**0.14±0.16***
Medium	2.20±0.40	0.65±0.38	0.75±0.85	0.77±0.91	**0.35±0.49***
High	3.88±0.61	1.94±0.74	1.69±1.13§	2.83±2.33	**1.53±1.35§**

* indicate the method with statistically significant lowest SSE ($p<0.05$)

§ indicate methods with statistically significant lowest SSE ($p<0.05$) but are no better than each other

It is already known that the broadening in the DSC time course caused by dispersion might be interpreted as an increase in the MTT if the analysis does not account for dispersion [29]. This source of error then propagates to the CBF estimation, leading to underestimation. In this case, the tissue response function would appear to be broader and to decay more slowly (an effect of

apparent increase in MTT) compared to the true response function. Such effects were observed in this study when the analysis was performed with the original implementations of VM and CPI that cannot accommodate dispersion (Figure 4.5), with the estimated residue functions having slower decay when compared to those simulated. VM+VTF and CPI+VTF were found to perform better in such cases, as the dispersion can now be accommodated in the estimated vascular transport function.

For the *in vivo* data, the residue function estimated by CPI in the infarcted ROI was found to be broader and with a slower decay (Figure 4.7) for the patient with atherosclerotic disease compared to a healthy scenario. This was also seen in the *R10* map (Figure 4.8). The residue function when assessed with CPI+VTF in the same infarcted ROI decayed faster than the CPI estimate; this would imply the presence of dispersion, as suggested by the simulation study. Higher values of *S* (dispersion coefficient) in the left MCA territory (Figure 4.8) with CPI+VTF were further evidence of dispersion in this region. The CPI+VTF results suggest that, while there was a contribution from dispersion, there was still some variation in residue function associated with the infarcted tissue, as could be clearly seen by a broader residue function with CPI+VTF in an infarcted ROI compared to a more rapid decay in the normal ROI (Figure 4.7c,d). This is reasonable since changes in the microvasculature and thus the residue function would be expected in infarcted tissue. The wider region of a slower residue function decay observed in the left MCA territory with CPI was absent from the results obtained from CPI+VTF, implying that there were no substantial observable changes in the microvasculature in this region, but that the effect was primarily due to dispersive effects (Figure 4.8). It was also later observed in the post carotid endarterectomy perfusion analysis (Figure 4.8f-h), where these dispersive effects were not observed with either of the methods (CPI or CPI+VTF).

It was found that the sum of delay and *p* (from the vascular transport function) can be estimated with a reasonable degree of accuracy even though; the errors in the two parameters are highly correlated. This is not surprising since the effects of both delay and dispersion on the DSC signal are similar, both causing a temporal shift in the peak signal drop. This can be appreciated from the curves shown in Figure 4.3: while some of these curves appear to be delayed, they were simulated with dispersion but no delay. In reality, when combined with a VTF the delay parameter only characterizes the delay for the leading edge of the input function to arrive, whereas *p* effectively characterizes the delay introduced to the bulk of the input function by dispersion. Thus, in previous work with delay correction [18,23], where the effects of dispersion have been ignored, it is likely that the estimates of delay accounted (to some extent) for both effects. This means that the values used in simulation here are liable to be more extreme than those found in reality. The ambiguity between delay and dispersion was not found to have a substantial impact on the CBF or residue function shape estimation for CPI+VTF; although it did impact the accuracy of estimation of the other dispersion parameter, *S*. In practice, a relationship between delay and the extent of dispersion might be expected [119], since both should increase with distance from AIF site to tissue voxel. Such a relationship could, in principle, help to constrain the problem further, possibly increasing the robustness of methods to correct for dispersion effects. However, the exact relationship, if such does exist, remains to be determined.

It might be expected that the CBF estimation could be improved, and the residue function and effects of dispersion separated, if a model-based approach for tissue vasculature is used, parameterizing both the residue function and effects of dispersion. However, the results of these simulations suggest that a model-based deconvolution (VM+VTF) cannot clearly distinguish the two, leading to errors in CBF estimation and a significant amount of uncertainty in both CBF and the residue function shape. It was observed that variations in the signal time course from the

VM+VTF model were similar for changes either in the dispersion parameters or in the parameters of the VM transit time distribution, most probably because both are defined by gamma distributions. Thus, there would be substantial ambiguity when estimating either set of parameters.

A metric based on the time for the residue function to decay to 10%, *R10*, has been used here to characterize the residue function *in vivo*. This is a recognition of the fact that whilst we might be able to estimate the residue function, its interpretation still needs to be more fully explored. *R10* in particular measures changes in the tail of the residue function and is thus associated with long transit times through the voxel. Thus it may capture information beyond that already found in the MTT parameter. Extracting the capillary hemodynamic information from the residue function by calculating the transit time distribution and the clinical significance of such measurements will be further assessed in the next chapter.

One possible limitation of the study was the assumption of a gamma kernel to characterize dispersion effects. A number of other functions have been used in the literature to model dispersion [29,30,69,72,76,112], for example, an exponential dispersion kernel has previously been used for DSC [29,83]. In practice the exponential kernel represents a special case of the family of gamma dispersion kernels, with $p=0$. Therefore, the gamma kernel provides a fairly flexible model for the VTF. An alternative to dispersion correction is the use of methods that derive local AIFs [77,99–106], these would bypass the errors introduced using analytical dispersion kernels. However, they suffer from issues due to partial volume effects [79,80] and these are difficult to reduce. Additionally, it still remains to be validated whether these methods can reliably measure the local AIF.

4.6 Conclusion

This chapter describes a method to improve the accuracy of CBF estimates with CPI when dispersion is present. The method developed did not fully resolve the ambiguity between the true residue function and dispersion; however, incorporating an additional vascular transport function model did show benefits. A reasonable separation of tissue hemodynamics and bolus dispersion can now be achieved with this approach for low to medium levels of dispersion. It remains to be seen what strategies should be used, however, when there is very high levels of dispersion. The modified CPI approach appears to provide a useful tool for the analysis of DSC-MRI data in patients with vascular abnormalities.

Chapter 5

Cerebral Hemodynamics beyond CBF

5.1 Introduction

Although DSC-MRI is a quantitative perfusion methodology, in current clinical settings it is mostly used for qualitative assessment. In diagnostic imaging the two hemispheres of the brain are routinely compared for signs of pathological variations in an individual patient. Population based standardization of quantitative DSC-MRI is a big challenge because cerebral blood volume and cerebral blood flow are both measured in relative units; mean transit time is the only parameter estimated in absolute units (seconds) [6,120,121]. MTT thresholds have thus been defined to differentiate the health status of the tissue (normal or ischemic) [121–124]. MTT is widely accepted as a perfusion metric in clinical decision making [121,125], research interest has also been shown in the study of tissue hemodynamics beyond CBF and MTT, including parameters such as flow heterogeneity [11,12] and tissue oxygenation [9,10]. Changes in tissue hemodynamics have been associated with the tissue oxygenation status and hence its metabolic state [10,126,127]; capillary hemodynamics have been suggested to affect local oxygen delivery [128]. According to direct microscopy studies in rats [11,12] and by perfusion studies in patients with stroke [129–131], it has been speculated that capillary hemodynamics might undergo profound changes in cerebral ischemia. More accurate estimation of the tissue residue function though perfusion imaging might thus provide further evidence about changes in capillary hemodynamics in pathology.

The residue function shape depends on the distribution of transit times through the tissue and its shape encapsulates information about capillary hemodynamics [8,9] including a parameter that has

been referred to as capillary transit time heterogeneity (*CTTH*) [10]. Recent research interest has focused on the use of the shape of the residue function to understand the underlying cerebral hemodynamic properties, variations in hemodynamics during the process of evolution of stroke and possible diagnostic implications [18,20,22,24]. However, this could not previously be achieved because of the oscillatory nature of the residue functions observed with the most frequently used SVD deconvolution method and its variants [17,18,22]. The non-physiological behaviour of the residue function makes it impossible to interpret it further for clinical decision making.

The Control Point Interpolation method proposed for DSC-MRI perfusion analysis in Chapter 3 has demonstrated the possibility of estimating a smooth residue function shape for *in-vivo* clinical data. In Chapter 4 CPI was further improved to correct for bolus dispersion. The motivation of this chapter is to evaluate CPI and its dispersion variant on a clinical dataset and to investigate the residue function behaviour in patients with atherosclerotic disease. Capillary hemodynamic information will be extracted from the residue function in the form of novel parameters, and the relevance of these new parameters for clinical decision making will be evaluated.

5.2 Material and Methods

5.2.1 Study I (n=17)

DSC-MRI data were collected with an Institutional Review Board approved protocol as part of a larger study [118]. Volunteers had the study procedure explained to them and written consent was obtained before scheduling the MR imaging. Two healthy control subjects (n=2) (29yrs and 40yrs, male:female=1:1) consented to take part in the study; seventeen patients (n=17) scheduled to undergo carotid endarterectomy (CEA) also consented to participate in this study. All patients had ≥65% stenosis of at least one carotid artery. The mean age (±SD) of participants included in the study was 69.7±10.4 years (12:5 males:females). The mean carotid stenosis ipsilateral to the side of

CEA was 79±8% (range: 65-90%), while the contralateral stenosis was 40±29% (range: 0-100%). All the percentage stenosis measurements were based on duplex sonography. Table 5.1 shows the demographics of the seventeen patients included in the study along with percentage stenosis of both carotid arteries and the presence or absence of any infarction based on visual assessment of the diffusion weighted imaging. The *in vivo* data was provided by Dr. Bradley J. MacIntosh and AIF selection was performed by David E. Crane, University of Toronto, Canada.

5.2.2 MRI Data Acquisition

Imaging was performed 48 hours prior to and within 24 hours following CEA surgery on a Siemens TIM Trio 3 Tesla MRI scanner (Siemens Healthcare, Erlangen, Germany) with a 12-channel head coil. Both the sessions were conducted in the early morning with imaging consisting of gradient-echo (EPI) (*TR*/*TE* = 1.5s/30ms. 22 slices, 78 volumes, flip angle = 70^0, 128x128 matrix, 1.7x1.7x5mm^3 voxels, generalized autocalibrating partially parallel acquisition (GRAPPA) with acceleration factor 2), diffusion weighted imaging (DWI) (TR/TE = 4.4s/93ms, b-values = 0, 1000 s/mm^2, 27slices, 1.6x1.6x3mm^3 voxels), pre-gadolinium contrast and 10 minutes post contrast T1-weighted acquisition (TR/TI/TE = 1.8s/900ms/4.4ms, flip angle = 8^0, 6/8th partial k-space, axial MP-RAGE, matched to DSC, 1.7x17.x2mm^3 voxels). DSC acquisition parameters were chosen in order to adhere to the stroke imaging guidelines [132] with chelated gadolinium contrast agent at a dose of 0.1 mmol/kg Magnevist®, injection rate of 10 ml/s followed by a 20 ml saline flush.

5.2.3 Image Analysis

Block-circulant Singular Value Decomposition (oSVD) [18] and Control Point Interpolation, CPI+VTF (CPI with dispersion correction) methods were used for perfusion analysis. The implementation of oSVD and CPI methods was performed using MATLAB (MathWorks, Natick, MA) with in-house algorithms. The oSVD method was implemented as in [18], CPI was

implemented as described in Chapter 3 and CPI+VTF as in Chapter 4. For deconvolution the AIF selection was performed using an automated algorithm [111], using the tail scaling technique [26].

Table 5.1: Patient information: Age, gender, % occlusion, side of CEA and DWI status.

Subject	Age(yrs) / Sex	Left (%)	Right (%)	CEA-side	DWI (side L/R)
1	76 / M	85	30	Left	
2	76/ M	85	0	Left	
3	67 / F	80	40	Left	
4	72 / F	65	65	Left	
5	53 /M	65	25	Left	
6	74 / M	100	80	Right	
7	76 / M	75	20	Left	
8	52 / F	75	45	Left	
9	74 / M	80	15	Left	
10	85 / M	80	0	Left	Yes (Left)
11	65 / M	80	90	Right	Yes (Right)
12	76 / M	75	60	Left	
13	65 / F	90	40	Left	Yes (Left)
14	71 / M	90	40	Left	
15	47 / M	65	0	Left	Yes (Left)
16	76 / M	70	80	Right	
17	80 / F	80	50	Left	Yes (Left)
mean±SD	**69.7±10.4**	**79±10**	**40±28**		

5.2.4 Hemodynamic Parameters from CPI and CPI+VTF

Mean Transit Time was calculated based on the central volume theorem as described in Chapter 2. Residue functions obtained from CPI and CPI+VTF method were then analyzed for variations in shape and capillary heterogeneity. The transit time distribution, *h(t*), in the tissue voxel was calculated by numerical differentiation of the residue function as in [8] derived from Equation 2.8:

$$h\,(t) = -\frac{d\,R(t)}{d\,t} \qquad \text{Equation 5.1}$$

where *h(t)* is the tissue capillary transit time distribution and *R(t)* is the residue function.

The Standard Deviation of the transit time distribution was used as a measure of capillary transit time heterogeneity (*CTTH*) [10], calculated from:

$$CTTH = \sqrt{E(h^2) - MTT^2} \qquad \text{Equation 5.2}$$

where *E(x)* is the expectation of *x*, MTT being calculated from the data using the central volume theorem. Smaller values of *CTTH* represent a more homogeneous distribution whereas a larger value represents a broader distribution with more heterogeneity. Skewness (*Skw*) of the transit time distribution was also used to quantify the asymmetry in the transit time distribution, calculated from:

$$Skw = E\left(\left[\frac{h - MTT}{CTTH}\right]^3\right) \qquad \text{Equation 5.3}$$

A higher positive value indicates an asymmetric transit time distribution with a longer tail towards the higher transit times, indicative of a greater contribution of lower transit times to the transit time distribution, whereas a lower positive value suggests less asymmetry, thus a more equal contribution from lower and higher transit times. Negative values of Skewness would be suggestive

of a longer tail towards lower transit times in the transit time distribution, suggestive of large contributions from the higher transit times.

5.2.5 Study II (ROI Study, n=5)

A subset of patients (n=5) from the study I cohort showing infarction in the DWI was included in this ROI-study to characterize the residue function changes in and around the infarcted tissue. Rigid body image registration was performed for perfusion and diffusion weighted images using FMRIB's Linear Image Registration Tool (FLIRT) from the FSL toolbox [133]. Residue function characteristics were evaluated from a Region of Interest (ROI) based on DWI and perfusion weighted images using three criteria [121]:

I. **Normal** – ROI in normal perfused tissue in the contralateral hemisphere that was outside the hypoperfused and DWI infarct tissue;
II. **DWI-ring** – ROI in tissue with perfusion deficit and around DWI tissue but normal DWI properties;
III. **DWI+** – ROI in infarct tissue within a DWI lesion.

A ROI of 2x2 voxels was manually selected through simultaneous visual inspection of the perfusion and diffusion weighted imaging data. A maximum of four ROIs were selected from each patient in the respective groups of Normal, DWI-ring and DWI+ tissue. In total 20 ROIs were selected from five patients in the Normal, 20 ROIs in the DWI-ring and 20 ROIs in the DWI+ group.

5.2.6 Statistical Analysis

Study I

Mutual Information (MI) was calculated to assess the amount of information shared between estimated parameters. MI is measured in relative units; however for comparison a higher value represents a large amount of information common to both parameters being evaluated and a lower

value suggests orthogonality in the two estimated parameters with little shared information. The Student paired t-test was used to calculate the statistical significance ($p<0.05$) in MI amongst the three hemodynamic parameters being evaluated (MTT, *CTTH*, Skw). Parameters with the least shared information would be expected to complement each other and the addition hemodynamic information now available in new parameters need to be evaluated further for its clinical significance.

Study II

Median and percentile distribution of MTT, *CTTH* and *Skw* for the three ROI groups was calculated and a box and whisker plot is used to show the differences. The Student paired t-test was used to measure the statistical significance ($p<0.05$) between the three tissue types and also to compare pre- and post-surgery values. Variations in estimated MTT values with *CTTH* and *Skw* values were compared with the model predictions for tissue oxygenation using a new hemodynamic model by Payne (Appendix I). A scatter plot is used to illustrate the variation in estimated MTT with *CTTH* and *Skw* along with these model predictions. The hemodynamic model by Payne (Appendix I) models capillary network with a baseline $CMRO_2$ of 100% for a normal tissue and then can estimate the variation in hemodynamics at multiple $CMRO_2$ levels.

5.3 Results

Results from study I shows qualitative hemispherical comparisons for patients both pre- and post-CEA using novel hemodynamic parameters. Results from Study II focus on quantitative analysis of hemodynamic parameters showing variations between normal tissue and tissue with hemodynamic disturbances using information from both perfusion and diffusion weighted imaging.

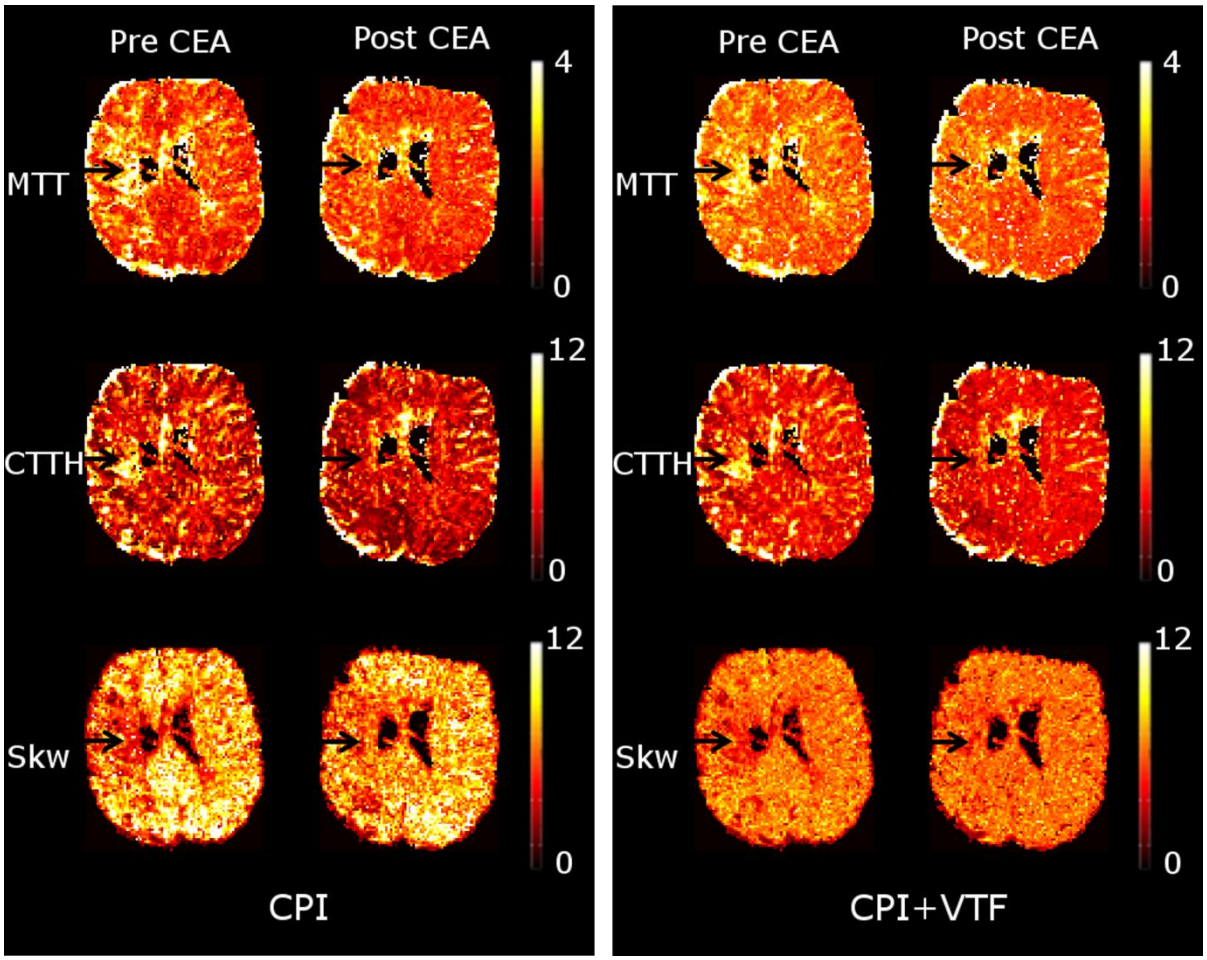

Figure 5.1: Axial brain slice from a patient with atherosclerotic disease showing MTT, *CTTH* and *Skw* both pre- and post-CEA obtained with CPI and CPI+VTF. MTT and *CTTH* tend to reduce towards normal values (arrow) and *Skw* tend to increase to normal values (arrow) after CEA.

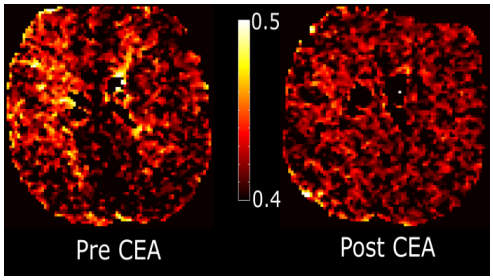

Figure 5.2: Dispersion estimates obtained with CPI+VTF both pre- and post-CEA for the patient in Figure 5.1.

5.3.1 Study I

On analysis with CPI and CPI +VTF, six patients were found to show increase in cerebral perfusion after CEA, five patients showed a decrease in perfusion and six showed no change after CEA. Figure 5.1, taken from a representative patient, shows an increase in tissue perfusion after CEA. Pre-surgery maps show high values of MTT in the right MCA territory which appear to decrease to normal (same as contralateral hemisphere values) post-surgery. The *CTTH* value is higher in the right MCA region compared to the contralateral left side before surgery; the *CTTH* in the right side reduces to values similar to those on the contralateral side after surgery. *Skw* values are lower in the right MCA region before surgery, increasing to values similar to those on the left contralateral hemisphere after surgery. Similar changes in hemodynamics are observed with both the CPI and the CPI+VTF method. Right-Left hemispherical differences are qualitatively more clearly visible in pre-surgery images with CPI when compared to those obtained using CPI+VTF. Figure 5.2 shows the respective dispersion estimates from the CPI+VTF method both pre- and post-CEA for the patient illustrated in Figure 5.1. A higher amount of dispersion is observed in the right MCA territory pre-CEA which was found to reduce post-CEA.

Figure 5.3, taken from a representative patient, shows a decrease in tissue perfusion after CEA. The right MCA territory shows an increase in MTT and *CTTH* after CEA and a reduction in *Skw* both with the CPI and the CPI+VTF methods. The changes in MTT, *CTTH* and *Skw* are observed to be opposite to the ones observed in the patient showing an increase in tissue perfusion after CEA, as in Figure 5.1. Figure 5.4 shows the estimated dispersion obtained with CPI+VTF both pre- and post-CEA for the patient illustrated in Figure 5.3. A higher amount of dispersion is observed in the right MCA territory in pre-CEA perfusion analysis that does not appear to reduce even after CEA.

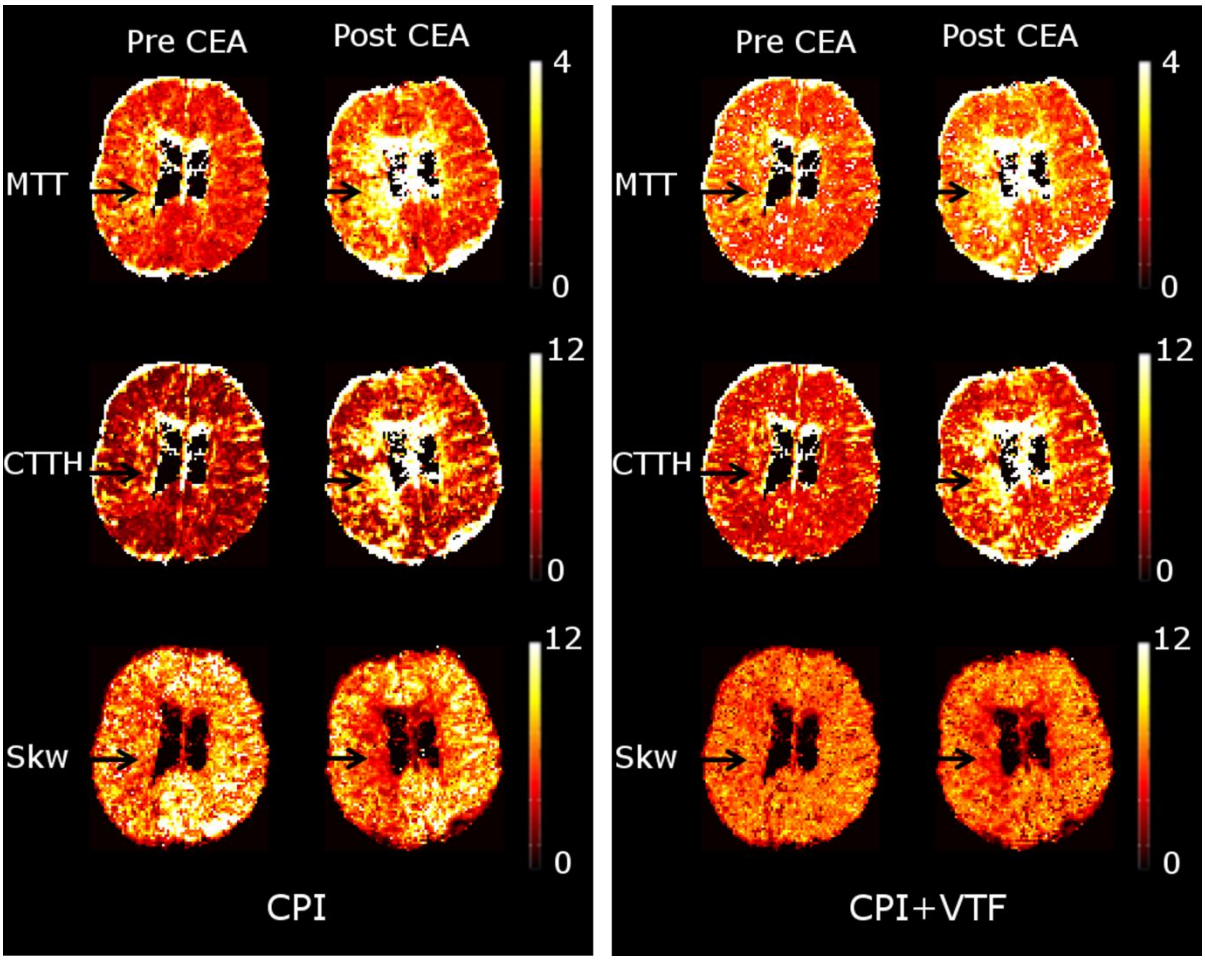

Figure 5.3: Axial brain slice from a patient with atherosclerotic diseases showing MTT, *CTTH* and *Skw* both pre- and post-CEA obtained with CPI and CPI+VTF. MTT and *CTTH* tend to increase (arrow) and *Skw* tends to decrease (arrow) after CEA.

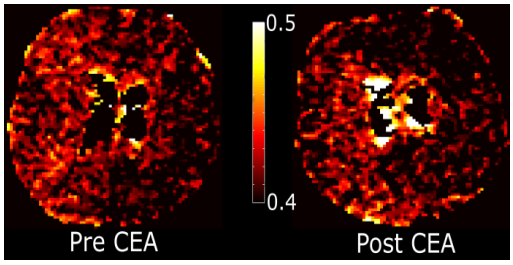

Figure 5.4: Dispersion estimates obtained with CPI+VTF both pre- and post-CEA for the patient in Figure 5.3.

Table 5.2 shows the MI calculated between MTT, *CTTH* and *Skw* from all seventeen patients both pre- and post-CEA obtained with CPI and CPI+VTF. With the CPI method, the combination of *CTTH* and *Skw* shows significantly lowest MI ($p<0.05$) compared to MTT-*CTTH* and MTT-*Skw*. With the CPI+VTF method, the lowest MI is observed with MTT and *CTTH* but no different than MTT-*Skw* and *CTTH-Skw* ($p>0.05$). *CTTH-Skw* shows highest MI and high variability with CPI+VTF.

Table 5.2: Mutual Information (MI) between hemodynamic parameters.

	CPI			CPI+VTF	
	CTTH	***Skw***		***CTTH***	***Skw***
MTT	0.96 ± 0.25	1.05 ± 0.28	**MTT**	0.92 ± 0.32	0.94 ± 0.33
CTTH		0.74 ± 0.54	***CTTH***		1.16 ± 1.52

5.3.2 Study II (ROI Study)

Using the CPI method with ROI analysis on the pre-CEA dataset, a mean MTT of 1.81 ± 0.25s was observed for normal tissue compared to 2.94 ± 1.53s for DWI-ring tissue and 5.58 ± 2.20s for DWI+ tissue, these values being lower ($p<0.05$) than the values calculated with the oSVD method (4.27±0.43s, 5.20±0.97s and 7.34±1.57s respectively). The differences in observed MTT among the three tissue types with CPI were found to be statistically significant ($p<0.05$).

Figure 5.5a shows the mean residue functions calculated with the CPI method showing the variations between normal tissue and tissue with hemodynamic disturbances. On visual assessment, the residue function observed in pre-surgery evaluation from the DWI-ring ROI consistently showed a slower decay compared to that observed in normal tissue; the residue function from the DWI+ tissue decayed even slower than the DWI-ring tissue. Figure 5.5b shows the corresponding transit time distribution for Normal, DWI-ring and DWI+ tissue pre-surgery; a larger contribution

from the higher transit times is seen in both the DWI-ring and the DWI+ tissue. Figure 5.5c, d shows that the variation in residue function shape and transit time distribution between the three tissue types decreased post-surgery. The hemodynamics in the DWI-ring and DWI+ tissue thus appeared to change towards the Normal tissue behaviour post-surgery. Similar changes in the residue function and the transit time distribution are observed with the CPI+VTF method, Figure 5.6. Note that the differences in residue function between Normal and DWI-ring during pre-surgery are smaller with CPI+VTF (Figure 5.6a) when compared to CPI method (Figure 5.5a), the same as was observed in Chapter 4 where the CPI method tended to show higher differences in ischemic and normal tissue because of dispersion effects that were corrected for in CPI+VTF.

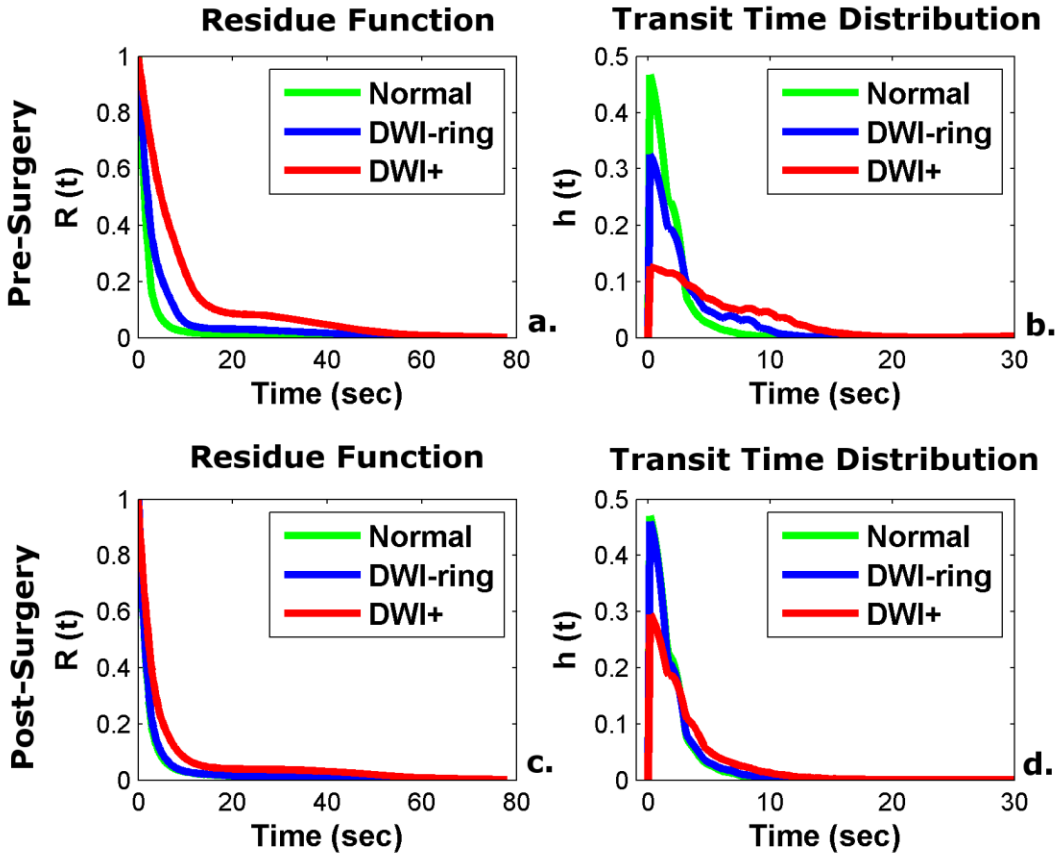

Figure 5.5: Mean residue function and distribution of transit times observed with CPI for Normal, DWI-ring and DWI+ tissue pre and post-surgery.

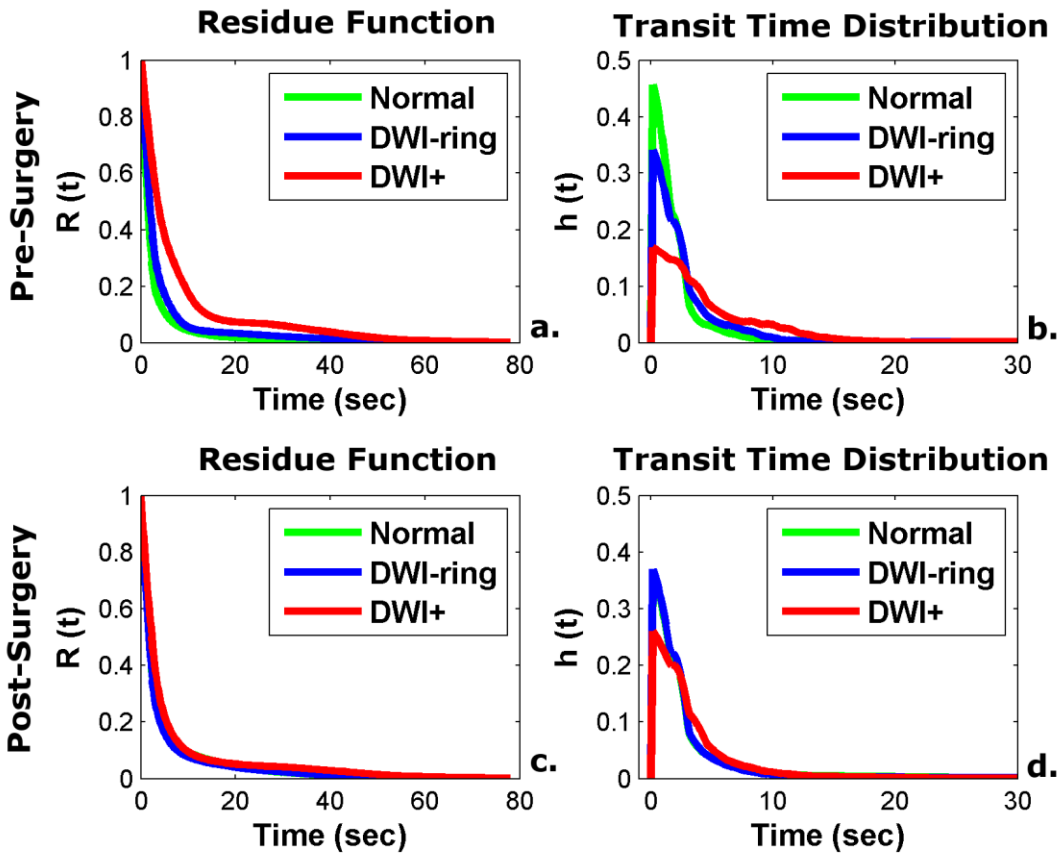

Figure 5.6: Mean residue function and distribution of transit times observed with CPI+VTF for Normal, DWI-ring and DWI+ tissue pre and post-surgery.

Figure 5.7 shows the box and whisker plot for MTT (top), *CTTH* (middle) and *Skw* (bottom) both pre- and post-surgery for the three tissue types using the CPI method. Figure 5.8 shows the corresponding values of MTT (top), *CTTH* (middle) and *Skw* (bottom) values observed with the CPI+VTF method. Pre-CEA MTT and *CTTH* consistently increased from Normal to DWI-ring and DWI+ tissue (MTT: Normal < DWI-ring < DWI+; *CTTH*: Normal < DWI-ring < DWI+), whereas *Skw* decreased from Normal to DWI-ring and further to DWI+ tissue type (*Skw*: Normal > DWI-ring > DWI+) with both the CPI and the CPI+VTF methods. For Normal tissue no significant change in MTT and *CTTH* was observed between pre- and post-CEA using the CPI method, however for DWI-ring and DWI+ tissue the hemodynamics appeared to change post-surgery as

observed with significant variations ($p<0.05$) in MTT and *CTTH*. With the CPI+VTF method, only *CTTH* showed significant changes in hemodynamics between pre- and post-CEA for both DWI-ring and DWI+ tissue. MTT, *CTTH* and *Skw* all showed significant variations ($p<0.05$) in values when comparing Normal, DWI-ring and DWI+ tissue in pre-CEA with both the CPI and the CPI+VTF method.

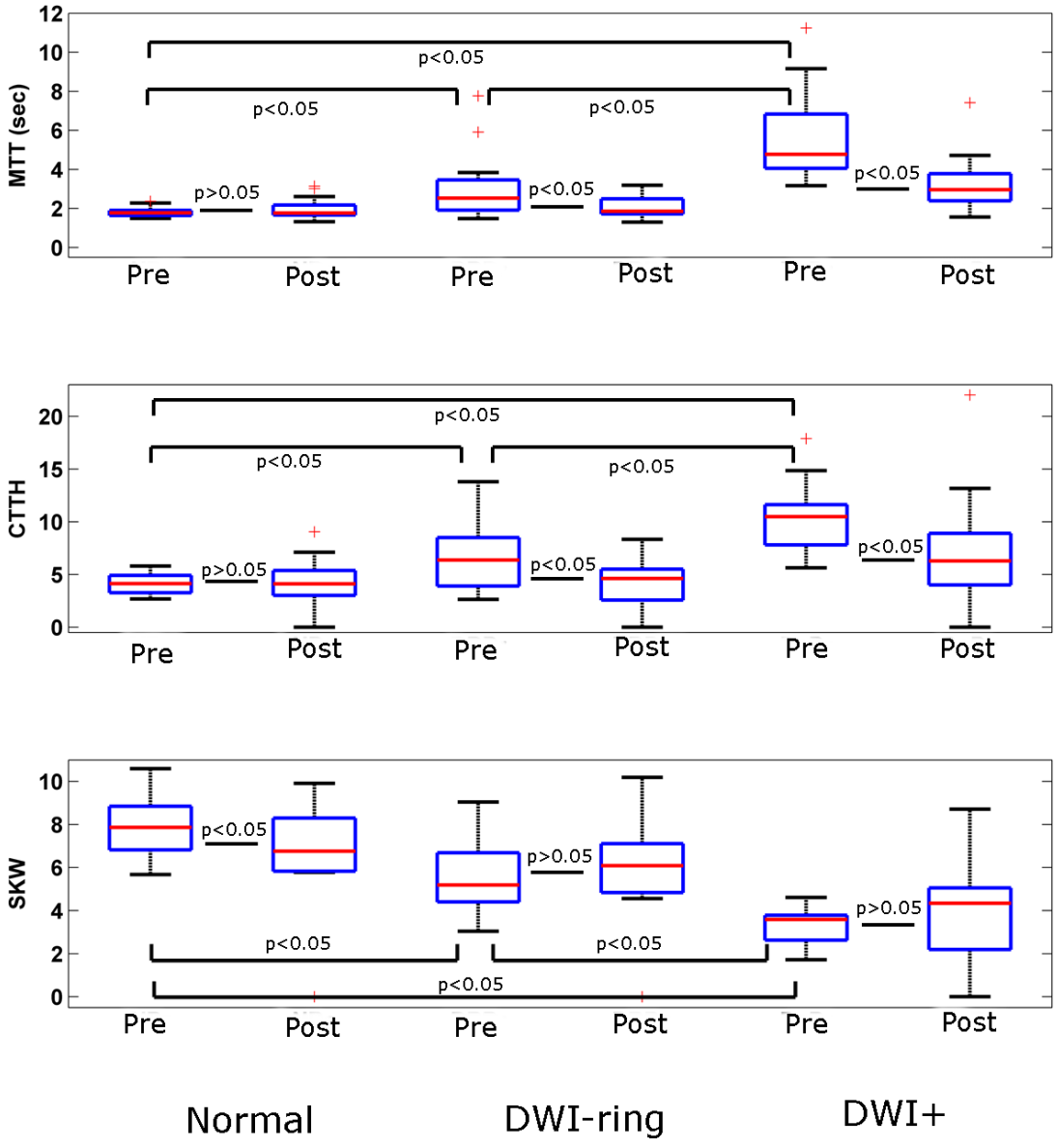

Figure 5.7: Box and whisker plot showing distributions of MTT (top), *CTTH* (middle) and *Skw* (bottom) for Normal, DWI-ring and DWI+ tissue types in pre-surgery and post-surgery perfusion analysis with CPI methods and comparisons for statistical significance.

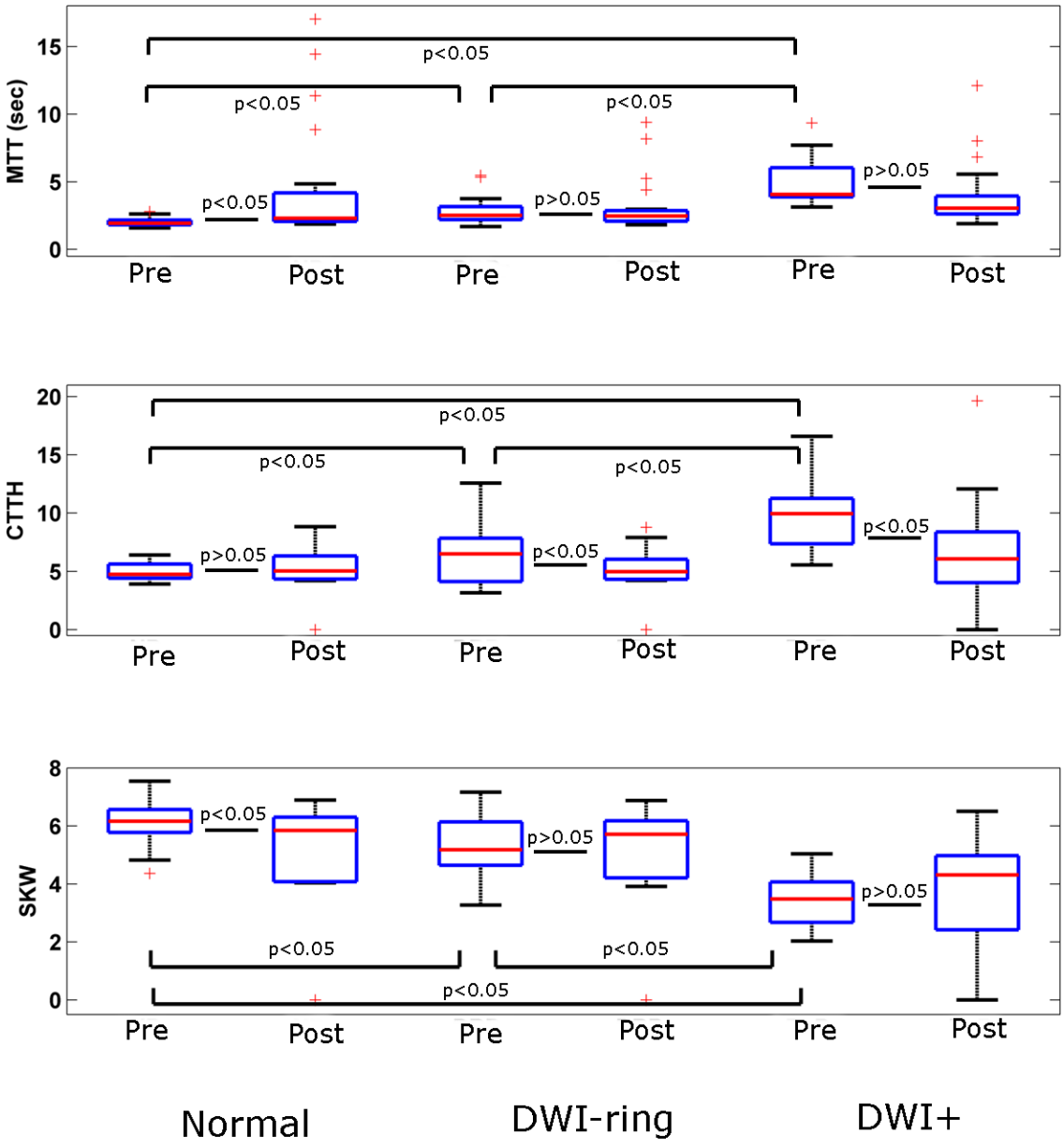

Figure 5.8: Box and whisker plot showing distributions of MTT (top), *CTTH* (middle) and *Skw* (bottom) for Normal, DWI-ring and DWI+ tissue types in pre-surgery and post-surgery perfusion analysis with CPI+VTF method, and comparisons for statistical significance.

Figure 5.9 shows the scatter plot for all paired combinations for MTT, *CTTH* and *Skw* for Normal, DWI-ring and DWI+ tissue obtained with both the CPI and the CPI+VTF method. A clear trend is observed in all three parameters with increases in MTT and CTTH and a decrease in *Skw*. The variability in *CTTH* and *Skw* also appears to increase with increased MTT. Figure 5.10 shows the

same results together with model predictions using a new hemodynamic model by Payne (Appendix I) for $CMRO_2$ levels in the range 40-100% of baseline. The new hemodynamic model characterizes a tissue capillary network of transit time distribution, $h(t)$, with a baseline $CMRO_2$ of 100%. The model represents an analytical solution that can provide hemodynamic parameter estimates for various $CMRO_2$ values. Normal tissue shows a tight cluster around a $CMRO_2$ level of 100%; the DWI-ring shows more variability but still appears to fall within a $CMRO_2$ range of 60-100%. DWI+ tissue shows the highest variability in the observed data, spanning values of $CMRO_2$ between 40-100%.

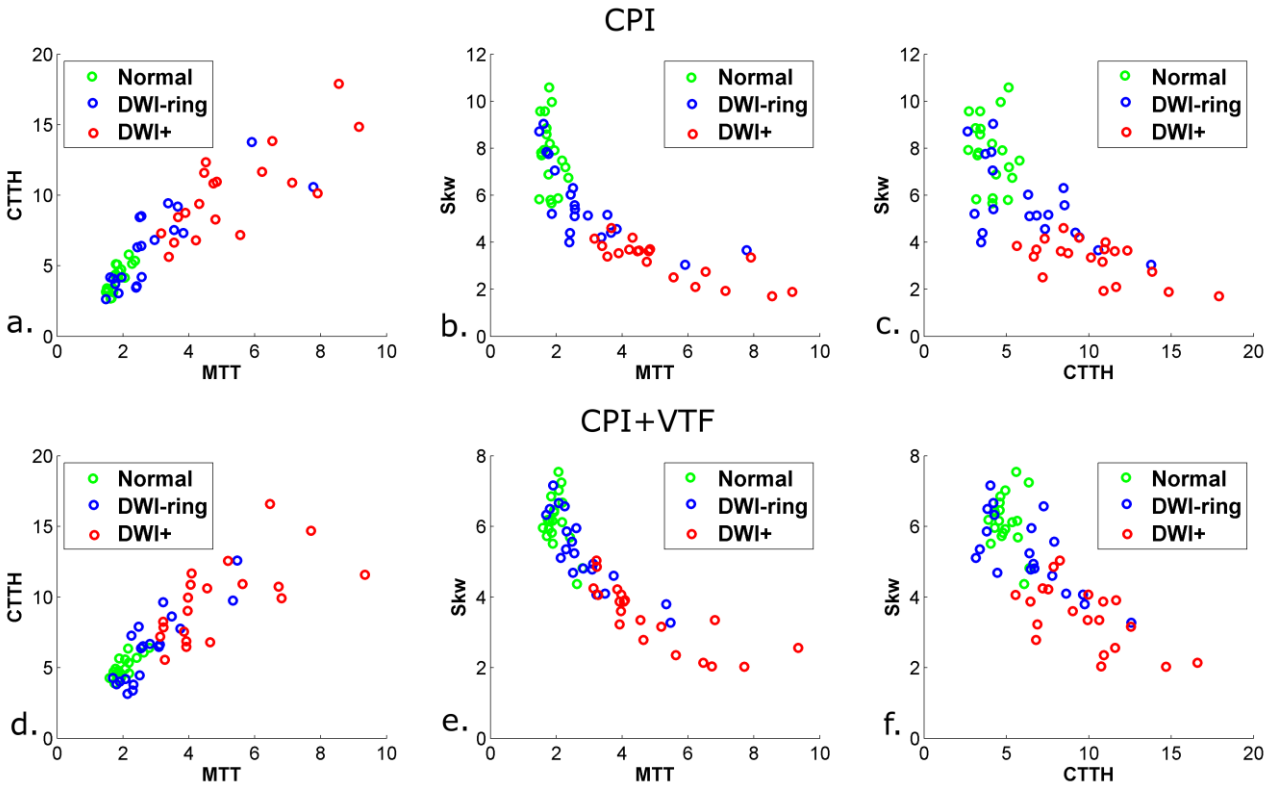

Figure 5.9: Scatter plot between: a, d) MTT and *CTTH*; b, e) MTT and *Skw*; c, f) *CTTH* and *Skw*; for Normal, DWI-ring and DWI+ tissue from five patients using CPI (a, b, c) and CPI+VTF (d, e, f) method.

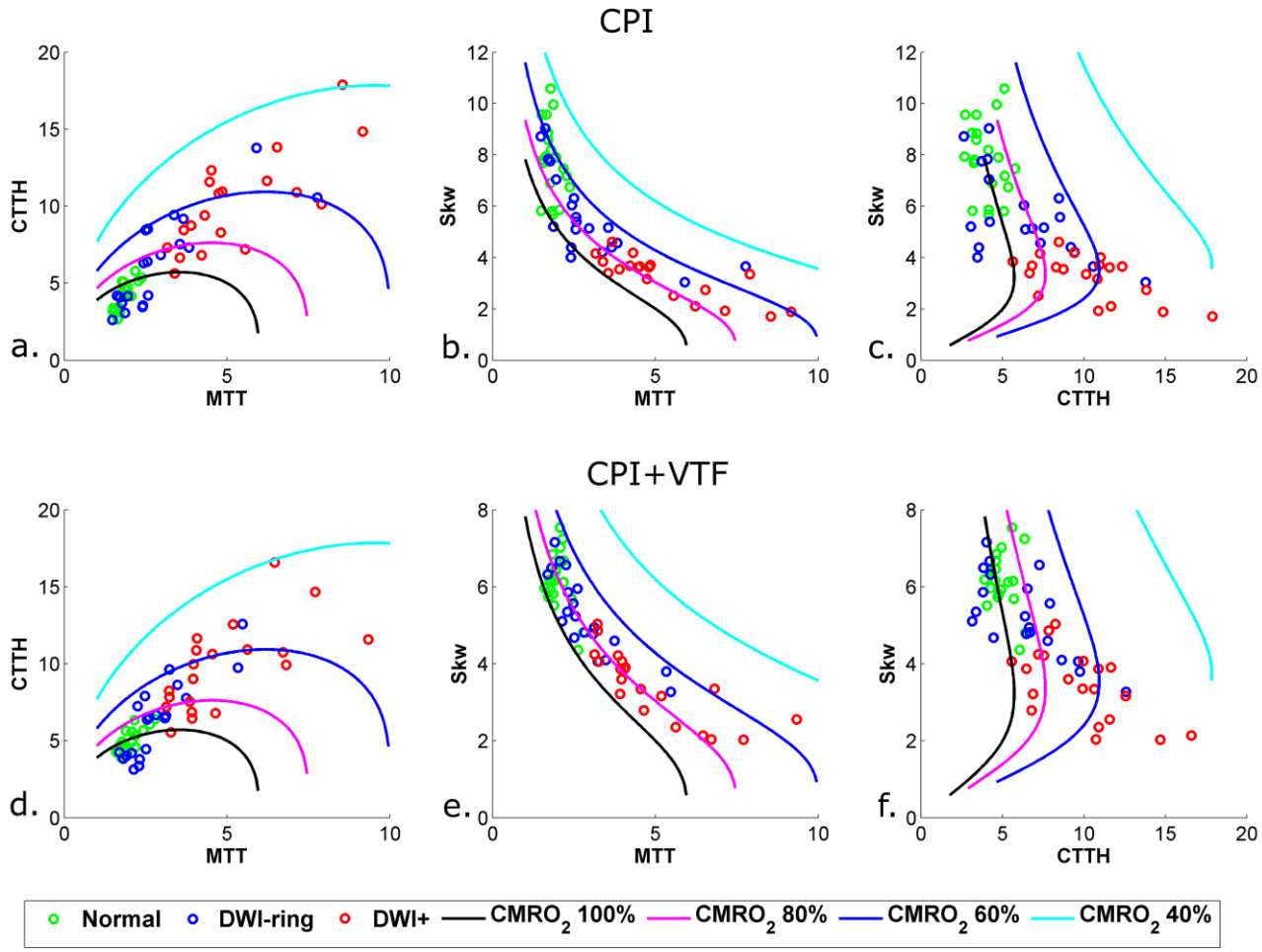

Figure 5.10: Scatter plot between a, d) MTT and *CTTH*, b, e) MTT and *Skw* and c, f) *CTTH* and *Skw* for Normal, DWI-ring and DWI+ tissue from five patients using CPI (a, b, c) and CPI+VTF (d, e, f) method and model prediction of capillary hemodynamics at $CMRO_2$ (40-100%) using hemodynamic model of Payne (Appendix I).

5.4 Discussion

Tissue hemodynamic information is encapsulated in the tissue residue function and transit time distribution; however, these have previously been very difficult to interpret precisely because of the non-physiological oscillations observed in the residue function as calculated with the most commonly used SVD based methods for perfusion analysis. CPI has been shown in Chapter 3 and Chapter 4 to be sensitive to the pathophysiological variations in residue function. In this chapter the novel CPI method and its dispersion variant were thus evaluated in a chronic atherosclerosis disease

patient cohort to investigate the significance of hemodynamic information from the DSC-MR imaging for clinical use.

The existence of an absolute perfusion threshold for tissue infarction has been continuously debated in the literature along with the possibility of a differential threshold for grey and white matter [123,124]. Since both the duration and severity of ischemia are of importance it would be expected that the thresholds are time dependent [121]. To perform a population study and to set a threshold for ischemic tissue, CBF and CBV values cannot easily be used as they are measured in a relative scale whereas MTT measurements could be more robust as they are measured in absolute units. MTT has been shown to exhibit a significant variation while comparing ischemic and healthy tissue [124].

The choice of deconvolution analysis method complicates this problem as each methodology is based on different fundamental assumptions for the underlying capillary hemodynamics. It has previously been reported that delay-sensitive deconvolution algorithms can overestimate the region of ischemic tissue compared to delay-insensitive methodologies [122]. For normal tissue a value of MTT of 1.81 ± 0.25s is observed with CPI and 2.02 ± 0.31s with CPI+VTF which is lower than the literature value of 3-4s [120,122–124]. This discrepancy could arise because of the differences in deconvolution method used. Most of the literature studies have used SVD based methods which are vulnerable to underestimation of CBF hence overestimation of MTT (by the central volume theorem). In simulation studies (Chapter 3 and Chapter 4) it has been shown that the SVD method could result in substantial overestimation of absolute MTT by a factor of approximately 1.6 where CPI achieves a better estimate. Normal literature value of 3-4s in that case would be realistically more close to 2-3s. Hence observing a lower value of MTT with CPI in normal tissue compared to literature is not surprising.

Smoothly decaying residue functions are observed with both the CPI and the CPI+VTF methods during clinical data analysis. Large differences in the shape of the residue function are observed between normal and ischemic tissue where the residue function from ischemic tissue shows a slower decay in the residue function. Tissue under conditions of hemodynamics stress might show a residue function shape that is in between those found for normal tissue and tissue with severe ischemia. As shown in Figure 5.5a and Figure 5.6a, the residue function in the DWI-ring is found to decay more slowly than in the Normal region but faster than in the DWI+ tissue. The hemodynamics in the DWI-ring might thus suggest tissue under ischemic stress as it has a larger contribution from the high transit times but not to the extent observed in the DWI+ tissue (Figure 5.5b and Figure 5.6b).

Since it might not be possible to visualize variations in the full residue function in a voxel-wise manner for the complete brain in clinical practice, hemodynamic summary parameters like MTT, *CTTH* and *Skw*, that characterize the transit time distribution are considered in this chapter to study spatial variations in hemodynamics in patients with atherosclerosis. Figure 5.1 and Figure 5.3 show the spatial maps of MTT, *CTTH* and *Skw* from two representative patients. In Figure 5.1 the patient shows reductions in MTT and *CTTH* with an increase in *Skw* after CEA, which suggests an increase in tissue perfusion after surgery, and a similar improvement is observed with the dispersion parameters, as shown in Figure 5.2. However, in some patients MTT and *CTTH* are found to increase and *Skw* to decrease post-CEA, which implies a worsening of capillary hemodynamics after CEA, as illustrated with a representative case in Figure 5.3. Post-CEA dispersion in general is expected to reduce, however in this patient the dispersion parameters do not show any significant reduction (Figure 5.4). This might be because of the postoperative complications of CEA. Carotid Endarterectomy is often associated with an increase in postoperative risk of embolism and cerebral ischemia as pieces of carotid plaque might get disrupted during the surgical intervention and travel

up the internal carotid artery to the brain, where they can block the circulation resulting in further ischemia [134–139]. It should also be noted that the datasets analyzed here are from an elderly patient cohort with bilateral carotid artery stenosis where only one of the severely affected arteries was surgically operated upon. The poor hemodynamics observed in these patients could also be a benign transient oligemia as post-CEA imaging was performed within 24 hours of surgery and it might be the case that hemodynamics take more time to return to normal in these patients. However, even in such a scenario the dispersion might be expected to improve which is not found to be the case here.

It has previously been suggested in rat models by Hudetz et al. [11] and Tomita et al. [12] that *CTTH* increases in proportion to MTT during ischemia and more recently a similar hypothesis has been proposed using a model for capillary hemodynamics by Jespersen et al. [9] and Ostergaard et al. [10]. An experimental investigation in humans has been performed in this thesis using the CPI method for perfusion MRI, where an increase in MTT has been shown to be associated with a proportionate increase in *CTTH* and decrease in *Skw* (Figure 5.9). Similar results have been observed independently by Payne using a physiological model of capillary hemodynamics (shown in Appendix I). The hemodynamic model by Payne shows that with the progression of ischemia (increase in MTT) tissue can sustain viable tissue oxygenation by altering hemodynamics through an increase in *CTTH* and a decrease in *Skw* of the transit time distribution in the capillary network. The empirical results observed with CPI and CPI+VTF method over Normal, DWI-ring and DWI+ tissue, as shown in Figure 5.10, appear to follow similar trends as with the model predictions by Payne. With an increase in MTT (Normal < DWI-ring < DWI+ tissue) the *CTTH* showed an increase and *Skw* showed a decrease in values. Comparing the *in vivo* results with model predictions, MTT vs. *CTTH* and *CTTH* vs. *Skw* showed a larger variation in the DWI+ tissue, falling within $CMRO_2$ band of 40-100%. However MTT vs. *Skw* showed a clearer trend within

$CMRO_2$ band of 60-100%. These discrepancies might be observed because of the model assumptions; the hemodynamic model by Payne assumes that the normal tissue at the baseline MTT of 2s has 100% $CMRO_2$ and that the transit times though the underlying capillary network can be modeled with a gamma probability distribution. The model also assumes that cerebral blood volume remains constant with variations in tissue MTT. These assumptions might not represent a realistic scenario for pathophysiological variations in hemodynamics. Further analysis would be helpful to understand physiological tissue oxygenation and capillary hemodynamics in greater detail.

MI was calculated for the estimated hemodynamic parameters to find the two most distinct parameters with the least amount of shared hemodynamic information. Parameters with the least shared information are expected to complement each other. MTT and *CTTH* have the lowest MI as measured with CPI+VTF, which is not surprising, as to characterize the shape for any probability distribution function (transit time distribution in this case) the mean and standard deviation are clearly two distinct parameters. The statistical significant differences however could not be shown probably because of the patient cohort evaluated this study. It is worthy of note that the study cohort is based on chronic cerebral ischemia where each patient suffered slow and progressive arterial stenosis over a long period of time (of order years) and for each patient hemodynamic stability might have been achieved influenced by other factors based an each individual's health status, i.e. age, associated hypertension, diabetes mellitus and cardiovascular disorders [40,140–142]. It would be very valuable to perform similar analysis and to evaluate the clinical benefits of calculating *CTTH* and *Skw* on a cohort of acute cerebral ischemia where hemodynamics are actively changing.

It is consistently observed that the measured *in-vivo* residue function has both a fast and a slow decay component, implying faster and slower flowing pathways in the tissue capillary network. This is consistent with the literature [8–10] where hemodynamics are actively controlled to

maintain sufficient blood and have oxygen supply to the tissue. There could be dynamic mechanisms in the capillary network that maintain normal tissue oxygenation even in the case of ischemic stress. The capillary hemodynamics might adjust for the blood flow hemodynamics up to a threshold after which the damage is inevitable [143], the concept is however poorly understood. In this study it is shown that the residue function in tissue with hemodynamic stress (DWI-ring) can revert to normal, as observed in imaging data post-CEA (Figure 5.5 and Figure 5.6). This still needs, however, to be validated in a larger dataset of acute stroke with a full comparison with gold standard diagnostic imaging, such as PET. The variations found in residue function shape and transit time distribution might open new avenues for quantitative diagnostic and prognostic monitoring of ischemia and stroke facilitating timely intervention and affecting the therapeutic outcomes.

In this study of *in vivo* residue function analysis with a non-parametric CPI method, it is found that the residue function has a more complex shape than either the expected exponential or box shapes. The residue function is revealed to have a fast and a slow decay component. The tail of the residue function behaves differently in ischemic tissue (decaying more slowly) compared to the initially fast decaying residue function. The two components of the residue function observed in *in vivo* data suggest that the mono-exponential model for the residue function or the box shaped residue function might not be the best choices to describe real tissue hemodynamics.

It should finally be noted that cerebral ischemia is a dynamic process. Studies have shown a wide variation in functional flow thresholds for different brain regions indicating possibly a differential regional vulnerability [144]. Perfusion imaging plays an important role in management of cerebral ischemia, thus clinical decision making cannot be based on the ambiguous threshold values available at present [121]. The residue function captures the dynamic behaviour of tissue

hemodynamics and seems to serve as potentially a better criterion for assessment of ischemia than a static threshold on snapshot parametric maps of CBF or MTT. The Control Point Interpolation method can thus serve as a useful tool to quantify cerebral hemodynamics in patients with vascular abnormalities. This could help to facilitate a better diagnostic, prognostic and therapeutic outcome for patients with vascular abnormalities.

5.5 Conclusion

In this chapter CPI and its dispersion variant were evaluated to investigate residue function behaviour in a larger clinical cohort of patients with atherosclerosis. The perfusion analysis of *in vivo* data using both the CPI and the CPI+VTF method revealed an increase in capillary heterogeneity and decrease in Skewness of the transit time distribution in tissue with hemodynamic stress. A clear trend observed in hemodynamic parameters to maintain the tissue oxygenation level at above 40% of baseline implies that there might be active mechanisms in the capillary bed to maintain tissue viability under conditions of hemodynamic stress. The research in this chapter clearly shows that it is now possible to quantify cerebral hemodynamics beyond CBF and MTT using the newly proposed control point interpolation method.

Chapter 6
Conclusion and Future Work

6.1 Conclusion

Cerebrovascular ischemia is one of the most challenging healthcare problems in an ageing population. Cerebral ischemia can lead to stroke which in turn can leave the patient with a permanent physical disability or can even be life threatening. Perfusion MRI is commonly used for diagnostic and prognostic monitoring of cerebral ischemia to help clinicians to assess cerebral perfusion for planning further medical management. Perfusion analysis can be performed by a model-based approach which is often discouraged in research studies as the tissue microvasculature response cannot be known *a priori*. The problem can be solved by performing a non-parametric approach without *a priori* knowledge of tissue residue function. This approach is referred to as model-free deconvolution, where the tissue residue function is determined experimentally. The process of deconvolution involved is an ill-posed inverse problem.

The ill-posed nature of the problem requires a non-parametric deconvolution method to perform reliably in all pathophysiological situations. The SVD based method and Vascular Model are commonly used in research (and clinical settings) but each has their own limitations in estimating the shape of residue function accurately. SVD based methods introduce non-physiological oscillations during deconvolution, while the vascular model is strictly a model-based solution as a gamma distribution is assumed to model the transit times, permitting only a restricted family of shapes for the residue function.

A new deconvolution method, Control Point Interpolation, proposed in Chapter 3 of this thesis, incorporates physiological hemodynamic information in the perfusion analysis methodology. The CPI method represents the residue function by a number of control points, each having two degrees of freedom (amplitude and time). A complete estimate of the shape of the residue function is then generated by using a piecewise cubic spline interpolation. The method has been shown in simulations to be able to estimate CBF with greater accuracy, than existing methods giving a regression coefficient between true and estimated CBF values of 0.96 compared to 0.83 for VM and 0.71 for oSVD. The CPI method also showed abilities to accurately estimate the residue function over a wide range of simulated conditions. The CPI method has also been tested on clinical data where a marked difference was observed between the residue functions of normal brain tissue and infarcted tissue. These variations in residue function are most likely hemodynamic variations in tissue but could also arise because of associated bolus dispersion.

In Chapter 4 the CPI method was adjusted to compensate for bolus dispersion using two approaches: 1) a Vascular Transport Function (VTF) was implemented in conjunction with CPI, termed the CPI+VTF method; and 2) a completely model-free approach was implemented in CPI called CPI_0 where the first control point was fixed to zero. Being non-parametric in its approach, CPI_0 cannot separate the residue function from effects of dispersion. However, with CPI+VTF it is possible to investigate variations in residue function as macrovascular dispersion is modeled in the VTF component. CPI+VTF results confirmed the variations in the residue function between normal and infarcted tissue, as observed with the CPI method in Chapter 3. It is of further interest to understand the variations in tissue hemodynamics in pathology over a larger clinical data set using these methods.

In Chapter 5 a retrospective analysis over a clinical dataset was performed for seventeen patients with atherosclerotic disease undergoing carotid endarterectomy surgery and two healthy control subjects. Perfusion imaging data were acquired for all the patients both pre- and post-surgical intervention. Perfusion analysis was performed with both the CPI method and its dispersion corrected variant methods. A ROI based analysis was used to compare the changes in hemodynamics pre- and post-surgery. The observed non-parametric residue function was converted to a transit time distribution. Standard deviation (*CTTH*) and Skewness (*Skw*) of the distribution were used as the summary parameters to investigate the clinical significance of changes in transit time distribution in pathology. For patients with cerebral ischemia *CTTH* increased in tissue under hemodynamic stress which returned to 'normal' contralateral values after CEA surgical procedure. In contrast *Skw* decreased in the tissue under hemodynamic stress, returning to 'normal' contralateral values after CEA surgery. However, some of the patients showed either poor or no change in hemodynamics even after CEA surgery, this might be a transient effect or due to surgical complications.

In conclusion, a non-parametric deconvolution method has been developed in the form of the CPI method. The method has been corrected to accommodate both bolus delay and dispersion. The method has been shown to provide accurate CBF estimation with simulations both in the presence and the absence of dispersion. It has been demonstrated though clinical investigation that the CPI method is able to show changes in the residue function shape and transit time distribution under pathophysiological conditions. An attempt has also been made to summarize the non-parametric residue function and transit time distribution by parameters including *R10*, *CTTH* and *Skw* through a clinical study. The clinical significance of these parameters in the assessment of stroke would require a larger clinical trial in patients with acute stroke. The CPI method could thus serve as a viable means to examine cerebral hemodynamics using perfusion magnetic resonance imaging.

6.2 Future Work

6.2.1 CPI for Brain Tumour Perfusion Imaging

A brain tumour is classified as either a primary cancer originating in the brain cell or a secondary cancer originating in an organ other than the brain but metastasizing to the brain; 25% of all body cancers spread to the brain leading to a secondary brain tumour [145]. In the UK alone 16,000 people are diagnosed with a brain tumour each year [145]. A brain tumour is also the biggest cause of tumour related death of children in UK and more people under 40 die of a brain tumour than from any other cancer [145]. Every year the incidence of brain tumours is increases by 4% [145]. These statistics represent a large patient burden on healthcare and research efforts are thus focused on the early detection and treatment of brain tumours. Perfusion MRI of the brain has become a standard clinical diagnostic technique for assessment of regional brain perfusion. DSC-MRI and Arterial Spin Labeling are currently both being used for perfusion analysis in research, where the former is currently also in widespread clinical practice because of its better signal to noise ratio. Perfusion imaging of brain tumours provides valuable information with respect to diagnosis, therapy planning and subsequent prognostic monitoring [146].

Perfusion analysis in brain tumours is significantly different from ischemic brain tissue as the blood brain barrier is often ruptured in a brain tumour leading to extravasation of contrast into the extravascular extracellular space. Thus the single compartment model assumption does not hold true in the perfusion assessment of brain tumours. The area under the CTC no longer represents the CBV, which is the fundamental assumption for perfusion analysis in ischemic brain tissue. In a brain tumour the Gadolinium contrast resides in for a longer time (more than the time of image acquisition). The residue function in such cases may not return to baseline during the DSC image acquisition.

Multi-compartmental models are available to perform perfusion analysis during contrast leakage [61] using a model-based analysis strategy. CPI could be a non-parametric alternative approach to the analysis of brain tumour perfusion. In *T2** perfusion imaging susceptibility effects from Gadolinium cause the MR signal to drop and the CTC to increase during the transit of contrast through the tissue capillary network. When the contrast leaks because of the blood brain barrier break down in a brain tumour there is a *T1* dominance of the MR signal which causes the signal to increase (above the baseline signal). There are models which correct for *T1* dominance and contrast extravasation effects in DSC-MRI [60,61,147]. Hence the CPI method would need to be adjusted for these effects before it could be used for the hemodynamic assessment of brain tumours.

It could be clinically useful to examine the behaviour of the residue function with the CPI method in the case of brain tumours. Tumour tissue growth is associated with neoangiogenesis (formation of new blood vessels in the tumour) which is also a marker of tumour aggressiveness [148,149]. Angiogenesis causes the hemodynamics in the tumour to vary. With the CPI method the variations in tissue hemodynamics can be studied, thus it might be possible to use this additional hemodynamic information as a measure of tumour's aggressiveness and further use for tumour grading. This could also be used in monitoring of patients on chemo-radiotherapy, where prognosis of the tumour could be measured in term of changes in hemodynamics towards normal tissue. One of the other uses of the CPI technique in brain tumour assessment could be differentiation of tumour recurrence from radiation necrosis, where tumour recurrence would be associated with actively changing tissue hemodynamics.

6.2.2 CPI for Cardiac Perfusion Imaging

Heart attack and stroke are two of the most devastating diseases in an aging population, in combination being referred to as vascular diseases. Statistics published by the British Heart

Foundation in 2009 showed that around one third of all deaths in the UK were due to vascular diseases; over 82,000 deaths being caused by ischemic heart disease alone [150]. Vascular disease management yearly costs £8.49 billion to the NHS (12.1% of the total NHS budget) [151]. A lot of research efforts are thus focused on early diagnosis and the initiation of timely treatment of ischemic heart disease (IHD). Significant advances have been made over the last 40 years, in particular in Magnetic Resonance Imaging. MRI perfusion techniques play an important role in IHD assessment to differentiate healthy from ischemic tissue. Although Positron Emission Tomography is considered to be the gold standard, the associated radiation risk, cost and unavailability in most clinical centres have limited its wider usage. Therefore, reliable, quantitative and robust MR perfusion imaging could yield a significant potential beneficial impact to a large population by improving the quality of diagnostic patient care.

A heart attack is the result of a long term progressive obstruction in the blood vessels in the heart. This obstruction is caused by deposition, for example cholesterol, in the vessel wall that slowly grows to completely block the lumen, leading to ischemia and a heart attack. During the course of this progressive obstruction the blood flow patterns in the heart alter in order to maintain a functionally viable state. With the use of the new CPI technique, it might be possible to measure these changes in microvascular hemodynamics, by quantifying variations in the residue function and transit time distribution that could help in early diagnosis of IHD. The research objective here would be to develop a new analysis protocol for vascular assessment of the heart that would help to diagnose subjects with vulnerability to heart attack and to facilitate an early diagnosis and prognostic monitoring of a heart attack.

In current clinical settings, cardiac perfusion analysis typically attempts to estimate surrogate markers like signal upslope and time-to-peak. Additionally, such analysis performs the perfusion

estimation in a segmented manner, where signals are averaged over a segment of the heart wall. Performing the analysis over segments provides valuable robust summary results, but it loses vital information about regional variations in perfusion. A voxel-wise analysis might be an appropriate alternative [152]. This additional perfusion information would be highly beneficial in clinical practice because it could provide a clear spatial demarcation of normal and under perfused tissue and hence a better diagnosis of IHD.

In order to sustain functionally viable tissue perfusion levels, ischemic tissue attempts to regulate microvascular flow through changes in hemodynamics. It might be possible to capture these early changes before a patient develops a heart attack; thus facilitating an early diagnosis and timely intervention. Altered hemodynamics might also provide information regarding the vulnerability of a patient to a recurrent heart attack. A microvascular assessment with a stress-test over a chronic cardiac ischemic cohort could be performed to diagnose tissue with hemodynamic stress and to initiate precautionary measures for those patients. After understanding the role of hemodynamic variations in early diagnosis, the next extension could be to investigate hemodynamic information for prognostic monitoring. Post-surgery (bypass grafting) the new artery starts to supply blood to the ischemic tissue, leading to more normal microvascular flow patterns over time. The information about microvascular flow patterns could be used as a measure of recovery. Such an improved means to measure prognosis might help to reduce post-surgical hospital stay time.

In future it would be also useful to investigate the clinical benefits of voxel-wise analysis and variations in microvascular flow patterns for early diagnosis of ischemic heart disease. Together with the Oxford Centre for Clinical Magnetic Resonance Research (OCMR), in the John Radcliffe Hospital a feasibility study over a single dataset has already been performed (the *in vivo* data was provided by Dr. Theo Karamitsos, OCMR, University of Oxford, UK); Figure 6.1 shows the

preliminary results for this subject. However, modeling cardiac hemodynamics for perfusion quantification comes with its own unique challenges including cardiac motion artifacts and high permeability of vessels. Those need to be addressed if the CPI method is to be used for cardiac perfusion assessment.

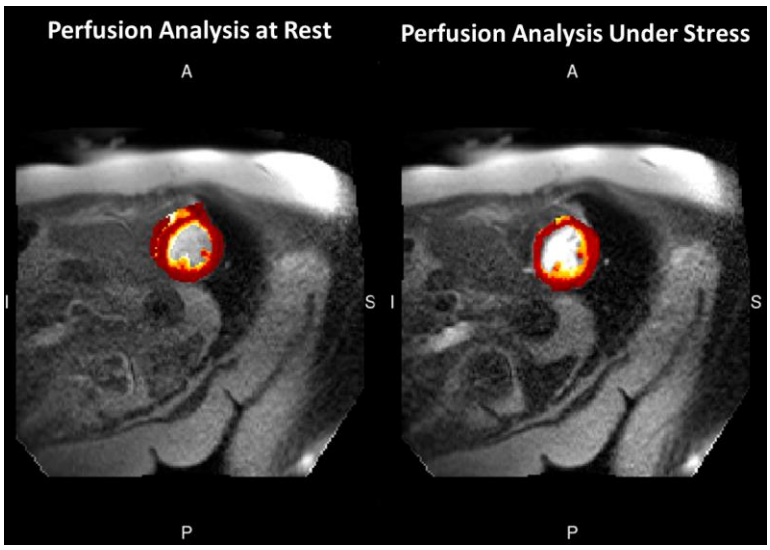

Figure 6.1: Voxel-wise perfusion quantification over the left ventricular wall for a healthy subject at rest and under stress condition.

6.2.3 CPI for Arterial Spin Labeling Imaging

Arterial Spin Labeling (ASL) is an MRI technique for measuring perfusion at the brain tissue level using a noninvasive methodology. Arterial blood water is used as an endogenous contrast for perfusion imaging in conjunction with MRI by magnetically labeling of water in blood proximal to the tissue of interest [153]. The tissue of interest is first imaged without labeling followed by labeling of the inflowing blood and imaging the tissue of interest again. The subtraction of the two images gives a measure of tissue perfusion. As compared to DSC-MRI, ASL has poor *SNR* for perfusion quantification but the benefit is that it does not require the administration of exogenous contrast, which is contraindicated in renal insufficiency, and ASL also provides a direct quantification of absolute CBF. The utility of ASL in characterizing perfusion in both acute stroke

[154] and chronic cerebrovascular disease [155] has already been demonstrated. The ability to quantify CBF noninvasively would be very useful for monitoring disease progression and therapy in patients with cerebral ischemia.

An analysis model for ASL perfusion has already been proposed by Buxton et al. [156] and been widely used so far. The model is represented, similar to DSC-MRI model, as a convolution of an arterial input function with a tissue residue function in addition to a *T1* recovery function for the labeled water. Pertersen et al. [157,158] used the model-free oSVD deconvolution method [18] for analysis of the ASL signal times series, which is susceptible to oscillations and underestimation of CBF. Motivated to achieve a more accurate CBF by characterizing a smooth residue function, the NSR method, which has already been proposed for DSC-MRI [24], has also been used in ASL perfusion quantification [107]. The limitations of both oSVD and NSR as discussed in Chapter 2 still hold for its use in ASL imaging.

It would thus be useful to explore perfusion quantification using the CPI method in ASL and to see if residue function analysis using the CPI method can provide additional information for tissue hemodynamics. The residue function in ASL imaging is not identical to the one in DSC-MRI; unlike DSC-MRI, the endogenous contrast (labeled water) in ASL is diffusible and free to exchange between blood and tissue. Thus the residue function has the microvascular hemodynamic information alongside information about water exchange between the intravascular and extravascular compartments. The CPI method in its current implementation could be used for ASL perfusion quantification as a non-parametric approach, thus improving the accuracy in CBF estimation. However, to study residue function variations the CPI method might need to be adjusted for diffusion of water molecules across the vessel wall by implementing it as a part of two compartment model. It is also to be noted that, the endogenously labeled water continuously decays

with the *T1* relaxivity of the blood water from the time of labeling onwards. This *T1* decay contributes a major proportion to the residue function. The fewer number of sample points in the ASL time series might also limit the extraction of hemodynamic information from the microvascular residue function.

The CPI method thus provide means to study capillary hemodynamics which might be helpful in understanding hemodynamic variations during pathophysiological progression of brain tumours, diagnosis and management of patients with cardiac ischemia and for prognostic monitoring of patients with ischemic heart disease after surgical intervention. CPI might also be useful in perfusion analysis with ASL in patients with cerebral ischemia and stroke. A wide range of clinical application can thus be explored with the newly proposed control point interpolation method in patients with vascular diseases.

References

1. Organization, W. H. *Global health risks-Mortality and burden of disease attributable to selected major risks*; 2009.

2. Heart Foundation, B. *Stroke Statistics*; 2009.

3. Heart Foundation, B. *Coronary Heart Disease Statistics*; 2009.

4. Law, M.; Som, P. M.; Naidich, T. P. *Problem Solving in Neuroradiology*; 1st ed.; Elsevier Saunders: Philadelphia, 2011; p. 656.

5. Kane, I.; Sandercock, P.; Wardlaw, J. Magnetic resonance perfusion diffusion mismatch and thrombolysis in acute ischaemic stroke: a systematic review of the evidence to date. *Journal of neurology, neurosurgery, and psychiatry* **2007**, *78*, 485–91.

6. Østergaard, L. Principles of cerebral perfusion imaging by bolus tracking. *Journal of magnetic resonance imaging: JMRI* **2005**, *22*, 710–7.

7. Cassot, F.; Lauwers, F.; Fouard, C.; Prohaska, S.; Lauwers-Cances, V. A novel three-dimensional computer-assisted method for a quantitative study of microvascular networks of the human cerebral cortex. *Microcirculation* **2006**, *13*, 1–18.

8. Østergaard, L.; Chesler, D. A.; Weisskoff, R. M.; Sorensen, A. G.; Rosen, B. R. Modeling cerebral blood flow and flow heterogeneity from magnetic resonance residue data. *Journal of Cerebral Blood Flow and Metabolism* **1999**, *19*, 690–9.

9. Jespersen, S. N.; Østergaard, L. The roles of cerebral blood flow , capillary transit time heterogeneity , and oxygen tension in brain oxygenation and metabolism. *Journal of Cerebral Blood Flow & Metabolism* **2012**, 264–277.

10. Ostergaard, L.; Jespersen, S. N.; Mouridsen, K.; Mikkelsen, I. K.; Jonsdottír, K. Ý.; Tietze, A.; Blicher, J. U.; Aamand, R.; Hjort, N.; Iversen, N. K.; Cai, C.; Hougaard, K. D.; Simonsen, C. Z.; Von Weitzel-Mudersbach, P.; Modrau, B.; Nagenthiraja, K.; Riisgaard Ribe, L.; Hansen, M. B.; Bekke, S. L.; Dahlman, M. G.; Puig, J.; Pedraza, S.; Serena, J.; Cho, T.-H.; Siemonsen, S.; Thomalla, G.; Fiehler, J.; Nighoghossian, N.; Andersen, G. The role of the cerebral capillaries in acute ischemic stroke: the extended penumbra model. *Journal of cerebral blood flow and metabolism: official journal of the International Society of Cerebral Blood Flow and Metabolism* **2013**, *33*, 635–48.

11. Hudetz, A. G.; Fehér, G.; Weigle, C. G.; Knuese, D. E.; Kampine, J. P. Video microscopy of cerebrocortical capillary flow: response to hypotension and intracranial hypertension. *The American journal of physiology* **1995**, *268*, H2202–10.

12. Tomita, Y.; Tomita, M.; Schiszler, I.; Amano, T.; Tanahashi, N.; Kobari, M.; Takeda, H.; Ohtomo, M.; Fukuuchi, Y. Moment analysis of microflow histogram in focal ischemic lesion to evaluate microvascular derangement after small pial arterial occlusion in rats. *Journal of cerebral*

blood flow and metabolism: official journal of the International Society of Cerebral Blood Flow and Metabolism **2002**, *22*, 663–9.

13. Tatlisumak, T. Is CT or MRI the Method of Choice for Imaging Patients With Acute Stroke? Why Should Men Divide if Fate Has United? *Stroke* **2002**, *33*, 2144–2145.

14. Chalela, J. A.; Kidwell, C. S.; Nentwich, L. M.; Luby, M.; Butman, J. A.; Demchuk, A. M.; Hill, M. D.; Patronas, N.; Latour, L.; Warach, S. Magnetic resonance imaging and computed tomography in emergency assessment of patients with suspected acute stroke: a prospective comparison. *Lancet* **2007**, *369*, 293–8.

15. Jacquez, J. *Compartmental analysis in biology and medicine: kinetics of distribution of tracer-labeled materials*; Elsevier: Amsterdam, 1972.

16. Rempp, K. A.; Brix, G.; Wenz, F.; Becker, C. R.; Gückel, F.; Lorenz, W. J. Quantification of regional cerebral blood flow and volume with dynamic susceptibility contrast-enhanced MR imaging. *Radiology* **1994**, *193*, 637–41.

17. Østergaard, L.; Weisskoff, R. M.; Chesler, D. A.; Gyldensted, C.; Rosen, B. R. High resolution measurement of cerebral blood flow using intravascular tracer bolus passages. Part I: Mathematical approach and statistical analysis. *Magnetic Resonance in Medicine* **1996**, *36*, 715–25.

18. Wu, O.; Østergaard, L.; Weisskoff, R. M.; Benner, T.; Rosen, B. R.; Sorensen, A. G. Tracer arrival timing-insensitive technique for estimating flow in MR perfusion-weighted imaging using singular value decomposition with a block-circulant deconvolution matrix. *Magnetic Resonance in Medicine* **2003**, *50*, 164–74.

19. Vonken, E. P.; Beekman, F. J.; Bakker, C. J.; Viergever, M. A. Maximum likelihood estimation of cerebral blood flow in dynamic susceptibility contrast MRI. *Magnetic Resonance in Medicine* **1999**, *41*, 343–50.

20. Andersen, I. K.; Szymkowiak, A.; Rasmussen, C. E.; Hanson, L. G.; Marstrand, J. R.; Larsson, H. B. W.; Hansen, L. K. Perfusion quantification using Gaussian process deconvolution. *Magnetic Resonance in Medicine* **2002**, *48*, 351–61.

21. Jerosch-Herold, M.; Wilke, N.; Stillman, a E. Magnetic resonance quantification of the myocardial perfusion reserve with a Fermi function model for constrained deconvolution. *Medical physics* **1998**, *25*, 73–84.

22. Calamante, F.; Gadian, D. G.; Connelly, A. Quantification of bolus-tracking MRI: Improved characterization of the tissue residue function using Tikhonov regularization. *Magnetic Resonance in Medicine* **2003**, *50*, 1237–47.

23. Mouridsen, K.; Friston, K.; Hjort, N.; Gyldensted, L.; Østergaard, L.; Kiebel, S. Bayesian estimation of cerebral perfusion using a physiological model of microvasculature. *NeuroImage* **2006**, *33*, 570–9.

24. Zanderigo, F.; Bertoldo, A.; Pillonetto, G.; Cobelli Ast, C. Nonlinear stochastic regularization to characterize tissue residue function in bolus-tracking MRI: assessment and comparison with SVD, block-circulant SVD, and Tikhonov. *IEEE transactions on bio-medical engineering* **2009**, *56*, 1287–97.

25. Gobbel, G. T.; Fike, J. R. A deconvolution method for evaluating indicator-dilution curves. *Physics in Medicine and Biology* **1994**, *39*, 1833–54.

26. Bjørnerud, A.; Emblem, K. E. A fully automated method for quantitative cerebral hemodynamic analysis using DSC-MRI. *Journal of cerebral blood flow and metabolism: official journal of the International Society of Cerebral Blood Flow and Metabolism* **2010**, *30*, 1066–78.

27. Østergaard, L.; Sorensen, A. G.; Kwong, K. K.; Weisskoff, R. M.; Gyldensted, C.; Rosen, B. R. High resolution measurement of cerebral blood flow using intravascular tracer bolus passages. Part II: Experimental comparison and preliminary results. *Magnetic Resonance in Medicine* **1996**, *36*, 726–36.

28. Iida, H.; Kanno, I.; Miura, S.; Murakami, M.; Takahashi, K.; Uemura, K. Error analysis of a quantitative cerebral blood flow measurement using H2(15)O autoradiography and positron emission tomography, with respect to the dispersion of the input function. *Journal of cerebral blood flow and metabolism: official journal of the International Society of Cerebral Blood Flow and Metabolism* **1986**, *6*, 536–45.

29. Calamante, F.; Gadian, D. G.; Connelly, A. Delay and dispersion effects in dynamic susceptibility contrast MRI: simulations using singular value decomposition. *Magnetic Resonance in Medicine* **2000**, *44*, 466–73.

30. Calamante, F.; Willats, L.; Gadian, D. G.; Connelly, A. Bolus delay and dispersion in perfusion MRI: implications for tissue predictor models in stroke. *Magnetic resonance in medicine: official journal of the Society of Magnetic Resonance in Medicine / Society of Magnetic Resonance in Medicine* **2006**, *55*, 1180–5.

31. Strong, K.; Mathers, C.; Bonita, R. Preventing stroke: saving lives around the world. *Lancet neurology* **2007**, *6*, 182–7.

32. Di Carlo, A. Human and economic burden of stroke. *Age and ageing* **2009**, *38*, 4–5.

33. Cost of Brain Disorders in Europe fact sheet http://www.europeanbraincouncil.org/projects/CDBE.asp.

34. Hendelman, W. J. *Atlas of Functional Neuroanatomy*; Second.; CRC Press, Taylor & Francis Group: Boca Raton, FL, 2006; Vol. 6.

35. The Radiology Assistant : Brain Ischemia - Vascular territories http://www.radiologyassistant.nl/en/p484b8328cb6b2/brain-ischemia-vascular-territories.html (accessed Jul 13, 2013).

36. File:Circle of Willis en.svg - Wikipedia, the free encyclopedia http://en.wikipedia.org/wiki/File:Circle_of_Willis_en.svg (accessed Jul 13, 2013).

37. StrokeCenter Pathogenesis and Pathophysiology http://www.strokecenter.org/education/ais_pathogenesis/22_ischemic_penumbra.htm.

38. Astrup, J.; Siesjö, B. K.; Symon, L. Thresholds in cerebral ischemia - the ischemic penumbra. *Stroke* **1981**, *12*, 723–5.

39. Wirestam, R.; Knutsson, L.; Risberg, J.; Börjesson, S.; Larsson, E.-M.; Gustafson, L.; Passant, U.; Ståhlberg, F. Attempts to improve absolute quantification of cerebral blood flow in dynamic susceptibility contrast magnetic resonance imaging: a simplified T1-weighted steady-state cerebral blood volume approach. *Acta radiologica (Stockholm, Sweden : 1987)* **2007**, *48*, 550–6.

40. Garcia, J.; Khang-Loon, H.; Pantoni, L. Pathology. In *Stroke Pathophysiology, Diagnosis and Management*; Barnett, H. J.; Mohr, J.; Stein, B.; Yatsu, F., Eds.; Churchill Livingston, 1998.

41. Detre, J. a; Wang, J.; Wang, Z.; Rao, H. Arterial spin-labeled perfusion MRI in basic and clinical neuroscience. *Current opinion in neurology* **2009**, *22*, 348–55.

42. Neumann-Haefelin, T.; Wittsack, H.-J.; Wenserski, F.; Siebler, M.; Seitz, R. J.; Modder, U.; Freund, H.-J. Diffusion- and Perfusion-Weighted MRI : The DWI/PWI Mismatch Region in Acute Stroke. *Stroke* **1999**, *30*, 1591–1597.

43. Straka, M.; Albers, G. W.; Bammer, R. Real-time diffusion-perfusion mismatch analysis in acute stroke. *Journal of magnetic resonance imaging : JMRI* **2010**, *32*, 1024–37.

44. Parsons, M. W.; Barber, P. A.; Chalk, J.; Darby, D. G.; Rose, S.; Desmond, P. M.; Gerraty, R. P.; Tress, B. M.; Wright, P. M.; Donnan, G. A.; Davis, S. M. Diffusion- and perfusion-weighted MRI response to thrombolysis in stroke. *Annals of neurology* **2002**, *51*, 28–37.

45. Neumann-Haefelin, T.; Wittsack, H.-J.; Wenserski, F.; Siebler, M.; Seitz, R. J.; Modder, U.; Freund, H.-J. Diffusion- and Perfusion-Weighted MRI : The DWI/PWI Mismatch Region in Acute Stroke. *Stroke* **1999**, *30*, 1591–1597.

46. Fiehler, J. Cerebral Blood Flow Predicts Lesion Growth in Acute Stroke Patients. *Stroke* **2002**, *33*, 2421–2425.

47. Hjort, N.; Butcher, K.; Davis, S. M.; Kidwell, C. S.; Koroshetz, W. J.; Röther, J.; Schellinger, P. D.; Warach, S.; Østergaard, L. Magnetic resonance imaging criteria for thrombolysis in acute cerebral infarct. *Stroke; a journal of cerebral circulation* **2005**, *36*, 388–97.

48. Schellinger, P. D.; Jansen, O.; Fiebach, J. B.; Heiland, S.; Steiner, T.; Schwab, S.; Pohlers, O.; Ryssel, H.; Sartor, K.; Hacke, W. Monitoring Intravenous Recombinant Tissue Plasminogen Activator Thrombolysis for Acute Ischemic Stroke With Diffusion and Perfusion MRI. *Stroke* **2000**, *31*, 1318–1328.

49. Coutts, S. B.; Simon, J. E.; Tomanek, A. I.; Barber, P. A.; Chan, J.; Hudon, M. E.; Mitchell, J. R.; Frayne, R.; Eliasziw, M.; Buchan, A. M.; Demchuk, A. M. Reliability of assessing percentage of diffusion-perfusion mismatch. *Stroke; a journal of cerebral circulation* **2003**, *34*, 1681–3.

50. Rother, J. Effect of Intravenous Thrombolysis on MRI Parameters and Functional Outcome in Acute Stroke <6 Hours. *Stroke* **2002**, *33*, 2438–2445.

51. Butcher, K. S.; Parsons, M.; MacGregor, L.; Barber, P. A.; Chalk, J.; Bladin, C.; Levi, C.; Kimber, T.; Schultz, D.; Fink, J.; Tress, B.; Donnan, G.; Davis, S. Refining the Perfusion-Diffusion Mismatch Hypothesis. *Stroke* **2005**, *36*, 1153–1159.

52. Kane, I.; Hand, P. J.; Rivers, C.; Armitage, P.; Bastin, M. E.; Lindley, R.; Dennis, M.; Wardlaw, J. M. A practical assessment of magnetic resonance diffusion-perfusion mismatch in acute stroke: observer variation and outcome. *Journal of neurology* **2009**, *256*, 1832–8.

53. Pooley, R. A. AAPM/RSNA physics tutorial for residents: fundamental physics of MR imaging. *Radiographics* **2005**, *25*, 1087–99.

54. Bitar, R.; Leung, G.; Perng, R.; Tadros, S.; Moody, A. R.; Sarrazin, J.; McGregor, C.; Christakis, M.; Symons, S.; Nelson, A.; Roberts, T. P. MR pulse sequences: what every radiologist wants to know but is afraid to ask. *Radiographics* **2006**, *26*, 513–37.

55. Villringer, A.; Rosen, B. R.; Belliveau, J. W.; Ackerman, J. L.; Lauffer, R. B.; Buxton, R. B.; Chao, Y. S.; Wedeen, V. J.; Brady, T. J. Dynamic imaging with lanthanide chelates in normal brain: contrast due to magnetic susceptibility effects. *Magnetic Resonance in Medicine* **1988**, *6*, 164–74.

56. Rosen, B. R.; Belliveau, J. W.; Vevea, J. M.; Brady, T. J. Perfusion imaging with NMR contrast agents. *Magnetic Resonance in Medicine* **1990**, *14*, 249–65.

57. Quarles, C. C.; Gochberg, D. F.; Gore, J. C.; Yankeelov, T. E. A theoretical framework to model DSC-MRI data acquired in the presence of contrast agent extravasation. *Physics in Medicine and Biology* **2009**, *54*, 5749–66.

58. Quarles, C. C.; Ward, B. D.; Schmainda, K. M. Improving the reliability of obtaining tumor hemodynamic parameters in the presence of contrast agent extravasation. *Magnetic Resonance in Medicine* **2005**, *53*, 1307–16.

59. Donahue, K. M.; Weisskoff, R. M.; Burstein, D. Water diffusion and exchange as they influence contrast enhancement. *Journal of magnetic resonance imaging : JMRI* **2000**, *7*, 102–10.

60. Emblem, K. E.; Bjornerud, A.; Mouridsen, K.; Borra, R. J. H.; Batchelor, T. T.; Jain, R. K.; Sorensen, a G. T(1)- and T(2)(*)-dominant extravasation correction in DSC-MRI: Part II-predicting patient outcome after a single dose of cediranib in recurrent glioblastoma patients. *Journal of Cerebral Blood Fow and Metabolism* **2011**, *31*, 2054–64.

61. Bjornerud, A.; Sorensen, a G.; Mouridsen, K.; Emblem, K. E. T(1)- and T(2)(*)-dominant extravasation correction in DSC-MRI: Part I-theoretical considerations and implications for

assessment of tumor hemodynamic properties. *Journal of Cerebral Blood Fow and Metabolism* **2011**, 1–13.

62. Zierler, K. L. Theoretical basis of indicator-dilution methods for measuring flow and volume. *Circulation Research* **1962**, *10*, 393–407.

63. Calamante, F.; Thomas, D. L.; Pell, G. S.; Wiersma, J.; Turner, R. Measuring cerebral blood flow using magnetic resonance imaging techniques. *Journal of Cerebral Blood Fow and Metabolism* **1999**, *19*, 701–35.

64. Zierler, K. L. Equations for measuring blood flow by external monitoring of radioisotopes. *Circulation Research* **1965**, *16*, 309–21.

65. Axel, L. Cerebral blood flow determination by rapid-sequence computed tomography: theoretical analysis. *Radiology* **1980**, *137*, 679–86.

66. Meier, P.; Zierler, K. L. On the theory of the indicator-dilution method for measurement of blood flow and volume. *Journal of applied physiology* **1954**, *6*, 731–44.

67. Knutsson, L.; Börjesson, S.; Larsson, E.-M.; Risberg, J.; Gustafson, L.; Passant, U.; Ståhlberg, F.; Wirestam, R. Absolute quantification of cerebral blood flow in normal volunteers: correlation between Xe-133 SPECT and dynamic susceptibility contrast MRI. *Journal of magnetic resonance imaging* **2007**, *26*, 913–20.

68. Knutsson, L.; van Westen, D.; Petersen, E. T.; Bloch, K. M.; Holtås, S.; Ståhlberg, F.; Wirestam, R. Absolute quantification of cerebral blood flow: correlation between dynamic susceptibility contrast MRI and model-free arterial spin labeling. *Magnetic resonance imaging* **2010**, *28*, 1–7.

69. Calamante, F.; Gadian, D. G.; Connelly, A. Quantification of perfusion using bolus tracking magnetic resonance imaging in stroke: assumptions, limitations, and potential implications for clinical use. *Stroke* **2002**, *33*, 1146–51.

70. Calamante, F. Artifacts and pitfalls in perfusion MR imaging. In *Clinical MR Neuroimaging: diffusion, perfusion and spectroscopy*; Gillard, J.; Waldman, A.; Barker, P., Eds.; Cambridge University Press, 2005; pp. 141–160.

71. Schmidt, R.; Graafen, D.; Weber, S.; Schreiber, L. M. Computational fluid dynamics simulations of contrast agent bolus dispersion in a coronary bifurcation: impact on MRI-based quantification of myocardial perfusion. *Computational and mathematical methods in medicine* **2013**, *2013*, 513187.

72. Calamante, F.; Yim, P. J.; Cebral, J. R. Estimation of bolus dispersion effects in perfusion MRI using image-based computational fluid dynamics. *NeuroImage* **2003**, *19*, 341–53.

73. Graafen, D.; Münnemann, K.; Weber, S.; Kreitner, K.-F.; Schreiber, L. M. Quantitative contrast-enhanced myocardial perfusion magnetic resonance imaging: simulation of bolus dispersion in constricted vessels. *Medical physics* **2009**, *36*, 3099–106.

74. Graafen, D.; Hamer, J.; Weber, S.; Schreiber, L. M. Quantitative myocardial perfusion magnetic resonance imaging: the impact of pulsatile flow on contrast agent bolus dispersion. *Physics in medicine and biology* **2011**, *56*, 5167–85.

75. Schmitt, M.; Viallon, M.; Thelen, M.; Schreiber, W. G. Quantification of myocardial blood flow and blood flow reserve in the presence of arterial dispersion: a simulation study. *Magnetic resonance in medicine: official journal of the Society of Magnetic Resonance in Medicine / Society of Magnetic Resonance in Medicine* **2002**, *47*, 787–93.

76. Calamante, F. Arterial input function in perfusion MRI: a comprehensive review. *Progress in Nuclear Magnetic Resonance Spectroscopy* **2013**.

77. Calamante, F.; Mørup, M.; Hansen, L. K. Defining a local arterial input function for perfusion MRI using independent component analysis. *Magnetic Resonance in Medicine* **2004**, *52*, 789–97.

78. Foottit, C.; Cron, G. O.; Hogan, M. J.; Nguyen, T. B.; Cameron, I. Determination of the venous output function from MR signal phase: feasibility for quantitative DCE-MRI in human brain. *Magnetic Resonance in Medicine* **2010**, *63*, 772–81.

79. Van Osch, M. J. P.; van der Grond, J.; Bakker, C. J. G. Partial volume effects on arterial input functions: shape and amplitude distortions and their correction. *Journal of magnetic resonance imaging: JMRI* **2005**, *22*, 704–9.

80. Van Osch, M. J.; Vonken, E. J.; Bakker, C. J.; Viergever, M. A. Correcting partial volume artifacts of the arterial input function in quantitative cerebral perfusion MRI. *Magnetic resonance in medicine* **2001**, *45*, 477–85.

81. Sorensen, A.; Kulke, S.; Weisskoff, R.; Boxerman, J.; Buchbinder, B.; Rosen, B. Investigation of cerebral hemodynamics with sprodiamide (Dy-DTPA-BMA) and functional magnetic resonance imaging. In *ASNR*; 1994; p. 237.

82. Jerosch-Herold, M. Quantification of myocardial perfusion by cardiovascular magnetic resonance. *Journal of cardiovascular magnetic resonance: official journal of the Society for Cardiovascular Magnetic Resonance* **2010**, *12*, 57.

83. Chappell, M. A.; Woolrich, M. W.; Kazan, S.; Jezzard, P.; Payne, S. J.; Macintosh, B. J. Modeling dispersion in arterial spin labeling: Validation using dynamic angiographic measurements. *Magnetic resonance in medicine: official journal of the Society of Magnetic Resonance in Medicine / Society of Magnetic Resonance in Medicine* **2013**, *69*, 563–70.

84. Leenders, K. L.; Perani, D.; Lammertsma, A. A.; Heather, J. D.; Buckingham, P.; Healy, M. J.; Gibbs, J. M.; Wise, R. J.; Hatazawa, J.; Herold, S. Cerebral blood flow, blood volume and oxygen utilization. Normal values and effect of age. *Brain* **1990**, *113*, 27–47.

85. Alsop, D. C.; Schlaug, G. The Equivalence of SVD and Fourier Deconvolution for Dynamic Susceptibility Contrast Analysis. In *ISMRM*; 2001; Vol. 691, p. 1581.

86. Golub, G.; Kahan, W. Calculating the Singular Values and Pseudo-Inverse of a Matrix. *Journal of the Society for Industrial and Applied Mathematics Series B Numerical Analysis* **1965**, *2*, 205–224.

87. Oppenheim, A.; Schafer, R. The discrete Fourier transform. In *Discrete-time signal processing*; Prentice Hall, Englewood Cliffs: New Jersey, 1999; pp. 514–580.

88. Liu, H. L.; Pu, Y.; Liu, Y.; Nickerson, L.; Andrews, T.; Fox, P. T.; Gao, J. H. Cerebral blood flow measurement by dynamic contrast MRI using singular value decomposition with an adaptive threshold. *Magnetic Resonance in Medicine* **1999**, *42*, 167–72.

89. Hansen, P. C. Analysis of Discrete Ill-Posed Problems by Means of the L-Curve. *SIAM Review* **1992**, *34*, 561.

90. Tikhonov, A. N.; Arsenin, V. Y. *Solutions of Ill-Posed Problems*; Halsted. Press: New York, 1977; p. 258.

91. Isaaks, E.; Srivastava, R. *An Introduction to Applied Geostatistics*; Oxford University Press: Oxford, 1989.

92. Williams, C. K. I.; Rasmussen, C. E. Gaussian processes for regression. In *Advances in neural information processing systems*; 1996; pp. 514–529.

93. Goutte, C.; Nielsen, F. A.; Hansen, L. K. Modeling the haemodynamic response in fMRI using smooth FIR filters. *IEEE transactions on medical imaging* **2000**, *19*, 1188–201.

94. Bell, B. M.; Pillonetto, G. Estimating parameters and stochastic functions of one variable using nonlinear measurement models. *Inverse Problems* **2004**, *20*, 627–646.

95. Peruzzo, D.; Zanderigo, F.; Bertoldo, A.; Pillonetto, G.; Cosottini, M.; Cobelli, C. Assessment of clinical data of nonlinear stochastic deconvolution versus block-circulant singular value decomposition for quantitative dynamic susceptibility contrast magnetic resonance imaging. *Magnetic resonance imaging* **2011**, 1–10.

96. Murase, K.; Shinohara, M.; Yamazaki, Y. Accuracy of deconvolution analysis based on singular value decomposition for quantification of cerebral blood flow using dynamic susceptibility contrast-enhanced magnetic resonance imaging. *Physics in medicine and biology* **2001**, *46*, 3147–59.

97. Ona, W.; Østergaard, L.; Benner, T.; Rosen, B.; Weisskoff, R.; Sorensen, A. Perfusion calculations using singular value decomposition are biased by tracer arrival timing. In *ISMRM*; Honolulu, 2002.

98. Østergaard, L.; Johannsen, P.; Høst-Poulsen, P.; Vestergaard-Poulsen, P.; Asboe, H.; Gee, A. D.; Hansen, S. B.; Cold, G. E.; Gjedde, A.; Gyldensted, C. Cerebral blood flow measurements by

magnetic resonance imaging bolus tracking: comparison with [(15)O]H2O positron emission tomography in humans. *Journal of Cerebral Blood Flow and Metabolism* **1998**, *18*, 935–40.

99. Alsop, D.; Wedmid, A.; Schlaug, G. Defining a local input function for perfusion quantification with bolus contrast MRI. In *Proceedings of the 10th Annual Meeting of ISMRM, Honolulu*; Honolulu, 2003; p. Abstract 659.

100. Duhamel, G.; Bazelaire, C.; Alsop, D. Input functions from echoplanar hemodynamic studies using dynamic susceptibility contrast: a numerical model compared to in-vivo results. In *Proceedings of the 11th Annual Meeting of ISMRM, Toronto, Canada*; 2003; p. Abstract 2199.

101. Willats, L.; Christensen, S.; Ma, H. K.; Donnan, G. A.; Connelly, A.; Calamante, F. Validating a local Arterial Input Function method for improved perfusion quantification in stroke. *Journal of cerebral blood flow and metabolism: official journal of the International Society of Cerebral Blood Flow and Metabolism* **2011**, *31*, 2189–98.

102. Duhamel, G.; Schlaug, G.; Alsop, D. C. Measurement of arterial input functions for dynamic susceptibility contrast magnetic resonance imaging using echoplanar images: comparison of physical simulations with in vivo results. *Magnetic resonance in medicine: official journal of the Society of Magnetic Resonance in Medicine / Society of Magnetic Resonance in Medicine* **2006**, *55*, 514–23.

103. Lorenz, C.; Benner, T.; Chen, P. J.; Lopez, C. J.; Ay, H.; Zhu, M. W.; Menezes, N. M.; Aronen, H.; Karonen, J.; Liu, Y.; Nuutinen, J.; Sorensen, A. G. Automated perfusion-weighted MRI using localized arterial input functions. *Journal of magnetic resonance imaging: JMRI* **2006**, *24*, 1133–9.

104. Knutsson, L.; Larsson, E.-M.; Thilmann, O.; Ståhlberg, F.; Wirestam, R. Calculation of cerebral perfusion parameters using regional arterial input functions identified by factor analysis. *Journal of magnetic resonance imaging: JMRI* **2006**, *23*, 444–53.

105. Christensen, S.; Calamante, F.; Hjort, N.; Wu, O.; Blankholm, A. D.; Desmond, P.; Davis, S.; Ostergaard, L. Inferring origin of vascular supply from tracer arrival timing patterns using bolus tracking MRI. *Journal of magnetic resonance imaging: JMRI* **2008**, *27*, 1371–81.

106. Grüner, R.; Bjørnarå, B. T.; Moen, G.; Taxt, T. Magnetic resonance brain perfusion imaging with voxel-specific arterial input functions. *Journal of magnetic resonance imaging: JMRI* **2006**, *23*, 273–84.

107. Ahlgren, A.; Wirestam, R.; Petersen, E. T.; Ståhlberg, F.; Knutsson, L. Perfusion quantification by model-free arterial spin labeling using nonlinear stochastic regularization deconvolution. *Magnetic resonance in medicine: official journal of the Society of Magnetic Resonance in Medicine / Society of Magnetic Resonance in Medicine* **2012**, *000*, 1–11.

108. Park, C. S.; Payne, S. J. A generalized mathematical framework for estimating the residue function for arbitrary vascular networks. *Interface Focus* **2013**, *3*.

109. Hyman, J. M. Accurate Monotonicity Preserving Cubic Interpolation. *SIAM Journal on Scientific and Statistical Computing* **1983**, *4*, 645.

110. Chappell, M. A.; Groves, A. R.; Whitcher, B.; Woolrich, M. W. Variational Bayesian Inference for a Nonlinear Forward Model. *IEEE Transactions on Signal Processing* **2009**, *57*, 223–236.

111. Crane, D. E.; Donahue, M. J.; Chappell, M. A.; Sideso, E.; Handa, A.; Kennedy, J.; Jezzard, P.; Macintosh, B. J. Evaluating quantitative approaches to dynamic susceptibility contrast MRI among carotid endarterectomy patients. *Journal of magnetic resonance imaging: JMRI* **2013**, *37*, 936–43.

112. Calamante, F. Bolus dispersion issues related to the quantification of perfusion MRI data. *Journal of magnetic resonance imaging: JMRI* **2005**, *22*, 718–22.

113. Essig, M. Protocol design for high relaxivity contrast agents in MR imaging of the CNS. *European radiology* **2006**, *16 Suppl 7*, M3–7.

114. Essig, M.; Shiroishi, M. S.; Nguyen, T. B.; Saake, M.; Provenzale, J. M.; Enterline, D.; Anzalone, N.; Dorfler, A.; Rovira, A.; Wintermark, M.; Law, M. Perfusion MRI: The Five Most Frequently Asked Technical Questions. *American Journal of Roentgenology* **2012**, *200*, 24–34.

115. Mouridsen, K.; Christensen, S.; Gyldensted, L.; Ostergaard, L. Automatic selection of arterial input function using cluster analysis. *Magnetic resonance in medicine: official journal of the Society of Magnetic Resonance in Medicine / Society of Magnetic Resonance in Medicine* **2006**, *55*, 524–31.

116. Smith, M. R.; Lu, H.; Trochet, S.; Frayne, R. Removing the effect of SVD algorithmic artifacts present in quantitative MR perfusion studies. *Magnetic resonance in medicine: official journal of the Society of Magnetic Resonance in Medicine / Society of Magnetic Resonance in Medicine* **2004**, *51*, 631–4.

117. Willats, L.; Connelly, A.; Calamante, F. Improved deconvolution of perfusion MRI data in the presence of bolus delay and dispersion. *Magnetic resonance in medicine: official journal of the Society of Magnetic Resonance in Medicine / Society of Magnetic Resonance in Medicine* **2006**, *56*, 146–56.

118. MacIntosh, B. J.; Sideso, E.; Donahue, M. J.; Chappell, M. A.; Günther, M.; Handa, A.; Kennedy, J.; Jezzard, P. Intracranial hemodynamics is altered by carotid artery disease and after endarterectomy: a dynamic magnetic resonance angiography study. *Stroke; a journal of cerebral circulation* **2011**, *42*, 979–84.

119. Mouannes-Srour, J. J.; Shin, W.; Ansari, S. A.; Hurley, M. C.; Vakil, P.; Bendok, B. R.; Lee, J. L.; Derdeyn, C. P.; Carroll, T. J. Correction for arterial-tissue delay and dispersion in absolute quantitative cerebral perfusion DSC MR imaging. *Magnetic resonance in medicine* **2012**, *68*, 495–506.

120. Kikuchi, K.; Murase, K.; Miki, H.; Yasuhara, Y.; Sugawara, Y.; Mochizuki, T.; Ikezoe, J.; Ohue, S. Quantitative evaluation of mean transit times obtained with dynamic susceptibility contrast-enhanced MR imaging and with (133)Xe SPECT in occlusive cerebrovascular disease. *AJR. American journal of roentgenology* **2002**, *179*, 229–35.

121. Dani, K. a; Thomas, R. G. R.; Chappell, F. M.; Shuler, K.; MacLeod, M. J.; Muir, K. W.; Wardlaw, J. M. Computed tomography and magnetic resonance perfusion imaging in ischemic stroke: definitions and thresholds. *Annals of neurology* **2011**, *70*, 384–401.

122. Kamalian, S.; Kamalian, S.; Konstas, A. A.; Maas, M. B.; Payabvash, S.; Pomerantz, S. R.; Schaefer, P. W.; Furie, K. L.; González, R. G.; Lev, M. H. CT perfusion mean transit time maps optimally distinguish benign oligemia from true "at-risk" ischemic penumbra, but thresholds vary by postprocessing technique. *AJNR. American journal of neuroradiology* **2012**, *33*, 545–9.

123. Mui, K.; Yoo, a J.; Verduzco, L.; Copen, W. a; Hirsch, J. a; González, R. G.; Schaefer, P. W. Cerebral blood flow thresholds for tissue infarction in patients with acute ischemic stroke treated with intra-arterial revascularization therapy depend on timing of reperfusion. *AJNR. American journal of neuroradiology* **2011**, *32*, 846–51.

124. Arakawa, S.; Wright, P. M.; Koga, M.; Phan, T. G.; Reutens, D. C.; Lim, I.; Gunawan, M. R.; Ma, H.; Perera, N.; Ly, J.; Zavala, J.; Fitt, G.; Donnan, G. a Ischemic thresholds for gray and white matter: a diffusion and perfusion magnetic resonance study. *Stroke; a journal of cerebral circulation* **2006**, *37*, 1211–6.

125. Hjort, N.; Butcher, K.; Davis, S. M.; Kidwell, C. S.; Koroshetz, W. J.; Röther, J.; Schellinger, P. D.; Warach, S.; Østergaard, L. Magnetic resonance imaging criteria for thrombolysis in acute cerebral infarct. *Stroke; a journal of cerebral circulation* **2005**, *36*, 388–97.

126. Zheng, Y.; Martindale, J.; Johnston, D.; Jones, M.; Berwick, J.; Mayhew, J. A Model of the Hemodynamic Response and Oxygen Delivery to Brain. *NeuroImage* **2002**, *16*, 617–637.

127. Christen, T.; Bolar, D. S.; Zaharchuk, G. Imaging brain oxygenation with MRI using blood oxygenation approaches: methods, validation, and clinical applications. *AJNR. American journal of neuroradiology* **2013**, *34*, 1113–23.

128. Kuschinsky, W.; Paulson, O. B. Capillary circulation in the brain. *Cerebrovascular and brain metabolism reviews* **1992**, *4*, 261–86.

129. Ostergaard, L.; Sorensen, a. G.; Chesler, D. a.; Weisskoff, R. M.; Koroshetz, W. J.; Wu, O.; Gyldensted, C.; Rosen, B. R. Combined Diffusion-Weighted and Perfusion-Weighted Flow Heterogeneity Magnetic Resonance Imaging in Acute Stroke. *Stroke* **2000**, *31*, 1097–1103.

130. Perkiö, J.; Soinne, L.; Østergaard, L.; Helenius, J.; Kangasmäki, A.; Martinkauppi, S.; Salonen, O.; Savolainen, S.; Kaste, M.; Tatlisumak, T.; Aronen, H. J. Abnormal intravoxel cerebral blood flow heterogeneity in human ischemic stroke determined by dynamic susceptibility contrast magnetic resonance imaging. *Stroke; a journal of cerebral circulation* **2005**, *36*, 44–9.

131. Simonsen, C. Z.; Røhl, L.; Vestergaard-poulsen, P.; Østergaard, L. Final Infarct Size after Acute Stroke : Prediction with Flow. *Radiology* **2002**, *225*, 269–275.

132. Wintermark, M.; Albers, G. W.; Alexandrov, A. V; Alger, J. R.; Bammer, R.; Baron, J.-C.; Davis, S.; Demaerschalk, B. M.; Derdeyn, C. P.; Donnan, G. A.; Eastwood, J. D.; Fiebach, J. B.; Fisher, M.; Furie, K. L.; Goldmakher, G. V; Hacke, W.; Kidwell, C. S.; Kloska, S. P.; Köhrmann, M.; Koroshetz, W.; Lee, T.-Y.; Lees, K. R.; Lev, M. H.; Liebeskind, D. S.; Ostergaard, L.; Powers, W. J.; Provenzale, J.; Schellinger, P.; Silbergleit, R.; Sorensen, A. G.; Wardlaw, J.; Wu, O.; Warach, S. Acute stroke imaging research roadmap. *AJNR. American journal of neuroradiology* **2008**, *29*, e23–30.

133. Jenkinson, M.; Bannister, P.; Brady, M.; Smith, S. Improved Optimization for the Robust and Accurate Linear Registration and Motion Correction of Brain Images. *NeuroImage* **2002**, *17*, 825–841.

134. Gavrilescu, T.; Babikian, V. L.; Cantelmo, N. L.; Rosales, R.; Pochay, V.; Winter, M. Cerebral microembolism during carotid endarterectomy. *The American Journal of Surgery* **1995**, *170*, 159–164.

135. Lusby, R. J.; Wylie, E. J. Complications of carotid endarterectomy. *The Surgical clinics of North America* **1983**, *63*, 1293–302.

136. Mackey, W. C.; O'Donnell, T. F.; Callow, A. D. Cardiac risk in patients undergoing carotid endarterectomy: impact on perioperative and long-term mortality. *Journal of vascular surgery* **1990**, *11*, 226–33; discussion 233–4.

137. McCrory, D. C.; Goldstein, L. B.; Samsa, G. P.; Oddone, E. Z.; Landsman, P. B.; Moore, W. S.; Matchar, D. B. Predicting complications of carotid endarterectomy. *Stroke; a journal of cerebral circulation* **1993**, *24*, 1285–91.

138. Yamada, K.; Yoshimura, S.; Kawasaki, M.; Enomoto, Y.; Asano, T.; Hara, A.; Minatoguchi, S.; Iwama, T. Embolic complications after carotid artery stenting or carotid endarterectomy are associated with tissue characteristics of carotid plaques evaluated by magnetic resonance imaging. *Atherosclerosis* **2011**, *215*, 399–404.

139. Duval Neto, G. F.; Niencheski, A. H. [Analysis of brain hemometabolism behavior during carotid endarterectomy with temporary clamping.]. *Revista brasileira de anestesiologia* **2004**, *54*, 162–77.

140. Garcia, J. H.; Liu, K. F.; Yoshida, Y.; Chen, S.; Lian, J. Brain microvessels: factors altering their patency after the occlusion of a middle cerebral artery (Wistar rat). *The American journal of pathology* **1994**, *145*, 728–40.

141. Schwab, S.; Spranger, M.; Aschoff, A.; Steiner, T.; Hacke, W. Brain temperature monitoring and modulation in patients with severe MCA infarction. *Neurology* **1997**, *48*, 762–7.

142. Zivin, J. A.; Choi, D. W. Stroke therapy. *Scientific American* **1991**, *265*, 56–63.

143. Hossmann, K.-A. Pathophysiological basis of translational stroke research. *Folia neuropathologica* **2009**, *47*, 213–27.

144. Heiss, W.-D. The concept of the penumbra: can it be translated to stroke management? *International journal of stroke* **2010**, *5*, 290–5.

145. Research, B. T. Brain Tumor - Statistics http://www.braintumourresearch.org/statistics-.

146. Essig, M.; Wenz, F.; Scholdei, R.; Brüning, R.; Berchtenbreiter, C.; Meurer, M.; Knopp, M. V Dynamic susceptibility contrast-enhanced echo-planar imaging of cerebral gliomas. Effect of contrast medium extravasation. *Acta radiologica (Stockholm, Sweden : 1987)* **2002**, *43*, 354–9.

147. Boxerman, J. L.; Schmainda, K. M.; Weisskoff, R. M. Relative cerebral blood volume maps corrected for contrast agent extravasation significantly correlate with glioma tumor grade, whereas uncorrected maps do not. *AJNR Am J Neuroradiol.* **2006**, *27*, 859–67.

148. Jain, R. K.; di Tomaso, E.; Duda, D. G.; Loeffler, J. S.; Sorensen, A. G.; Batchelor, T. T. Angiogenesis in brain tumours. *Nature reviews. Neuroscience* **2007**, *8*, 610–22.

149. Kim, W.-Y.; Lee, H.-Y. Brain angiogenesis in developmental and pathological processes: mechanism and therapeutic intervention in brain tumors. *The FEBS journal* **2009**, *276*, 4653–64.

150. Heart Foundation, B. Cardiovascular disease http://www.bhf.org.uk/heart-health/conditions/cardiovascular-disease.aspx.

151. Allender, S.; Foster, C.; Scarborough, P.; Rayner, M. The burden of physical activity-related ill health in the UK. *Journal of epidemiology and community health* **2007**, *61*, 344–8.

152. Zarinabad, N.; Chiribiri, A.; Hautvast, G. L. T. F.; Ishida, M.; Schuster, A.; Cvetkovic, Z.; Batchelor, P. G.; Nagel, E. Voxel-wise quantification of myocardial perfusion by cardiac magnetic resonance. Feasibility and methods comparison. *Magnetic resonance in medicine* **2012**, *68*, 1994–2004.

153. Detre, J. A.; Leigh, J. S.; Williams, D. S.; Koretsky, A. P. Perfusion imaging. *Magnetic resonance in medicine: official journal of the Society of Magnetic Resonance in Medicine / Society of Magnetic Resonance in Medicine* **1992**, *23*, 37–45.

154. Chalela, J. A.; Alsop, D. C.; Gonzalez-Atavales, J. B.; Maldjian, J. A.; Kasner, S. E.; Detre, J. A. Magnetic resonance perfusion imaging in acute ischemic stroke using continuous arterial spin labeling. *Stroke; a journal of cerebral circulation* **2000**, *31*, 680–7.

155. Detre, J. A.; Alsop, D. C.; Vives, L. R.; Maccotta, L.; Teener, J. W.; Raps, E. C. Noninvasive MRI evaluation of cerebral blood flow in cerebrovascular disease. *Neurology* **1998**, *50*, 633–41.

156. Buxton, R. B.; Frank, L. R.; Wong, E. C.; Siewert, B.; Warach, S.; Edelman, R. R. A general kinetic model for quantitative perfusion imaging with arterial spin labeling. *Magnetic resonance in medicine* **1998**, *40*, 383–96.

157. Petersen, E. T.; Lim, T.; Golay, X. Model-free arterial spin labeling quantification approach for perfusion MRI. *Magnetic resonance in medicine: official journal of the Society of Magnetic Resonance in Medicine / Society of Magnetic Resonance in Medicine* **2006**, *55*, 219–32.

158. Petersen, E. T.; Mouridsen, K.; Golay, X. The QUASAR reproducibility study, Part II: Results from a multi-center Arterial Spin Labeling test-retest study. *NeuroImage* **2010**, *49*, 104–13.

Appendix I: Hemodynamic Model by Payne[3]

1 Governing equation

Mass transport equation for oxygen in 1D axisymmetric vessel:

$$\frac{\partial C_B}{\partial t} + U\frac{\partial C_B}{\partial x} = -D\frac{2\pi R}{\pi R^2}(C_P - C_T) \tag{1}$$

where we are assuming uniform velocity, i.e. no dispersion, and linear diffusion across the vessel wall with diffusion speed *D*. Subscripts *B*, *P* and *T* refer to oxygen concentrations in blood, plasma and tissue respectively.

Assume steady state conditions and that plasma concentration is a fraction *k* of blood concentration. Non-dimensionalise (1) in space with respect to vessel length, *L*, such that $z = x/L$:

$$\frac{\partial C_B}{\partial z} + k\lambda T C_B = \lambda T C_T \tag{2}$$

where:

$$\lambda = \frac{2D}{R} \tag{3}$$

$$T = \frac{L}{U} \tag{4}$$

N.B. These are not non-dimensional since we retain transit time explicitly.

2 Analysis

Equation (2) can be solved over *z*:

$$C_B = Ae^{-k\lambda T z} + \frac{C_T}{k} \tag{5}$$

with inlet boundary condition, $C_{B,in}$, giving the solution:

[3] This is the direct copy of the technical note by Stephen J. Payne.

$$C_B = \left(C_{B,in} - \frac{C_T}{k}\right) e^{-k\lambda Tz} + \frac{C_T}{k} \tag{6}$$

The Oxygen Extraction Fraction (OEF) is then equal to:

$$OEF = \frac{C_{B,in} - C_{B,out}}{C_{B,in}} = \left(1 - \frac{C_T}{kC_{B,in}}\right)\left(1 - e^{-k\lambda T}\right) \tag{7}$$

Now assume a distribution of transit times and integrate to calculate the overall OEF:

$$OEF = \int_0^\infty \left(1 - \frac{C_T}{kC_{B,in}}\right)\left(1 - e^{-k\lambda T}\right)h(T)dT \tag{8}$$

where, to start with, we assume a Gamma distribution for *h(T)*:

$$h(T) = \frac{1}{\Gamma(\alpha)\beta^\alpha} T^{\alpha-1} e^{-\frac{T}{\beta}} \tag{9}$$

Substitution of (9) into (8) gives:

$$OEF = \left(1 - \frac{C_T}{kC_{B,in}}\right)\left[1 - \left(\frac{1}{1 + k\lambda\beta}\right)^\alpha\right] \tag{10}$$

Hence metabolic rate is also given by:

$$CMRO2 = F\left(C_{B,in} - \frac{C_T}{k}\right)\left[1 - \left(\frac{1}{1 + k\lambda\beta}\right)^\alpha\right] \tag{11}$$

where *F* is the cerebral blood flow. MTT and CTTH can also be written in terms of the Gamma distribution parameters.

$$MTT = \mu = \alpha\beta \tag{12}$$

$$CTTH = \sigma = \sqrt{\alpha}\beta \tag{13}$$

If we divide (11) by its baseline values, we obtain:

$$m = f\frac{\left[1-\left(\frac{1}{1+k\lambda\beta}\right)^{\alpha}\right]}{\left[1-\left(\frac{1}{1+k\lambda\bar{\beta}}\right)^{\bar{\alpha}}\right]} \tag{14}$$

where *m* is fractional CMRO2 and *f* is fractional flow.

If it is assumed that cerebral blood volume remains constant, then fractional flow is inversely proportional to fractional MTT. If baseline OEF is known, typically around 0.3 for the capillary bed, then the denominator in (14) can be re-written, giving:

$$m = \frac{\bar{\mu}}{\mu}\frac{\left[1-\left(\frac{1}{1+k\lambda\beta}\right)^{\alpha}\right]}{\left[\frac{\overline{OEF}}{\left(1-\frac{\bar{C}_T}{k\bar{C}_{B,in}}\right)}\right]} \tag{15}$$

Re-arranging:

$$\left[\frac{\overline{OEF}}{\bar{\mu}\left(1-\frac{\bar{C}_T}{k\bar{C}_{B,in}}\right)}\right] = \frac{1}{m\mu}\left[1-\left(1+k\lambda\frac{\sigma^2}{\mu}\right)^{-\frac{\mu^2}{\sigma^2}}\right] \tag{16}$$

The LHS is fixed by baseline conditions and the RHS thus solves to give CTTH as a function of MTT for any given value of fractional CMRO2, *m*, and diffusion rate of oxygen, $\lambda = 2D/R$. We assume that *k* remains constant, since this is a fractional concentration and thus unlikely, at first order, to change significantly.

Equation (16) has to be solved numerically, but this is straightforward. Using values quoted in Zheng et al. [126] and Ostergaard et al. [10] we take baseline OEF to be 0.3, $k = 0.01$, $C_T/C_{P,in} = 0.1$ and $\lambda = 100$/s (close to the quoted value of 118/s). The LHS of (16) is thus equal to 1/3 divided by baseline MTT and the term $k\lambda = 1$. Note that (16) is largely invariant to changes in tissue

concentration around the baseline, very similar to Figure 5 in Ostergaard et al. [10], which makes plotting the results simpler, although we explicitly allow two model parameters to vary, unlike the previous paper.

CTTH as a function of MTT (assuming a baseline MTT of 2 seconds) for various fractions of baseline CMRO2 is shown below. Clearly, changes in CMRO2 will have a very substantial impact on the behaviour: note also that the form of the relationship is in good agreement with the results from Ostergaard et al. [10], which is reassuring. A similar plot can be generated for changes in kλ, but the resulting plots exhibit a much smaller variation.

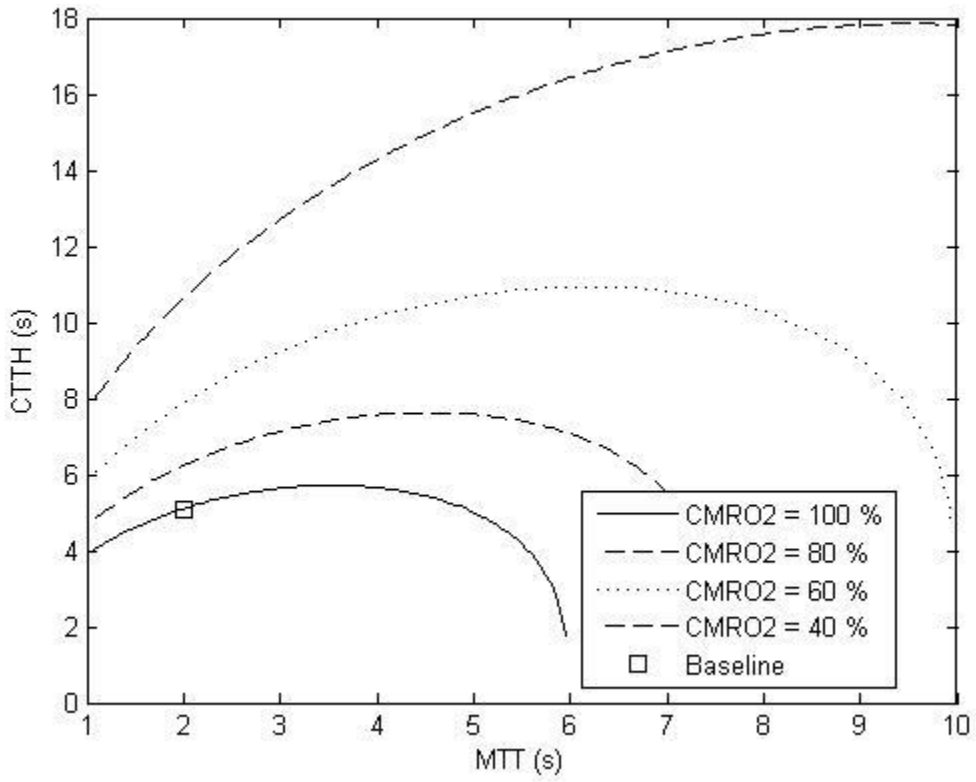

It is worth noting that we have assumed a Gamma form of the transit time distribution: it would be possible to choose any suitable form for *h(T)*, in which case (16) becomes, in general form:

$$\left[\frac{\overline{OEF}}{\bar{\mu}\left(1-\frac{\bar{C}_T}{k\bar{C}_{B,in}}\right)}\right]=\frac{1}{m\mu}\left[1-\int_0^{\infty}e^{-k\lambda T}h(T)dT\right] \quad (17)$$

If desired, this could be solved numerically for any experimentally-derived *h(T)* and curves similar to that in the Figure above derived accordingly. Unless *h(T)* is very different from a Gamma distribution, this will not affect the results very substantially though.